KEK Proceedings 2009-5
September 2009
H

Proceedings of the ILC Physics Working Group Meetings at KEK in the period from May 2007 to June 2009

Edited by

Katsumasa Ikematsu, Yasuhiro Okada, Hiroaki Ono, Shinya Kanemura,
Taikan Suehara, Yosuke Takubo, Tomohiko Tanabe, and Keisuke Fujii

The 8th General Meeting of the ILC Physics Working Group, January 21, 2009

Preface

The ILC physics working group is a mixture of experimentalists and theorists mainly working in Japan. It has its origin in the previous LC physics study group and has been reformed with the initiative of a JSPS Creative Scientific Research project: "Research and Development of a Novel Detector System for the International Linear Collider". The working group is, however, formally independent of the JSPS project and is open to everybody who is interested in ILC physics. The primary task of the working group is to reexamine the ILC physics in the context of the expected LHC outcome and to further strengthen the physics case for the ILC project. The topics covered in the working group activities range from key measurements such as those of the Higgs self-coupling and the top Yukawa coupling to uncover the secrets of the electroweak symmetry breaking to various new physics scenarios like supersymmetry, large extra dimensions, and other models of terascale physics.

The working group has held ten General Meetings in the period of May 2007 to June 2009 to discuss the topics mentioned above. This report summarizes the progress made in this period and sets a milestone for future developments in ILC physics.

Editors, Conveners of the Working Group

Contents

Study of the Higgs Direct Reconstruction in $ZH \to q\bar{q}H$ for ILC

Hiroaki Ono[(a)*]

[(a)] *Nippon Dental University School of Life Dentistry at Niigata, Niigata, Japan*

Precise measurement of the Higgs boson properties is an important issue of the International Linear Collider (ILC) experiment. We studied the accuracy of the Higgs mass reconstruction in the $ZH \to q\bar{q}H$ multi-jet process with the Higgs mass of $M_H = 120$ GeV at $\sqrt{s} = 250$ GeV with the ILD detector model. In this study, we obtained the reconstructed Higgs mass of $M_H = 120.79 \pm 0.089$ GeV and 5.3% measurement accuracy of the cross-section for $ZH \to q\bar{q}b\bar{b}$ with the integrated luminosity of $\mathcal{L} = 250$ fb^{-1} data samples.

1 Introduction

International Linear Collider (ILC) [1] is a future e^+e^- collider experiment for the precise measurement and the validation of the Standard Model (SM) physics, especially for the measurement of the Higgs boson property, even the discovery of the Higgs boson will be realized in Large Hadron Collider (LHC) experiment. In the SM, light Higgs boson mass (M_H) is predicted around the 114.4 GeV $\leq M_H \leq$ 160 GeV from the study in LEP [2] and Tevatron [3] experiment. The largest production cross-section for SM Higgs boson is obtained through the Higgs-strahlung ($e^+e^- \to Z^* \to ZH$) process which associated with the Z boson and the Z mainly decays to $q\bar{q}$ pair, as shown in Fig. 1, around the ZH production threshold energy shown in Fig. 2 (a).

Since Higgs boson mainly decays to $b\bar{b}$ pair at the Higgs mass below 140 GeV region as shown in Fig. 2 (b), the final state of the $ZH \to q\bar{q}H$ process forms the four-jet. In ILC experiment, the most of interesting physics processes including ZH process form the multi-jets final state from the decay of gage bosons (W, Z) and heavy flavor quarks (b, c), thus ILC detectors are required to have the good jet energy resolution for the precise measurement. There are three detector concepts, SiD, ILD and 4^{th} for the ILC detector, and ILD is the merged concepts of the previous GLD [4] (Asian group) and LDC [5] (European group) models for the Letter of Intent (LOI) submission [6]. In order to achieve the best jet energy resolution, ILD adopt the Particle Flow Algorithm (PFA) suited detector design. Since the PFA performance is degraded by the cluster overlapping and the double-counting of the particles

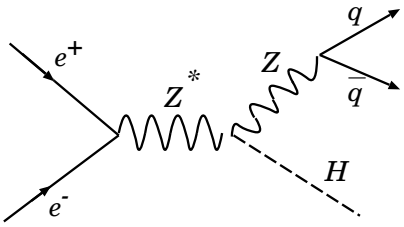

Figure 1: Higgs boson production via Higgs-strahlung (ZH) process and Z mainly decay to $q\bar{q}$.

*TEL:+81-25-267-1500-(537), MAIL:ono@ngt.ndu.ac.jp

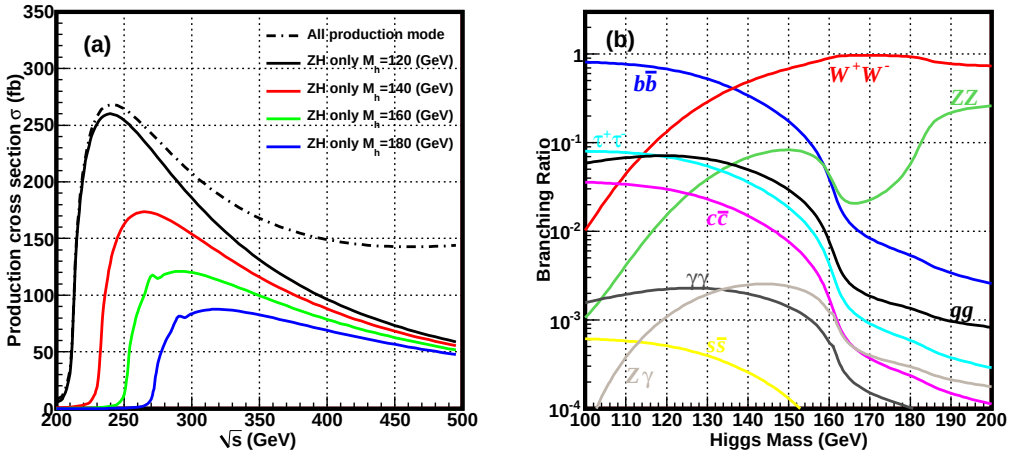

Figure 2: (a). Production cross-section of the Higgs boson as a function of center-of-mass energy ($\sqrt{s}$) and (b). branching ratio of the Higgs decay as a function of the Higgs mass.

energy in the calorimeter, particles separation in the calorimeter is an important key for better PFA performance.

The figure-of-merit of the PFA performance from each detector parameter relating to the particles separation in the calorimeter is described as $F.O.M. = BR^2/\sqrt{\sigma^2 + {R_M}^2}$, where B is a magnetic field, R is a detector radius, σ is a segmentation of the calorimeter and R_M is a effective Moliere radius of the calorimeter. In order to maximize the $F.O.M.$, ILD detector adopts the large radius tracker and high granularity calorimeter with 3.5 T magnetic field. In this analysis, we study the direct reconstruction of the Higgs boson mass with the full detector simulation for $ZH \to q\bar{q}H$, $H \to b\bar{b}$ four-jet mode with the ILD detector model.

2 Simulation tools

For full detector simulation study, we use the ILD detector model based Monte Carlo (MC) full simulation package called Mokka, which is based on the MC simulation package Geant4 [7]. Generated MC hits are reconstructed and smeared in the reconstruction package called MarineReco which includes the PFA package called PandoraPFA [8]. Since $\sqrt{s} = 250$ GeV reconstructed and skimmed signal and background samples called DST files are generated for the LOI physics analysis in ILD group, we use these DST data samples saved in the linear collider common data format called LCIO. For the DST data sample analysis, we use the useful analysis package library called Anlib for the event shape analysis and jets reconstruction, and analysis process is handled through the Root [9] based analysis framework called JSF [10]. For the comparison of the PFA performance between realistic PFA and perfect-clustering PFA, we also use the GLD detector model MC full simulator called Jupiter [11] with the generating the signal and background events by PYTHIA, and reconstruction package called Satellites [12] based on Root, both of them are also controlled

in the JSF framework. From the comparison of the $ZH \to q\bar{q}H$ in GLD detector model, shown in Fig 2, PandoraPFA reconstruction performance (a) achieve the comparable performance with perfect-clustering PFA (b) in terms of the reconstructed Higgs mass distribution width of σ which corresponds to the jet energy resolution even only the $ZZ \to q\bar{q}q'\bar{q}'$ background is considered. Therefore, we shift to the full SM background analysis with common DST data.

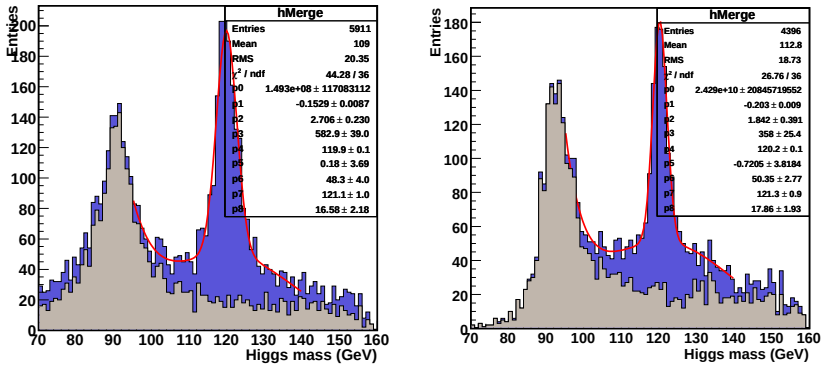

(a) (b)

Figure 3: Comparison of the reconstructed Higgs mass distribution for $ZH \to q\bar{q}b\bar{b}$ only with ZZ background in GLD detector model with the different PFA clustering of (a) realistic PandoraPFA and (b) perfect clustering PFA.

3 Analysis Procedure of $ZH \to q\bar{q}H$ mode

3.a MC samples

The SM Higgs boson is mainly produced through the Higgs-strahlung $e^+e^- \to ZH$ process around the production threshold center-of-mass energy ($\sqrt{s} \sim 230$ GeV). Since the main decay mode at $M_H < 2M_W$, Higgs boson mainly decays to $b\bar{b}$ pair, thus largest production cross-section is obtained from the $ZH \to q\bar{q}b\bar{b}$ process, which forms four-jet final state and both Z and H can be reconstructed directly. Fig. 4 shows the typical event display of the $ZH \to q\bar{q}H$ in JSF. In this analysis, we assume the center-of-mass energy as the ZH production threshold of $\sqrt{s} = 250$ GeV and the light Higgs mass of $M_H = 120$ GeV. Each DST data samples is scaled to the integrated luminosity of $\mathcal{L} = 250$ fb^{-1} and the beam polarization to $P(e^+, e^-) = (30\%, -80\%)$. The main backgrounds for $ZH \to q\bar{q}b\bar{b}$ are considered as following

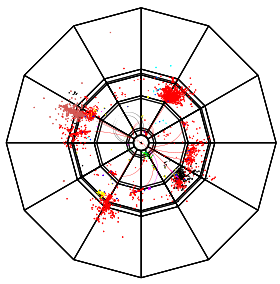

Figure 4: Typical event display of the $ZH \to q\bar{q}H$ four-jet final state.

processes: $ZH \to Z^*/\gamma \to q\bar{q}$, $e^+e^- \to WW/ZZ \to$
$qq'q''q'''$ or $q\bar{q}q'\bar{q'}$, $e^+e^- \to WW \to \nu\ell qq'$ and $e^+e^- \to ZZ \to \ell\ell\ell\ell$. Generated signal and background MC samples which scaled to be $\mathcal{L} = 250$ fb^{-1} are summarized in Table. 1.

MC samples ($\mathcal{L} = 250$ fb^{-1})	$ZH \to qqH$ (sig)	$qqqq$	$\nu\ell qq$	$\ell\ell\ell\ell$	qq
Number of generated events	51763	814163	302807	98127	2529928

Table 1: Generated signal and background MC data samples scaled with $\mathcal{L} = 250$ fb^{-1}.

In order to correct the escape energy from the heavy quark decay including neutrinos, kinematic five constraint (5C) fit is applied, which consists of the four constraints (4C) of momentum balance ($\sum P_{x,y,z_i} = 0$) and jets energy balance ($\sum E_i - \sqrt{s} = 0$) of the four-jet and one Z mass constraints for Z candidate di-jet. For the kinematic fitting, jet energies (E_j) and jet angles (θ, ϕ) of each jet are used as measured variables. Finally, reconstructed Higgs mass distribution is fitted with the Gaussian convoluted with Gaussian function for the signal and exponential function for the contribution from background events which remain after the Higgs boson selections.

3.b Jet Reconstruction

Since the final state of the $ZH \to q\bar{q}H$ mode forms four-jet, after the PandoraPFA clustering, forced four-jet clustering based on Durham jet-clustering algorithm has applied. In order to select the best jet pair combination from the four-jet, following χ^2 value is evaluated,

$$\chi^2 = \left(\frac{M_{12} - M_Z}{\sigma_{M_Z}}\right)^2 + \left(\frac{MissM_{34} - M_Z}{\sigma_{MM_H}}\right)^2 \tag{3.1}$$

where M_{12} is Z candidate di-jet mass, $MissM_{34}$ is a missing mass of the remaining Higgs candidate di-jet, M_Z is the Z boson mass (91.2 GeV), and σ_{M_Z} and $\sigma_{MissM_{34}}$ are sigma of distribution of the reconstructed Z boson mass and the missing mass of the Higgs candidate jets, respectively. In order to select the best jets pair combination, $\chi^2 < 10$ is required for the reconstructed jets pair.

3.c Event selection

After the χ^2 cut to select the best jet pair combination, following event selections are applied for background rejection:

(a) visible energy : $200 \leq E_{vis} \leq 270$ GeV;

(b) Longitudinal momentum of the Z : $|P_{\ell Z}| < 70$ GeV to reduce ZZ background;

(c) Higgs production angle : $|\cos\theta_H| < 0.85$ to reduce the ZZ background;

(d) thrust angle : $thrust < 0.9$;

(e) Number of particles: $N_{particle} > 40$ to suppress the $\ell\ell\ell\ell$ background;

(f) Maximum and minimum jet energy fraction: $E_{min}/E_{max} > 0.25$;

(g) Maximum momentum of jet: $P_{j_{max}} < 100$ GeV;

(h) Y Plus : $YPlus > 0.0001$;

(i) Y Minus : $YMinus > 0.001$;

(j) Minimum angle of Z-H jets : $20 < \theta_{ZHj_{min}} < 135$;

(k) Maximum angle of Z-H jets : $110 < \theta_{ZHj_{max}}$;

(l) b-tagging : $P_{btag} > 0.5$ from LCFIVTX package.

The distribution and its cut positions for each selection variable are shown in Fig. 1. Since the W/Z generated in the WW/ZZ background event are relatively boosted compare to the Z generated in ZH signal event, longitudinal momentum of Z ($P_{\ell Z}$) and maximum momentum in jets ($P_{j_{max}}$) are higher in WW/ZZ background event than in signal event. None jet-like background events are reduced by the number of particles (N_{PFO}) cut. Y Plus and Y Minus values are threshold Y-values used in the jet clustering topology which reconstructed from four-jet to five-jet or three-jet, respectively. Minimum and maximum angles between Z and H candidate jets are also used for the separation by the event shape difference between ZH event and backgrounds.

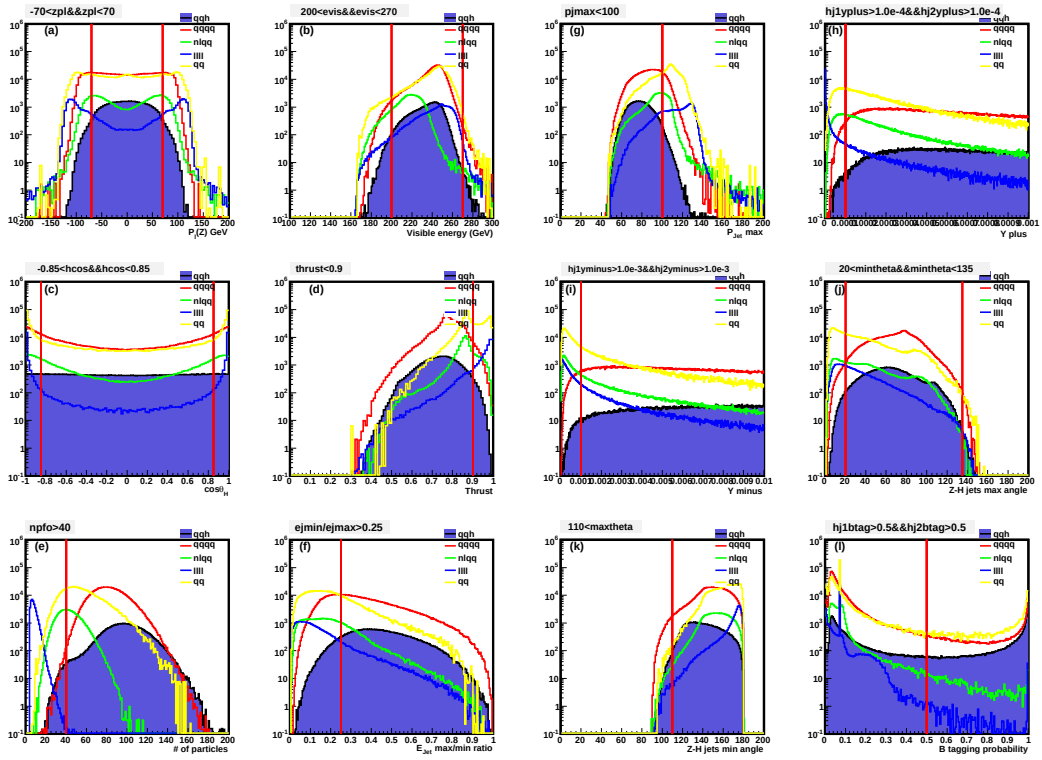

Figure 5: Distribution of each selection variable and its cut positions to select $ZH \to q\bar{q}b\bar{b}$ event.

Finally, we apply the vertex tagging selection for the neural net output of the b-likeness analyzed in the vertexing package called LCFIVTX in ilcsoft. The reduction summary in each event selection is listed in the Table 2.

Selections	$ZH \to q\bar{q}H$(Sig)	$qqqq$	$\nu\ell qq$	$\ell\ell\ell\ell$	qq
no cuts	51745	814162	302807	98127	2529928
χ^2	36748 (71.02 %)	688703 (84.59 %)	19043 (6.29 %)	25375 (25.86 %)	541852 (21.42 %)
$\lvert P_{lZ}\rvert$	34952 (67.55 %)	479403 (58.88 %)	12832 (4.24 %)	5565 (5.67 %)	293883 (11.62 %)
E_{vis}	34924 (67.49 %)	477994 (58.71 %)	12457 (4.11 %)	5335 (5.44 %)	287324 (11.36 %)
$\lvert\cos\theta_H\rvert$	30451 (58.85 %)	397270 (48.79 %)	9934 (3.28 %)	2167 (2.21 %)	223873 (8.85 %)
$thrust$	29916 (57.81 %)	389703 (47.87 %)	8312 (2.75 %)	1422 (1.45 %)	103283 (4.08 %)
$N_{particles}$	29820 (57.63 %)	389514 (47.84 %)	4353 (1.44 %)	0 (0.00 %)	87022 (3.44 %)
$E_{j\,min}/E_{j\,max}$	27843 (53.81 %)	297580 (36.55 %)	1603 (0.53 %)	0 (0.00 %)	40880 (1.62 %)
$p_{j\,max}$	27622 (53.38 %)	289490 (35.56 %)	1500 (0.50 %)	0 (0.00 %)	31382 (1.24 %)
$Yplus$	27607 (53.35 %)	288421 (35.43 %)	1465 (0.48 %)	0 (0.00 %)	30773 (1.22 %)
$Yminus$	27559 (53.26 %)	287825 (35.35 %)	1354 (0.45 %)	0 (0.00 %)	27250 (1.08 %)
$\theta_{Z-Hj\,min}$	27311 (52.78 %)	285704 (35.09 %)	1284 (0.42 %)	0 (0.00 %)	24601 (0.97 %)
$\theta_{Z-Hj\,max}$	27031 (52.24 %)	277203 (34.05 %)	1263 (0.42 %)	0 (0.00 %)	24280 (0.96 %)
$b-tagging$	5972 (11.54 %)	4732 (0.58 %)	0 (0.00 %)	0 (0.00 %)	458 (0.02 %)

Table 2: Backgrounds reduction summary in each selection for $ZH \to q\bar{q}b\bar{b}$.

From the reduction summary of Table. 2, $\ell\ell\ell\ell$ four-leptonic background can be suppressed completely by number of particles cut ($N_{PFOs} < 40$) and the remaining backgrounds are $qqqq$ and qq which including b-quarks event after applying the b-tagging.

4 Results

Reconstructed Higgs mass distribution after the selection of $ZH \to q\bar{q}b\bar{b}$ is fitted with the function of Gaussian convoluted Gaussian with the exponential function assuming the background, as shown in Fig. 6. Fitted results of the reconstructed $ZH \to q\bar{q}b\bar{b}$ Higgs mass distribution are summarized in the Table. 3. From the fitted results, Higgs mass ($M_H = 120$ GeV at MC) is reconstructed as $M_H = 120.79 \pm 0.089$GeV and the measurement accuracy of cross-section to $ZH \to q\bar{q}b\bar{b}$ is obtained as $\delta\sigma/\sigma = 5.3\%$.

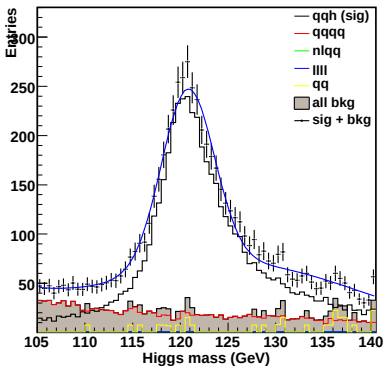

Figure 6: Reconstructed Higgs mass distribution of $ZH \to q\bar{q}b\bar{b}$.

5 Conclusion

Simulation study of the direct reconstruction of the Higgs boson in $ZH \to q\bar{q}b\bar{b}$ four-jet mode with the Higgs mass of 120 GeV at the $\sqrt{s} = 250$ GeV and the integrated luminosity of $\mathcal{L} = 250fb^{-1}$ has performed for the ILD detector model considering with

Higgs mass ($M_H = 120$ GeV at MC)	$M_H = 120.79$ (GeV)
Measurement accuracy of M_H	$\delta M_H = 89$ (MeV)
Measurement accuracy of $\sigma(ZH \to q\bar{q}bb)$	$\delta\sigma/\sigma = 5.3\%$

Table 3: Fitted results for the reconstructed Higgs mass distribution.

the $qqqq$, $\nu\ell qq$ $\ell\ell\ell\ell$, qq background processes. From
the study, measurement accuracy of the reconstructed Higgs mass is estimated as 87 MeV and the measurement accuracy of the cross-section of $ZH \rightarrow q\bar{q}b\bar{b}$ mode is obtained as $\delta\sigma/\sigma = 5.3\%$.

Acknowledgment

I would like to thank to everyone who join the ILC physics WG subgroup [14] for useful discussion of this work and to ILD optimization group members who maintain the softwares and MC samples. This study is supported in part by the Creative Scientific Research Grant No. 18GS0202 of the Japan Society for Promotion of Science and promotion.

References

[1] ILC Reference Design Report (RDR) http://www.linearcollider.org/rdr/

[2] The LEP Electroweak Working Group, arXiv:0811.4682 [hep-ex] (November 2008).

[3] CDF Collaboration and D0 Collaboration, arXiv:0903.4001 [hep-ex].

[4] GLD Detector Outline Document (DOD), arXiv:physics/0607154v1 [physics.ins-det]

[5] http://ilcldc.org/documents/dod

[6] http://www.ilcild.org/

[7] GEANT4 Collaboration: S. Agostinelli *et al.*, Nucl. Instrum. Methods A506, 250 (2003).

[8] http://ilcsoft.desy.de/portal/

[9] http://root.cern.ch/

[10] http://acfahep.kek.jp/subg/sim/simtools/

[11] ACFA Linear Collider Working Group, KEK Report 2001-11, August, 2001.

[12] Proceedings of the APPI Winter Institute, KEK Proceedings 2002-08, July (2002).

[13] S. Yamamoto, K. Fujii and A. Miyamoto, arXiv:0809.4111 [physics.comp-ph].

[14] http://www-jlc.kek.jp/subg/physics/ilcphys/

Measurement of Higgs Branching Ratio at ILC

Kohei Yoshida[(a)]

[(a)] *Department of Physics, Tohoku University, Sendai, Japan*

Measurement of Higgs branching ratio is necessary to investigate Higgs coupling to particle masses. Especially, it is the most important program to measure the branching ratio of $H \to b\bar{b}$ and $H \to c\bar{c}$ at the international linear collider (ILC). We have studied the measurement accuracy of Higgs branching ratio at ILC with $\sqrt{s} = 250$ GeV by using $ZH \to \nu\bar{\nu}H$ events. We obtained the Higgs branching ratio with 1.1% and 13.7% accuracy for $H \to b\bar{b}$ and $H \to c\bar{c}$, respectively.

.

1 Introduction

In the Higgs mechanism, Higgs coupling is proportional to a particle mass. For that reason, it is important to measure the Higgs coupling to particle masses, i.e. Higgs branching ratio, is important to confirm Higgs mechanism and distinguish the Standard Model extensions. Especially, it is the most important program to measure the branching ratio of $H \to b\bar{b}$ and $H \to c\bar{c}$ at ILC [1] with the excellent performance of the flavor tagging.

We have studied the measurement accuracy of Higgs branching ratio at ILC by using $ZH \to \nu\bar{\nu}H$ events. In this paper, we report the measurement accuracy of Higgs branching ratio of $H \to b\bar{b}$ and $H \to c\bar{c}$.

2 Simulation tools

In this study, we used common generator samples in the ILC community for ZH events and standard model backgrounds, which were prepared with WITHERD at SLAC [2]. In this study, the Higgs mass was assumed to be 120 GeV. We used the center of mass energy of $\sqrt{s} = 250$ GeV and the integrated luminosity of 250 fb^{-1}. Here, the beam energy spread was assumed as 0.3% for the electron and positron beam. The beam polarization was set to 80% left-handed for the electron beam and 30% right-handed for the positron beam.

The signal and background events were simulated by the full simulator, Mokka[3], where the detector model is `ILD_00` was implemented as the detector model [4]. Hadronization was done by Pythia6.409, in which the Higgs branching ratio is defined as shown in Table 2 for the Higgs mass of 120 GeV. After the detector simulation, the reconstruction was performed by Marlin[7].

3 Event selection

In this study, the final states of four fermions are considered as background events, where they are classified into 6 groups, $\nu\nu qq$, $qqqq$, $\nu\ell qq$, $\ell\ell qq$, $\nu\nu\ell\ell$ and $\ell\ell\ell\ell$. The signal and

	Branching ratio
$b\bar{b}$	65.7%
W^+W^-	15.0%
$\tau^+\tau^-$	8.0%
gg	5.5%
$c\bar{c}$	3.6%

Table 1: The Higgs branching ratio defined in Pythia6.409.

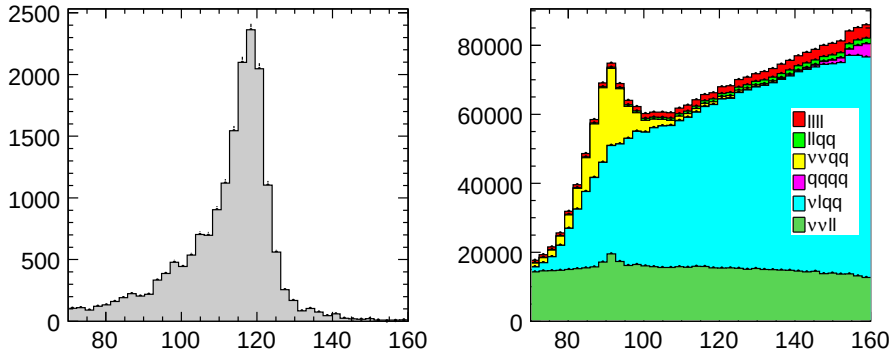

Figure 1: Distribution of the reconstructed di-jet mass for signal (left) and background (right).

background events are summarized in Table 2. All events are reconstructed as 2-jet events by Durham jet algorithm [6]. By using the reconstructed 2 jets, the di-jet mass (M_{jj}) was reconstructed as shown in Fig. 1. Since the background events dominate in the Higgs mass region, the selection cuts were investigated.

At first, we studied the distribution of missing mass ($M_{\rm miss}$). Since a Z boson decays into the neutrino pair in $ZH \to \nu\bar{\nu}H$ events, the missing mass should be consistent with Z boson mass (91.2 GeV). We, therefore, selected the events with 80 GeV $< M_{\rm miss} <$ 140 GeV. Applying this cut, $\ell\ell\ell\ell$, $\ell\ell qq$, and $qqqq$ events were suppressed. Then, we required that the reconstructed di-jet particles have the transverse momentum ($p_{\rm T}$) from 20 to 70 GeV and longitudinal momentum ($p_{\rm L}$) below 60 GeV. We selected the number of charged tracks ($N_{\rm tracks}$) above 10 to remove $W^+W^- \to l^+\nu l^-\bar{\nu}$ events.

After the selection cuts so far, $\tau\nu_\tau qq$ events become the main background. The maximum track momentum in each events ($p_{\rm max}$) were investigated since the charged tracks from τ have relatively higher momentum than those from b-jets. We selected the events with $p_{\rm max} <$ 30 GeV. Y_+ is the threshold y-value to reconstruct 2-jet as 3-jets. Since the final state of $ZH \to \nu\bar{\nu}q\bar{q}$ and $\tau\nu_\tau qq$ is 2 and 3 bodies, respectively, Y_+ for $ZH \to \nu\bar{\nu}q\bar{q}$ events has smaller value than $\tau\nu_\tau qq$ events. On the other hand, Y_-, the y-value to reconstruct 2-jet as 1-jets, has larger value for $ZH \to \nu\bar{\nu}q\bar{q}$ events than $\nu\bar{\nu}qq$ and $l\nu qq$ because β of W and

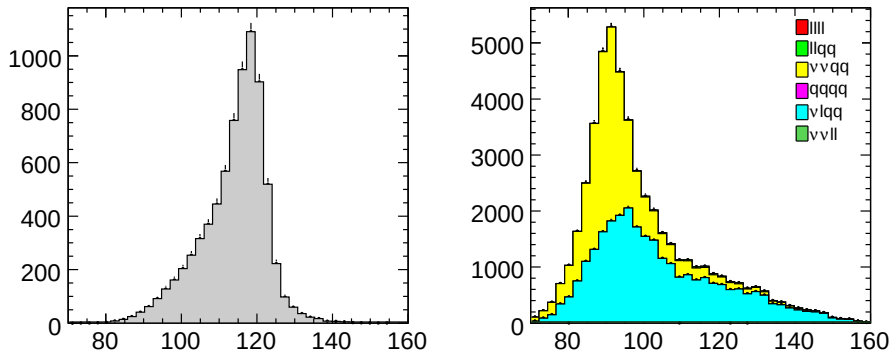

Figure 2: Distribution of the reconstructed di-jet mass after the selection cuts for signal (left) and background (right).

	cross section (fb)	No. of events	No. of events after all cuts	Efficiency (%)
$ZH \to \nu\bar{\nu}H$	77.4	19,360	7,384	38.14
$ZH \to \nu\bar{\nu}bb$	52.2	13,062	6,434	49.26
$ZH \to \nu\bar{\nu}c\bar{c}$	2.83	707	318	44.98
$\nu_e eqq$	5843.2	1,460,797	851	0.06
$\nu_\mu \mu q$	5309.3	1,327,332	2,288	0.17
$\nu_\tau \tau q$	5304.2	1,326,061	24,979	1.88
$\nu_\nu qq$	599.9	149,979	21,653	14.44
Other	25291	6,322,758	335	0.01

Table 2: The number of events for signal and background, and the selection efficiencies after the selection cuts.

Z bosons from decay of WW and ZZ events is larger than Higgs from $ZH \to \nu\bar{\nu}q\bar{q}$. We, therefore, selected $Y_+ < 0.02$ and $0.2 < Y_- < 0.8$.

Finally, the signal region was set to be 100 GeV $< M_{jj} <$ 130 GeV. After all the selection cuts, $\nu\nu qq$ events from WW and ZZ events were reduced as shown in Fig. 2. The number of signal and background events and the selection efficiencies after the selection cut was summarized in Table 2.

4 Measurement of Higgs branching ratio

To measure the Higgs branching ratio of $H \to b\bar{b}$ and $H \to c\bar{c}$, the template fitting was performed [7]. For the template fitting, 3-dimensional histogram for the b-, c-, and bc-likeness was used, which are obtained as output values from LCFIVertex package [8]. In LCFIVertex, neural-net training was done by using $Z \to qq$ events at Z-pole (91.2 GeV) to derive b- and c-likeness. bc-likeness is c-likeness whose neural-net training is done by using

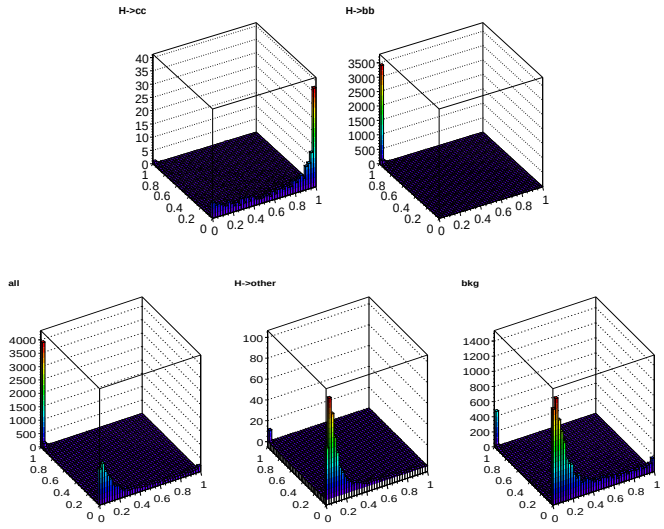

Figure 3: 2-dimensional template histogram for b-likeness and c-likeness.

only $Z \to bb$ events as background. The each flavor-likeness for two jets are combined as,

$$X-\text{likeness} = \frac{X_1 \cdot X_2}{X_1 \cdot X_2 + (1-X_1)(1-X_2)} \tag{4.2}$$

where $X = b$, c or bc. X_1 and X_2 are the flavor-likeness of the first and second jet, respectively.

The template sample is separated into $H \to b\bar{b}$, $H \to c\bar{c}$, $H \to other$, and Standard Model background events. Figure 3 shows the 2-dimensional template histogram for b-likeness and c-likeness. In $H \to other$ sample, $H \to gg$ and $H \to W^-W^+$ events are dominant. Since the both distributions are identical, they are treated in one template sample.

In the template fitting, the fitting parameters (r_{bb}, r_{cc}, r_{oth}, and r_{bkg}) were adjusted to minimize the following χ^2 function:

$$\chi^2 = \sum_{i=1}^{n_b}\sum_{j=1}^{n_c}\sum_{k=1}^{n_{bc}} \frac{(N_{ijk}^{data} - \sum_s r_s(\frac{N^{ZH}}{N^s})N_{ijk}^s - r_{bkg}N_{ijk}^{bkg})^2}{N_{ijk}^{all}}, \tag{4.3}$$

where s shows $b\bar{b}$, $c\bar{c}$ and $other$. r_{bb}, r_{cc}, r_{oth} are the fraction of $H \to b\bar{b}$, $H \to c\bar{c}$, $H \to others$ in ZH events after the selection cut, where we set $r_{other} = 1 - r_{cc} - r_{bb}$. r_{bkg} is the normalization factor of the Standard Model background. N_{ijk}^s are the number of expected events in (i, j, k) bin of the 3-dimensional histogram.

To estimate the reconstruction accuracy of r_{bb} and r_{cc}, the fitting was done for 1,000 times by using Toy-MC. Figure 4 shows the distributions of r_{bb} and r_{cc} obtained by the fitting. r_{bb} and r_{cc} were determined to be 0.87 ± 0.01 and 0.046 ± 0.009, respectively. These mean values are consistent with the true r_{bb} (0.87) and r_{cc} (0.046). From the result, if the

	r_{bkg}: free	$r_{bkg} = 1$
BR($H \to b\bar{b}$)	1.1%	1.1%
BR($H \to c\bar{c}$)	13.7%	13.6%
BR($H \to c\bar{c}/H \to b\bar{b}$)	13.3%	13.3%

Table 3: The measurement accuracy of Higgs branching ratio. For measurement accuracy of BR($H \to b\bar{b}$) and BR($H \to c\bar{c}$), it is assumed that the cross section of ZH is determined by other measurements.

cross section of $e^+e^- \to ZH$ can be determined with other measurements like a measurement of the Higgs recoil mass [9] and the selection efficiencies of $ZH \to \nu\bar{\nu}b\bar{b}$ and $ZH \to \nu\bar{\nu}c\bar{c}$ are known, Higgs branching ratio of $H \to b\bar{b}$ and $H \to c\bar{c}$ can be measured with accuracy of 1.1% and 13.7%, respectively.

To evaluate the influence of Standard Model background on determination of the Higgs branching ratio, we performed the template fitting, fixing r_{bkg} to 1. r_{bb} and r_{cc} were determined to be 0.87 ± 0.01 and 0.046 ± 0.006, respectively. It corresponds to the measurement accuracy of 1.1% and 13.6% for r_{bb} and r_{cc}, respectively. From this result, it was found that the fluctuation of the background normalization has only negligible effects on the measurement of Higgs branching ratio.

Without any other measurement, we can measure the relative branching ratio between $H \to b\bar{b}$ and $H \to c\bar{c}$ by analysis of only $ZH \to \nu\bar{\nu}H$ events as follows:

$$\frac{BR(H \to c\bar{c})}{BR(H \to b\bar{b})} = \frac{r_{cc}/\epsilon_{cc}}{r_{bb}/\epsilon_{bb}}, \tag{4.4}$$

where ϵ_{bb} and ϵ_{cc} are the selection efficiencies of $H \to b\bar{b}$ and $H \to c\bar{c}$ events as shown in Table 2. The relative branching ratio of 0.054 ± 0.007 was obtained for the template fitting with free and fixed r_{bkg}, which corresponds to 13.3% accuracy. The measurement accuracy for Higgs branching ratio is summarized in Table 3.

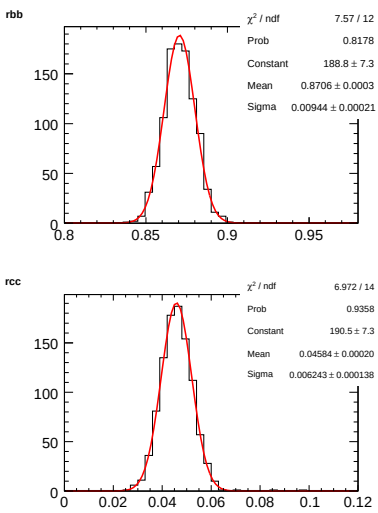

Figure 4: Distribution of r_{bb} (Upper) and r_{cc} (Lower) obtained by the template fitting.

5 Conclusion

Measurement of Higgs branching ratio is necessary to investigate Higgs coupling to particle masses. Especially, it is the most important program to measure the branching ratio of $H \to b\bar{b}$ and $H \to c\bar{c}$ at ILC. We have studied the measurement accuracy of Higgs branching ratio at ILC with $\sqrt{s} = 250$ GeV by using $ZH \to \nu\bar{\nu}H$ events. For Higgs mass of 120 GeV and the integrated luminosity of 250 fb^{-1}, we obtained the measurement accuracy of 1.1% and 13.7% for $H \to b\bar{b}$ and $H \to c\bar{c}$, respectively, assuming that the cross section of ZH is determined by other measurements. Finally, the relative branching ratio between $H \to b\bar{b}$ and $H \to c\bar{c}$ was obtained with 13.3% accuracy.

6 Acknowledgments

The authors would like to thank all the members of the ILC physics subgroup [16] for useful discussions and ILD optimization working group. This study is supported in part by the Creative Scientific Research Grant No. 18GS0202 of the Japan Society for Promotion of Science.

References

[1] INTERNATIONAL LINEAR COLLIDER REFERENCE DESIGN REPORT, ILC Global Design Effort and World Wide Study.

[2] http://ilcsoft.desy.de/portal/data_samples/.

[3] http://ilcsoft.desy.de/portal/software_packages/mokka/.

[4] http://www.ilcild.org.

[5] http://ilcsoft.desy.de/portal/software_packages/marlin/.

[6] S. Catani *et al.*, Phys. Lett. B269 (1991) 179;
N. Brown, W. J. Stirling, Z. Phys. C53 (1992) 629.

[7] Thorsten Kuhl and Klaus Desch, LC-PHSM-2007-001.

[8] LCFIVertex package Reference Manual, http://ilcsoft.desy.de/portal/software_packages/lcfivertex/.

[9] P. Garcia-Abia and W. Lohmann, Eur. Phys. J. direct C2, 2 (2000).

[10] http://www-jlc.kek.jp/subg/physics/ilcphys/.

Analysis of Higgs Self-coupling with ZHH at ILC

Yosuke Takubo[(a)]*

[(a)] *Department of Physics, Tohoku University, Sendai, Japan*

Measurement of the cross-section of $e^+e^- \to ZHH$ offers the information of the trilinear Higgs self-coupling, which is important to confirm the mechanism of the electro-weak symmetry breaking. Since there is huge background in the signal region, background rejection is key point to identify ZHH events. In this paper, we study the possibility to observe the ZHH events at ILC by using $ZHH \to \nu\bar{\nu}HH/q\bar{q}HH$ events.

1 Introduction

In the standard model, particle masses are generated through the Higgs mechanism. This mechanism relies on a Higgs potential, $V(\Phi) = \lambda(\Phi^2 - \frac{1}{2}v^2)^2$, where ϕ is an iso-doublet scalar field, and v is the vacuum expectation value of its neutral component ($v \sim 246$ GeV). Determination of the Higgs boson mass, which satisfies $m_H^2 = 2\lambda v^2$ at tree level in the standard model, will provide an indirect information about the Higgs potential and its self-coupling, λ_{HHH}. The measurement of the trilinear self-coupling, $\lambda_{HHH} = 6\lambda v$, offers an independent determination of the Higgs potential shape and the most decisive test of the mechanism of the electro-weak symmetry breaking.

λ_{HHH} can be extracted from the measurement of the cross-section for the Higgs-strahlung process (σ_{ZHH}), $e^+e^- \to ZHH$. For a Higgs mass of 120 GeV, the W fusion process is negligible at $\sqrt{s} = 500$ GeV. Figure 1 shows the relevant Feynman diagrams for this process. The information of λ_{HHH} is included in the diagram of Fig. 1(a), and the relation between the cross-section of ZHH and λ_{HHH} is characterized by $\frac{\Delta\lambda_{HHH}}{\lambda_{HHH}} \sim 1.75\frac{\Delta\sigma_{ZHH}}{\sigma_{ZHH}}$, where $\Delta\lambda_{HHH}$ and $\Delta\sigma_{ZHH}$ are measurement accuracy of λ_{HHH} and σ_{ZHH}, respectively [1]. For that reason, precise measurement of the cross-section for the ZHH production is essential to determination of the strength of the trilinear Higgs self-coupling.

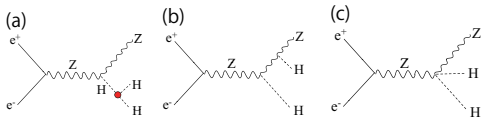

Figure 1: The relevant Feynman diagrams for the ZHH production. The trilinear self-coupling is included in (a).

We have studied the feasibility for observation of ZHH events at the ILC. For the analysis, we assumed a Higgs mass of 120 GeV, $\sqrt{s} = 500$ GeV, and an integrated luminosity of 2 ab^{-1}. The final states of the ZHH production can be categorized into 3 types, depending on the decay modes of Z: $ZHH \to q\bar{q}HH$ (135.2 ab^{-1}), $ZHH \to \nu\bar{\nu}HH$ (38.8 ab^{-1}), and $ZHH \to \ell\bar{\ell}HH$ (19.8 ab^{-1}), where the cross-sections were calculated without the beam polarization, initial-state radiation, and beamstrahlung. In this paper, we report status of the analysis with $ZHH \to \nu\bar{\nu}HH/q\bar{q}HH$events.

*MAIL: takubo@epx.phys.tohoku.ac.jp

2 Simulation tools

We have used MadGraph [10] to generate $ZHH \to \nu\bar{\nu}HH/q\bar{q}HH$ and $tbtb$ events, where top quarks in $tbtb$ events are decayed by using DECAY package in MadGraph. $ZZ \to bbbb$, tt, and ZH events have been generated by Physsim [11]. In this study, the beam polarization, initial-state radiation, and beamstrahlung have not been included in the event generations. We also have ignored the finite crossing angle between the electron and positron beams. In both event generations, helicity amplitudes were calculated using the HELAS library [12], which allows us to deal with the effect of gauge boson polarizations properly. Phase space integration and the generation of parton 4-momenta have been performed by BASES/SPRING [10]. Parton showering and hadronization have been carried out by using PYTHIA6.4 [13], where final-state tau leptons are decayed by TAUOLA [14] in order to handle their polarizations correctly.

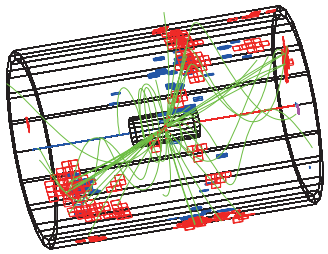

Figure 2: A typical event display of $ZHH \to \nu_\mu\bar{\nu}_\mu HH$.

The generated Monte Carlo events have been passed to a detector simulator called JSFQuickSimulator, which implements the GLD geometry and other detector-performance related parameters [15]. Figure 2 shows a typical event display of $ZHH \to \nu_\mu\bar{\nu}_\mu HH$.

3 Analysis

3.a $ZHH \to \nu\bar{\nu}HH$

For the Higgs mass of 120 GeV, the Higgs boson mainly decays into $b\bar{b}$ (76% branching ratio in MadGraph). Therefore, we concentrated on $ZHH \to \nu\bar{\nu}b\bar{b}b\bar{b}$ from $\nu\bar{\nu}HH$ events. As background events, we considered $ZZ \to bbbb$ (9.05 fb), tt (583.6 fb), ZH (62.1 fb), and $tbtb$ (1.2 fb). They have much larger cross-sections than ZHH, necessitating powerful background rejection.

The clusters in the calorimeters are combined to form a jet if the two clusters satisfy $y_{ij} < y_{\rm cut}$, where y_{ij} is y-value of the two clusters. All events are forced to have four jets by adjusting $y_{\rm cut}$. Then, mass of the Higgs boson was reconstructed to identify $\nu\bar{\nu}HH$ events by minimizing χ^2 value defined as

$$\chi^2 = \frac{({}^{\rm rec}M_{H1} - {}^{\rm true}M_H)^2}{\sigma_{H1}^2} + \frac{({}^{\rm rec}M_{H2} - {}^{\rm true}M_H)^2}{\sigma_{H2}^2}, \tag{3.5}$$

where ${}^{\rm rec}M_{H1,2}$, ${}^{\rm true}M_{H1,2}$, and $\sigma_{H1,2}$ are the reconstructed Higgs mass, the true Higgs mass (120 GeV), and the Higgs mass resolution, respectively. $\sigma_{H1,2}$ was evaluated for each reconstructed Higgs boson by using $31\%/\sqrt{E_{\rm jet}}$, where $E_{\rm jet}$ is the jet energy. Figure 3 shows the distri-

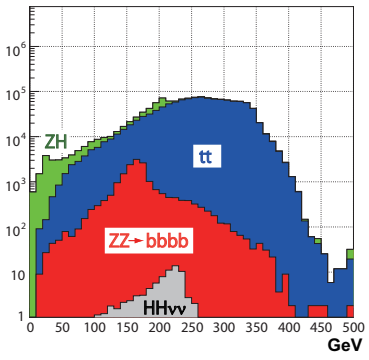

Figure 3: Distribution of the sum of the two reconstructed Higgs masses for $\nu\bar{\nu}HH$ and background events.

bution of the sum of the two reconstructed Higgs boson masses for $\nu\bar{\nu}HH$ and background events. With no selection cuts, the signal is swamped in huge number of background events.

To identify the signal events from the backgrounds, we applied the following selection cuts. We required $\chi^2 < 20$ and 95 GeV$< M_{H1,2} <$ 125 GeV to select events, for which the Higgs bosons could be well reconstructed. Since Higgs mainly decay into a b-quark pair, the reconstructed mass distribution have a tail in lower mass region due to missing energy by neutrinos from decay processes of the b-quark. For that reason, the mass cut is applied asymmetrically against the Higgs mass. Then, since a Z boson is missing in $\nu\bar{\nu}HH$ events, we set the selection cut on the missing mass ($^{\rm miss}M$): 90 GeV $<^{\rm miss} M <$ 170 GeV.

The angular distribution of the particles reconstructed as the Higgs bosons has a peak at $\cos\theta = \pm 1$ for ZZ events whereas the distribution becomes more uniform in $\nu\bar{\nu}HH$ events. We applied the angular cut of $|\cos\theta_{\rm H1,2}| < 0.9$ to reject these ZZ events.

The 4-jet events from ZH events have small missing transverse momentum ($^{\rm miss}P_{\rm T}$), which contaminate in the signal region. For that reason, we required $^{\rm miss}P_{\rm T}$ above 50 GeV.

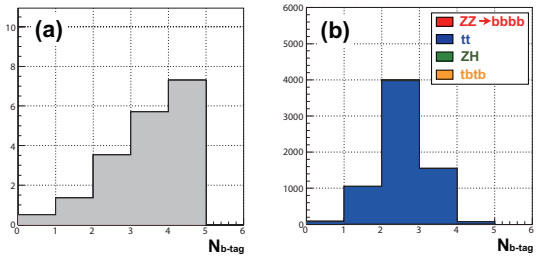

Figure 4: Distribution of the number of jets tagged as b-jets after the selection cuts for $\nu\bar{\nu}HH$ (a) and backgrounds (b).

After the selection cuts so far, the dominant background was tt events. The leptonic decay mode of W from $t \to bW$ can be rejected by indentifying isolated charged leptons. We define the energy deposit within 20 degree around a track as E_{20}. The isolated lepton track was defined to be a track with 10 GeV $< E_{20} < \frac{2}{11}E_{\rm trk} - 1.8$ GeV, where $E_{\rm trk}$ is energy of the lepton track. We required the number of isolated lepton tracks ($N_{\rm lepton}$) to be zero.

Finally, the flavor tagging was applied. We identified a jet as a b-jet, when it has 2 tracks with 3-sigma separation from the interaction point. Figure 4 shows the distribution of the number of jets tagged as b-jets after the selection cuts ($N_{\rm b-tag}$). Since the Higgs boson decays into $b\bar{b}$ with a 76% branching ratio, $\nu\bar{\nu}HH$ events have a peak at $N_{b-\rm tag} = 4$, whereas tt events have a peak at 2. To reject the tt events effectively, we selected events with $N_{b-\rm tag} = 4$.

Figure 5 shows the distribution of the sum of the two reconstructed Higgs masses for $ZHH \to \nu\bar{\nu}HH$ after all the selection cuts. We summarize the reduction rate by each selection cut in Table 1. Finally, we obtained 7.3 events for $\nu\bar{\nu}HH$ and 69.2 events for backgrounds. This result corresponds to a signal significance of 0.8 ($= 7.3/\sqrt{7.3 + 69.2}$). For observation of the ZHH production, further background rejection, especially tt events, is necessary.

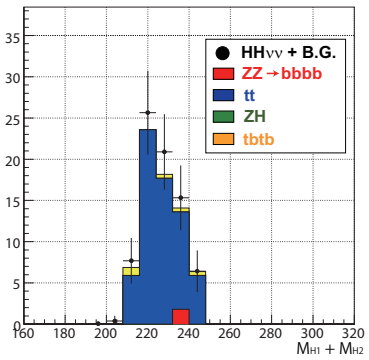

Figure 5: Distribution of the sum of the two reconstructed Higgs boson masses for $ZHH \to \nu\bar{\nu}HH$ after all the selection cuts.

	$\nu\bar{\nu}HH$	$ZZ \to bbbb$	tt	ZH	$tbtb$
No cut	77.6	18,100	1,167,200	124,200	2,154
$\chi^2 < 20$	43.7	12,169	364,921	83,065	468
95 GeV$< M_{H1,2} <$ 125 GeV	29.5	387	70,557	8,570	82
90 GeV$<^{\rm miss} M <$ 170 GeV	26.2	127	32,570	696	45
$\lvert\cos\theta_{H1,2}\rvert < 0.9$	23.0	34.4	26,521	447	37
$^{\rm miss}P_{\rm T} > 50$ GeV	18.4	3.6	17,591	137	25
$N_{\rm lepton} = 0$	17.8	3.6	6,708	37.3	9.7
$N_{\rm b-tag} = 4$	7.3	1.8	65	0	2.4

Table 1: Cut statistics.

	$qqHH$	tt	$tbtb$
No cut	270	1,167,200	124,200
$\chi^2 < 20$	219	615,456	1,810
90 GeV$< M_{H1,2} <$ 150 GeV	214	600,899	1,781
60 GeV$< M_Z <$ 120 GeV	213	595,533	1,771
$N_{\rm lepton} = 0$	193	467,154	1,240
$^{\rm miss}E < 70$ GeV	170	352,061	943
$N_{\rm b-tag} = 6$	4.6	0	0.6

Table 2: Cut statistics.

3.b $ZHH \to q\bar{q}HH$

For the analysis of $qqHH$, all the events are reconstructed as 6-jet events, adjusting the y-value. Here, we considered tt and $tbtb$ events as background events. The masses of the Higgs and Z boson were reconstructed by minimizing χ^2 value defined as

$$\chi^2 = \frac{(^{\rm rec}M_{H1} - ^{\rm true}M_H)^2}{\sigma_{H1}^2} + \frac{(^{\rm rec}M_{H2} - ^{\rm true}M_H)^2}{\sigma_{H2}^2} + \frac{(^{\rm rec}M_Z - ^{\rm true}M_Z)^2}{\sigma_Z^2}, \tag{3.6}$$

where $^{\rm rec}M_{H1,2}$, $^{\rm rec}M_Z$, $^{\rm true}M_{H1,2}$, and $^{\rm true}M_Z$ are the reconstructed Higgs and Z mass and the true Higgs and Z mass, respectively. $\sigma_{H1,2}$ and σ_Z are the Higgs and Z mass resolution, respectively, which are defined in Sec 3.a.

We required $\chi^2 < 20$, 90 GeV$< M_{H1,2} <$ 150 GeV, and 60 GeV$< M_Z <$ 120 GeV to select events, for which the Higgs and Z bosons could be well reconstructed. Then, the isolated lepton track was searched to indentify the lepton tracks from decay of top quarks in tt and $tbtb$ events. We required the number of isolated lepton tracks ($N_{\rm lepton}$) to be zero. Since the missing energy of the signal is smaller than tt and $tbtb$ events, $^{\rm miss}E < 70$ GeV was required. Finally, we applied the b-tagging whose requirement is the same as the analysis for $\nu\bar{\nu}HH$events. Here, we required that all the jets are b-jets, $N_{\rm b-tag} = 6$.

After all the cut, we obtained 4.6 events for $qqHH$ and 0.6 events for the background. That corresponds to the signal significance of 2.0 ($= 4.6/\sqrt{4.6+0.6}$). The number of the events at each selection cut is summarized in Table 2.

4 Summary

$ZHH \to \nu\bar{\nu}HH/q\bar{q}HH$ processes were studied to investigate the possibility of the trilinear Higgs self-coupling at the ILC. In this study, we assumed the Higgs boson mass of 120 GeV, $\sqrt{s} = 500$ GeV, and the integrated luminosity of 2 ab^{-1}. After the selection cuts, the signal significance of 0.8 and 2.0 was obtained for $\nu\bar{\nu}HH$ and $q\bar{q}HH$events, respectively. To extract the information of λ_{HHH}, we must improve the flavor tagging to reject background events effectively.

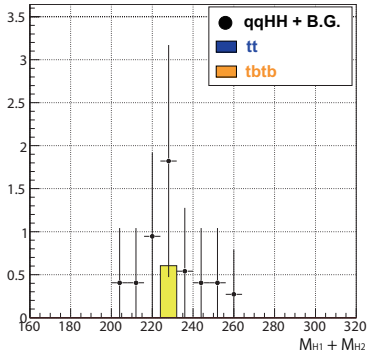

Figure 6: Distribution of the sum of the two reconstructed Higgs boson masses for $ZHH \to q\bar{q}HH$ after all the selection cuts.

5 Acknowledgments

The authors would like to thank all the members of the ILC physics subgroup [16] for useful discussions. This study is supported in part by the Creative Scientific Research Grant No. 18GS0202 of the Japan Society for Promotion of Science, and Dean's Grant for Exploratory Research in Graduate School of Science of Tohoku University.

References

[1] C. Castanier, P. Gay, P. Lutz, J Orloff, arXive:hep-ex/0101028.

[2] http://madgraph.hep.uiuc.edu/.

[3] http://acfahep.kek.jp/subg/sim/softs.html.

[4] H. Murayama, I. Watanabe, K. Hagiwara, KEK-91-11, (1992) 184.

[5] T. Ishikawa, T. Kaneko, K. Kato, S. Kawabata,*Comp, Phys. Comm.* **41** (1986) 127.

[6] T. Sjòstrand, *Comp, Phys. Comm.* **82** (1994) 74.

[7] http://wasm.home.cern.ch/wasm/goodies.html.

[8] GLD Detector Outline Document, arXiv:physics/0607154.

[9] http://www-jlc.kek.jp/subg/physics/ilcphys/.

Study of Higgs Self-coupling at ILC

Junping Tian[(a)], **Keisuke Fujii**[(b)], and **Yuanning Gao**[(a)]

[(a)] *Tsinghua University, Beijing 100084, People's Republic of China*
[(b)] *High Energy Accelerator Research Organization (KEK), Tsukuba, Japan*

In this Analysis we investigated the possibility of the measurement of Higgs self-coupling at ILC through the process $e^+ + e^- \to ZHH$ using fast simulation data. So far two combinations of decay modes: $Z \to q\bar{q}, H \to b\bar{b}, H \to WW^*$ and $Z \to l\bar{l}, H \to b\bar{b}, H \to b\bar{b}$ were studied. Our preliminary results show that it is very challenging to suppress the huge standard model backgrounds effectively.

1 Introduction

It is well accepted that the discovery of a Higgs-like boson is not enough to fully understand the mechanism of electro-weak symmetry breaking (EWSB) and mass generation. The Higgs self-coupling can be a non-trivial probe of the Higgs potential and probably the most decisive test of the EWSB mechanism. In the standard model framework, the Higgs potential $V(\Phi) = \lambda(\Phi^2 - \frac{1}{2}v^2)^2$, where Φ is an isodoublet scalar field and $v \approx 246$ GeV is the vacuum expectation value of its neutral component, is uniquely determined by the self-coupling λ. Obviously, determination of the Higgs mass, which satisfies $m_H^2 = 2\lambda v^2$ at tree level, can provide an indirect information about the self-coupling. The measurement of the trilinear self-coupling $\lambda_{HHH} = 6\lambda v$ offers direct independent determination of the Higgs potential shape, which is the topic of this analysis.

The trilinear Higgs self-coupling can be measured at ILC through the two leading processes: double Higgs-strahlung [1, 2] and WW fusion [2, 3, 4, 5, 6], which are shown in Fig.1. The former is expected to dominate around the center of mass energy of 500 GeV and the latter to take it over at higher energy. In this analysis we focus on the double Higgs-strahlung process $e^+ + e^- \to ZHH$ for the Higgs mass of $M_H = 120$ GeV and the center of mass energy of $\sqrt{s} = 500$ GeV with the integrated luminosity 2 ab^{-1}.

Depending on the different decay modes of Z and H, there are different methods to identify the signal events. Table I shows several most promising combinations of decay modes for $e^+ + e^- \to ZHH$ and their branching ratios. Modes 1 and 3 are studied in Ref. [7]. We study the other two modes in this analysis.

2 Simulation

The simulations of signal events ($e^+ + e^- \to ZHH$) and possible background events ($e^+ + e^- \to t\bar{t}, ZZZ, W^+W^-Z, ZZ, ZH$) were done by Physsim [11]. In Physsim the helicity amplitudes are calculated by the HELAS library [12]. The phase space integration and the

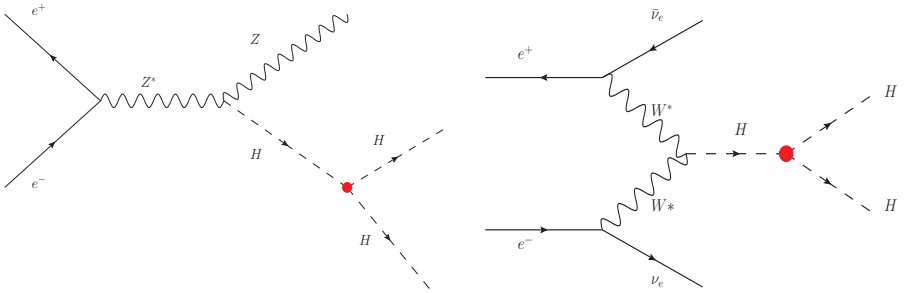

Figure 1: Leading processes involving trilinear Higgs self-coupling: (Left) Double Higgs-strahlung; (Right) WW fusion.

Table 1: Most promising modes for $e^+ + e^- \to ZHH$

Decay Mode	$Z \to$	$H_1 \to$	$H_2 \to$	Branching Ratio
1	$q\bar{q}$	$b\bar{b}$	$b\bar{b}$	34%
2	$q\bar{q}$	$b\bar{b}$	WW^*	14%
3	$\nu\bar{\nu}$	$b\bar{b}$	$b\bar{b}$	9.8%
4	$l\bar{l}$	$b\bar{b}$	$b\bar{b}$	4.9%

four momenta generation are performed by BASES/SPRING [10]. Parton showering and hadronization are carried out by PYTHIA6.4 [13], where final-state τ leptons are decayed by TAUOLA [14] in order to handle their polarizations correctly. The detector simulation was done by JSFQuickSimulator, which implements the GLD geometry and other detector-performance related parameters [13].

It is worth mention of that the simulations were performed without the beam polarization but with the initial-state radiation, beam width and beamstrahlung. Then the cross sections used here are shown in Table II. An integrated luminosity of 2 ab^{-1} is assumed in this analysis.

Table 2: Cross sections of the related processes

Process	Cross section
$e^+ + e^- \to ZHH$	152 ab
$e^+ + e^- \to t\bar{t}$	530 fb
$e^+ + e^- \to ZZZ$	800 ab
$e^+ + e^- \to W^+W^-Z$	36 fb
$e^+ + e^- \to ZZ$	515 fb
$e^+ + e^- \to ZH$	70 fb

3 Analysis

3.a $e^+ + e^- \to ZHH \to (q\bar{q})(b\bar{b})(WW^*)$

The full hadronic decays of W and W^* were investigated. In this mode the final state of a candidate signal event contains of 8 jets, two of which are b jets. To select the signal events, first we find all the good tracks and require the number of tracks be greater than 20. We then try to combine tracks with a small Y value to a current jet cluster, where the Y value between two momenta p_1, p_2 is defined as $Y(p_1, p_2) = \frac{M^2(p_1,p_2)}{E_{vis}}$, with $M(p_1, p_2)$ being the invariant mass of p_1, p_2 and E_{vis} the total visible energy. We continue the jet clustering until there are 7 jets left, because the two jets coming from W^* are very close to each other which means the Y-value between them is very small, thereby being likely to be clustered as one jet. At this point we calculate the Y values for all the pairs from these 7 jets and choose the minimum denoted by Y_{cut}. The Y_{cut} distributions of signal events and background events (here we consider the $t\bar{t}$ events as background) are shown in Fig.2. The 7 jets are combined by minimizing the χ^2 which is defined as

$$\chi^2 = \frac{(M(b,\bar{b}) - M_H)^2}{\sigma_{H_1}^2} + \frac{(M(W,W^*) - M_H)^2}{\sigma_{H_2}^2} + \frac{(M(q,\bar{q}) - M_Z)^2}{\sigma_Z^2} + \frac{(M(q,\bar{q}') - M_W)^2}{\sigma_W^2}$$

where $M(q, q')$ is the reconstructed invariant mass of jet q and jet q', M_H, M_Z and M_W are the mass of H, Z and W, respectively, and $\sigma_{H_1}, \sigma_{H_2}, \sigma_Z and \sigma_W$ are their corresponding mass resolutions.

In order to further suppress the background, we require that $\chi^2 < 20, 90\text{GeV} < M(H_1) < 130\text{GeV}, 110\text{GeV} < M(H_2) < 150\text{GeV}, 70\text{GeV} < M(Z) < 110\text{GeV}, Y_{cut} > 0.0076$, where the asymmetry of two Higgs mass requirement is due to their different decay modes. The preliminary result of this cut-based analysis is shown in Table III. Though we can still add other cuts like b tagging requirement, the signal events will become too few to be observed. It seems very challenging to reject the huge $t\bar{t}$ background in this mode.

We are going to investigate the semi-lepton decays of W and W^*.

Table 3: Cut statistics of $e^+ + e^- \to ZHH \to (q\bar{q})(b\bar{b})(WW^*)$

Process	$ZHH \to (q\bar{q})(b\bar{b})(WW^*)$	$t\bar{t}$
theoretical	18.3	1062000
pre-selection	12.6	483949
$\chi^2 < 20$	5.2	65144
$90GeV < M_{H_1} < 130GeV$	5.1	63157
$110GeV < M_{H_2} < 150GeV$	3.6	36670
$90GeV < M_Z < 110GeV$	3.5	34359
$Y_{cut} > 0.005$	2.3	8454
$Y_{cut} > 0.0076$	1.1	2644

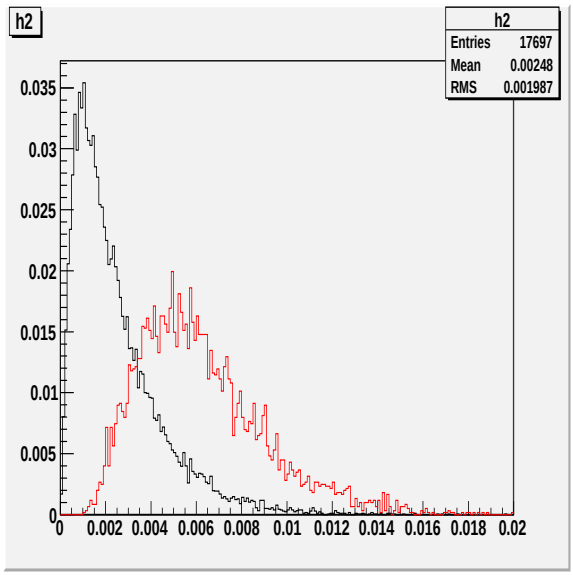

Figure 2: Distribution of Y_{cut}, where black is for signal and red is for $t\bar{t}$ background.

3.b $e^+ + e^- \to ZHH \to (l\bar{l})(b\bar{b})(b\bar{b})$

In this mode a candidate signal event contains two leptons and four b jets, where we only consider the Z boson decaying into e^+e^- and $\mu^+\mu^-$. The two isolated charged lepton tracks are required to have an energy greater than 20 GeV and the energy deposited in the cone of 20° around each lepton track be less than 20 GeV. We then force the other tracks to four jets and combine the four jets by minimizing the χ^2 defined by

$$\chi^2 = \frac{(M(b,\bar{b}) - M_H)^2}{\sigma_{H_1}^2} + \frac{(M(b,\bar{b}) - M_H)^2}{\sigma_{H_2}^2} + \frac{(M(l,\bar{l}) - M_Z)^2}{\sigma_Z^2}.$$

Table IV shows that 15.4 signal events survived the pre-selection but with thousands times more background events left. In order to reject the background effectively, while keeping a reasonable signal efficiency, we used the neural net method MLP in the TMVA package [14] which gives some useful classifiers. Here we mainly consider the five kinds of backgrounds that are shown in Table IV. First we separately do the neural net analysis between the signal and each of the five kinds of backgrounds. For each event we can get five classifiers to separate signal and backgrounds. Figure 3 histograms the classifiers obtained by the MLP method for the signal and $t\bar{t}$ samples.

We then add some more cuts on the five classifiers denoted by $mva\_tt, mva\_zzz, mva\_wwz, mva\_zz$ and mva_zh as shown in Table IV. We further impose cuts on the Z mass, Y_{cut}, and require b tagging, which is based on the number of tracks with 2.5σ separation from the interaction point. Our preliminary result is listed in Table IV. The final cut is applied with the neural net for the signal and the ZZZ background after all of the above cuts. We end up with 3

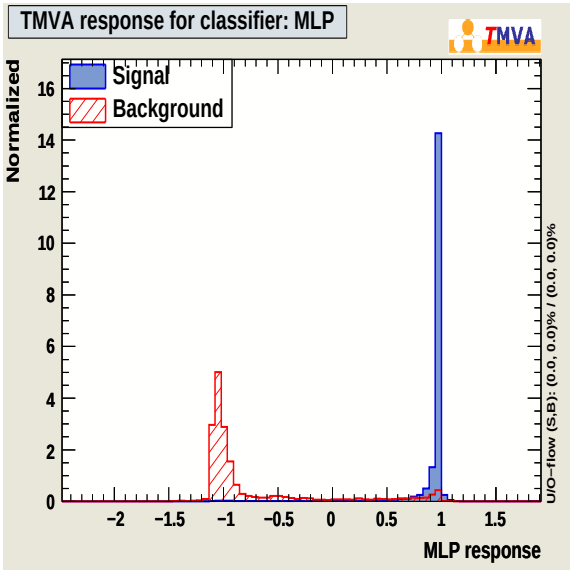

Figure 3: The classifier obtained by neural net training for signal and $t\bar{t}$ background.

signal events with 0.82 ZZZ events left, while four backgrounds are eliminated. The result shows that the ZHH events can be observed in this mode with the significance $\frac{S}{\sqrt{S+B}} \sim 1.5\sigma$.

4 Summary

The two modes, $e^+ + e^- \to ZHH \to (q\bar{q})(b\bar{b})(WW^*)$ and $e^+ + e^- \to ZHH \to (l\bar{l})(b\bar{b})(b\bar{b})$, were investigated for the purpose of the measurement of the trilinear Higgs self-coupling at ILC for $M_H = 120$ GeV, $\sqrt{s} = 500$ GeV and the integrated luminosity of 2 ab^{-1}. The former mode is very difficult to use for the signal observation, while the latter mode can be useful to observe the self-coupling.

5 Acknowledgments

We would like to thanks all the members of the ILC physics subgroup [15] for useful discussions. This study is supported in part by KEK, Center of High Energy Physics, Tsinghua University and the JSPS Core University Program.

References

[1] G. Gounaris, D. Schildknecht and F. Renard, Phys. Lett. **B83** (1979) 191 and (**E**) **89B** (1980) 437; V. Barger, T. Han and R.J.N. Phillips, Phys. Rev. **D38** (1988) 2766.

[2] V.A. Ilyin, A.E. Pukhov, Y. Kurihara, Y. Shimizu and T. Kaneko, Phys. Rev. **D54** (1996) 6717.

[3] F. Boudjema and E. Chopin, Z. Phys. **C73** (1996) 85.

[4] V. Barger and T. Han, Mod. Phys. Lett. **A5** (1990) 667.

[5] A. Dobrovolskaya and V. Novikov, Z. Phys. **C52** (1991) 427.

Table 4: Cut statistics of $e^+ + e^- \to ZHH \to (l\bar{l})(b\bar{b})(b\bar{b})$

Process	ZHH	$t\bar{t}$	ZZZ	WWZ	ZZ	ZH
generated	1M	4.5M	500K	750K	1.25M	250K
theoretical	304	1062000	1600	72300	1030000	140000
pre-selection	15.4	9023	125	1943	3560	1618
$mva\_tt > 0.98$ $mva\_wwz > 1.0$ $mva\_zz > 0.97$ $mva\_zh > 0.97$ $mva\_zzz > 0$	11.7	312	12.9	12.7	16.5	5.6
$70GeV < M_Z < 110GeV$	9.7	106	11.7	7.5	16.5	0.56
$Y_{cut} > 0.015$	9.1	91.3	10.6	6.9	6.6	0
$2b(H_1)(N_{off} > 0)$	6.3	28	5.5	1.8	0	0
$2b(H_2)(N_{off} > 1)$	3.5	0.71	2.3	0	0	0
$mva\_zzz > 0.86$	3.0	0	0.82	0	0	0

[6] D.A. Dicus, K.J. Kallianpur and S.S.D. Willenbrock, Phys, Lett. **B200** (1988) 187; A. Abbasabadi, W.W. Repko, D.A. Dicus and R. Vega, Phys. Rev. **D38** (1988) 2770; Phys. Lett. **B213** (1988) 386.

[7] Y. Takubo, arXiv:0907.0524v1.

[8] http://acfahep.kek.jp/subg/sim/softs.html.

[9] H. Murayama, I. Watanabe, K. Hagiwara, KEK-91-11, (1992) 184.

[10] T. Ishikawa, T. Kaneko, K. Kato, S. Kawabata, Comp. Phys. Comm. **41** (1986) 127.

[11] T. Sj ostrand, Comp. Phys. Comm. **82** (1994) 74.

[12] http://wasm.home.cern.ch/wasm/goodies.html.

[13] GLD Detector Outline Document, arXiv:physics/0607154.

[14] A. Hoecker, P. Speckmayer, J. Stelzer, J. Therhaag, E. von Toerne, H. Voss *et al.*, arXiv:physics/0703039v5.

[15] http://www-jlc.kek.jp/subg/physics/ilcphys.

Feasibility study of the forward-backward asymmetry of the $e^+e^- \to t\bar{t}$ process in all-hadronic decay modes at $\sqrt{s} = 500$ GeV with the ILD detector

Katsumasa Ikematsu[(a)*], **Akiya Miyamoto**[(a)], and **Keisuke Fujii**[(a)],

[(a)] *High Energy Accelerator Research Organization (KEK), Tsukuba, 305-0801, Japan*

We have studied the measurement accuracy of the forward-backward asymmetry of the $e^+e^- \to t\bar{t}$ process in the 6-jet mode at $\sqrt{s} = 500$ GeV with the ILD detector. In the analysis the vertex charges of b-jets were used to distinguish t from $\bar{t}$ in each event. The distribution of the cosine of the reconstructed polar angle of so identified t or $\bar{t}$ showed a clear forward-backward asymmetry. After the correction for charge misidentification the forward-backward asymmetry was determined to be $A^t_{FB} = 0.334 \pm 0.0079$ for 500 fb^{-1} with the beam polarization combination of $P(e^+, e^-) = (+30\%, -80\%)$, demonstrating a very good statistical accuracy ($\sim 2\%$) even in the 6-jet mode.

1 Introduction

The forward-backward asymmetry of the $e^+e^- \to t\bar{t}$ process is sensitive to the $t\bar{t}Z$ and $t\bar{t}\gamma$ couplings and serves as a probe for new physics, which may appear as anomaly in these couplings.

Needless to say we have to distinguish t from $\bar{t}$ in each event in order to measure the forward-backward asymmetry, A^t_{FB}. In the lepton+4-jet mode, it is straightforward because the lepton charge tells the charge of the leptonically decayed W, and hence identifies its parent to be either t or $\bar{t}$. In the 6-jet mode, however, we need some other way to separate t and $\bar{t}$, which is non-trivial. Nevertheless it is worth investigating the feasibility of A^t_{FB} measurement in the 6-jet mode, since it has a major branching fraction of 46%. In addition, the kinematical fit works better in the 6-jet mode than in the lepton+4-jet mode, where a large energy is taken away by the neutrino from the leptonically decayed W. The 6-jet mode might, hence, be advantageous when the influence of beamstrahlung is significant.

In this paper, we use the vertex charges of b jets to distinguish t from $\bar{t}$ in each event. The measurement of the vertex charges requires a high performance detector system as well as a sophisticated reconstruction algorithm. The forward-backward asymmetry in the 6-jet mode is therefore a very good measure for the overall performance of a detector system, hence being included as one of the ILC LoI benchmarks [1]. The benchmark conditions are the center of mass energy of $\sqrt{s} = 500$ GeV, an integrated luminosity of 500 fb^{-1}, and a beam polarization combination of $P(e^+, e^-) = (+30\%, -80\%)$.

The ILD [2] is equipped with an unprecedentedly excellent vertex detector, which allows efficient b-jet charge identification with the vertex charge. The vertex charges of b jets were

*Corresponding author. e-mail address: Katsumasa.Ikematsu@kek.jp

reconstructed by the LCFIVertex algorithm [3].

This paper is organized as follows. After we briefly describe our analysis framework in section 2, we move on to the vertex charge reconstruction and show how well we can identify each jet as b or $\bar{b}$ in section 3. We then apply this to $t/\bar{t}$ identification for the determination of the production angle distribution ($dN/d\cos\theta_t$) in section 4. After the correction for charge misidentification we derive the A_{FB}^t and discuss the result in comparison with the Monte Carlo truth in section 5. Section 6 summarizes our analysis and concludes this paper.

2 Analysis framework

In general, Monte Carlo (MC) simulation consists of the following steps: event generation, detector simulation, event reconstruction, and data analysis.

All of the MC event samples, both the signal and the backgrounds, used in this study were produced in the StdHep [5] format by a SLAC team [4] as common inputs to LoI studies, using WHIZARD 1.4 [6] for generating parton 4-momenta and PYTHIA 6.2 [7] for parton-showering and hadronization. The beam energy spread and the beamstrahlung were properly taken into account using the spectrum generated with Guinea-Pig [8] for the default ILC design parameters at $\sqrt{s} = 500\,\mathrm{GeV}$.

The final-state particles output in the StdHep format from the event generation step were passed to a Geant4-based detector simulator called Mokka [9] and swum through the ILD detector to create exact hits in trackers and calorimeters.

These exact hits were smeared or digitized, if necessary, depending on the detector elements in the first part of MarlinReco [10] [11]. The pattern recognition was done for the smeared tracker hits, separately in the TPC and the silicon detectors and so found track segments were then linked together and fed into a Kalman-filter-based track fitter in the second part of MarlinReco. From the fitted tracks and the calorimeter hits, individual particles were reconstructed as particle flow objects (PFO) with a sophisticated particle flow algorithm called PandoraPFA [12] in the third part of MarlinReco.

These PFOs were forced to cluster into 6 jets for the signal and all background events with Durham jet clustering algorithm [13] in the fourth part of MarlinReco.

The next step is heavy flavour tagging with LCFIVertex [3]. The LCFIVertex package consists of two parts. The first part is to search for secondary and tertiary vertices inside each jet and locate them, thereby determining the decay length, the transverse mass, and the momentum at each of these vertices. In the second part these quantities are translated into the impact parameter joint probability and the highest two impact parameter significances, which are used as inputs into a neural net (NN) trained with jet samples having 0 and 1 or more secondary vertices. Each reconstructed jet is then assigned with the three NN outputs, corresponding to b-, c-, and bc-tags.

Once a bottom-flavoured jet is identified we can determine whether it is b or $\bar{b}$ by measuring the vertex charge. We will discuss this in detail in section 3.

The reconstruction of $e^+e^- \to t\bar{t}$ events in 6-jet final states has been studied extensively in the context of the top quark mass measurement. The top quark mass in the 6-jet mode is one of the benchmark observables for ILC LoIs and the ILD study has been reported in reference [2]. Similar to the top quark mass measurement, the measurement of the forward-backward asymmetry requires a correct jet-parton association. In this paper we employed the same reconstruction algorithm as those used for the top quark mass measurement. For the reconstruction, therefore, we refers the readers to the above reference.

3 Vertex charge reconstruction and its performance for a single *b*-jet

In principle, we can tell which three jets are from top and the rest from anti-top in the 6-jet final state by identifying either a $b/\bar{b}$-jet or a $c/\bar{c}$-jet from W^+/W^- decay as shown in Fig. 1. In this analysis, however, we used only $b/\bar{b}$-jets for the top/anti-top separation.

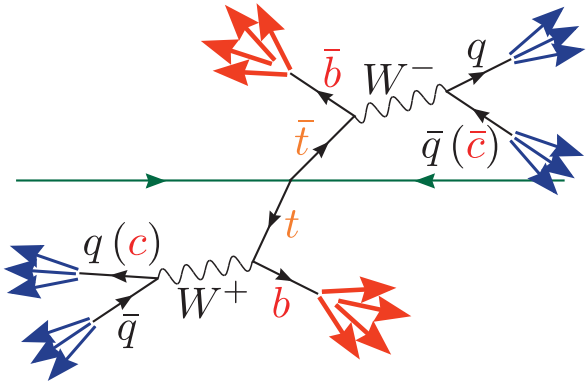

Figure 1: Schematic diagram showing fully hadronic decay channel of $e^+e^- \to t\bar{t}$ process

A bottom quark hadronizes into a B-hadron, which flies over a finite distance thanks to its large $c\tau$, making a secondary vertex significantly away from the primary vertex and hence identifiable by the vertex detector. We define the vertex charge as the sum of the charges of the charged tracks associated with the secondary vertex. If the charged tracks are reconstructed and associated perfectly, the vertex charge is equal to the charge of the primary B-hadron, from which the charge sign of the $b/\bar{b}$ is uniquely determined.

In practice, however, there is no perfect vertexing, and the resultant distribution of the vertex charges of charged B-hadrons will have a finite width and hence their charges might sometimes be mis-identified. By the same token, the charges of neutral B-hadrons might be mis-identified, causing confusion in bottom charge sign identification.

Figure 2 shows the distribution of the MC level vertex charge, which is defined by the charge of a B-meson ($B^\pm$ or B^0) involved in the jet tagged as a b-jet.

Inspection of the figures tells us that we can separate B^+s from B^-s by selecting jets with negative or positive vertex charges with some contamination from B^0s.

Figure 3 shows the distribution of the reconstructed vertex charges of the jets which are b-tagged. In this distribution the b-quark ($\bar{b}$-quark) contribution is shown by hatched blue (red).

The charge sign identification efficiency for a single b-jet using the vertex charge is 28% with a purity of 75%. Notice that only 40% of the b-jets hadronize into charged B-hadrons and hence maximum efficiency one can hope for is 40% in this method.

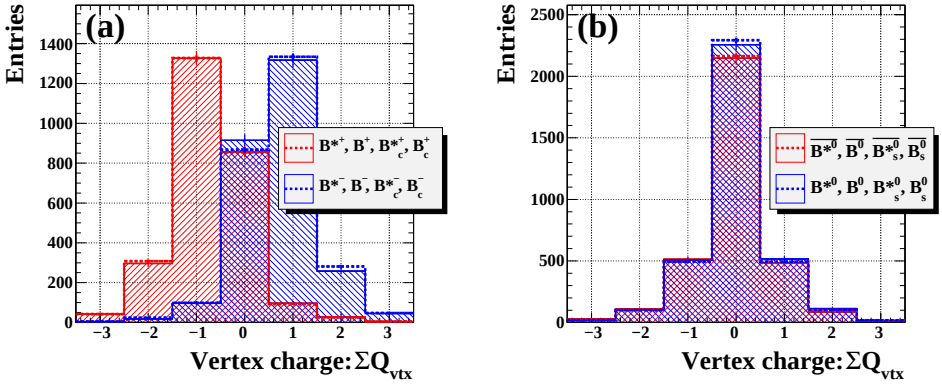

Figure 2: Reconstructed vertex charge distributions for (a) charged B-mesons and (b) neutral B-mesons as separated using MC truth information (PDG particle ID code).

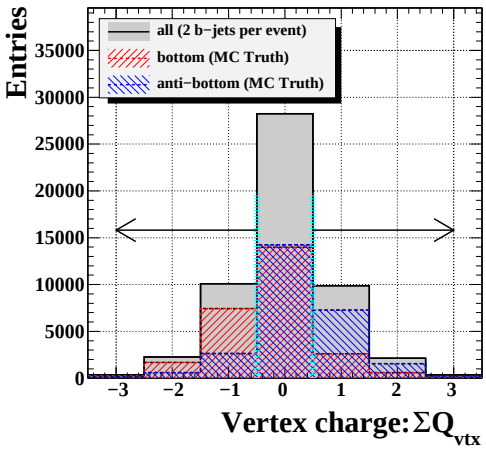

Figure 3: Reconstructed vertex charge distributions for b-quarks (hatched red) and $\bar{b}$-quarks (hatched blue), as identified using MC truth information, shown together with that of all the reconstructed b-jets (solid gray).

4 t and $\bar{t}$ identification and determination of the production angle distribution ($dN/d\cos\theta_t$)

Let's call two reconstructed top systems t_1 and t_2 and b-tagged jets associated to them b_1 and b_2, respectively, The identification of t and $\bar{t}$ is performed by using the vertex charges of b_1 and b_2 as follows. We define c_i ($i = 1$ and 2) as the vertex charge of b_i and $C \equiv c_1 - c_2$ as the event charge. If C is 0, the event is thrown away as we cannot tell t from $\bar{t}$. If C is positive, t_1 is t, while if C is negative, t_1 is $\bar{t}$. The typical distribution of the event charge C is shown in Fig. 4.

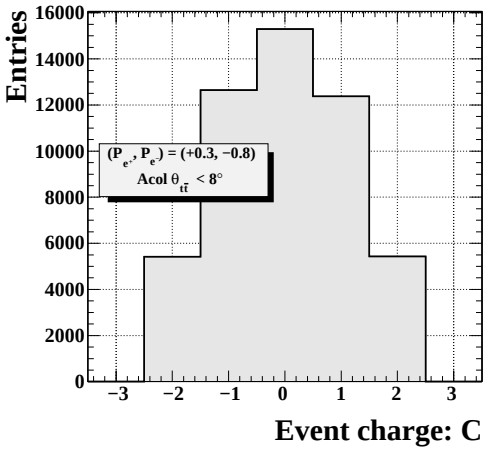

Figure 4: Distribution of event charge: $C = c_1 - c_2$.

Figures 5-(a) through -(i) show the distributions of the production angle of t_1 for 9 possible combinations of the signs of the vertex charges: c_1 and c_2, for the samples where both W bosons decayed into light quarks.

We can see a clear forward-backward asymmetry in the case of $C \neq 0$ (Figs. 5-(a) to -(f)). Notice also that in the first row (-(a) to -(c)) t_1 is t while in the second row (-(d) to -(f)) t_1 is $\bar{t}$, and hence showing opposite asymmetries. On the other hand, in the case of $C = 0$, for which the charge signs of both b-jets were undetermined or they were inconsistent (both b_1 and b_2 had the same sign), there is no forward-backward asymmetry visible. In each figure the contribution from the events with wrong charge sign is hatched red, showing an opposite forward-backward asymmetry. Hatched blue is that from the combinatorial background in which the reconstructed b-jet candidates were not actually b-jets, showing no forward-backward asymmetry.

The combinatorial background depends on the flavour into which W bosons decay. Figures 6-(a) through -(i) are the same figures as Figs. 5-(a) through -(i), but plotted for the samples where one of the two W bosons decayed into a $c/\bar{c}$-quark. Figures 7-(a) through -(i) are similar figures for the samples where both W bosons decayed into $c/\bar{c}$-quarks. We

can see clearly that the combinatorial background grows with the number of c-jets in the final states, since the probability of mis-identifying charm as bottom increases.

If C is positive, t_1 is t, while if C is negative, t_1 is $\bar{t}$. If we can assume that t_1 and t_2 are back-to-back, the production angle of t is obtained from the angle of t_1 as

$$cos\theta_t \equiv \sigma_C \cdot |\cos\theta_{t_1}|, \tag{4.7}$$

where σ_C is the sign of C. In order to test this assumption we compared the distributions for t_1 with those of t_2 after reflection (hatched green) in Figs. 5, 6, and 7-(d) to -(f). This comparison confirmed the assumption[†], allowing us to use Eq. (4.7) to combine all the figures with $C \neq 0$. The selection efficiency of this cut is 69%.

The differential cross section for $e^+e^- \rightarrow t\bar{t}$ and consequently its forward-backward asymmetry (A^t_{FB}) depend on the center-of-mass energy of the $t\bar{t}$ system, which, in turn, depends on the amount of initial state radiation and beamstrahlung. In order to make A^t_{FB} well-defined, we hence rejected events with $\sqrt{\hat{s}}$ significantly less than 500 GeV, by requiring the acollinearity between t_1 and t_2 to be less than 8°. This final cut discarded 24% of the events so far survived. The overall selection efficiency is 20% for fully hadronic $t\bar{t}$ events.

The resultant production angle distribution is shown in Fig. 8. Of the final sample 83% have correctly identified signs of top quark charge.

5 Determination of A^t_{FB}

The production angle distribution Fig. 8 is distorted by the charge mis-identification. The distortion can be corrected by using the following formulae:

$$\begin{cases} dN_{\rm obs}(\theta) &= p(\theta)\cdot\eta(\theta)\cdot\mathcal{L}\cdot d\sigma(\theta) + \bar{p}(\pi-\theta)\cdot\eta(\pi-\theta)\cdot\mathcal{L}\cdot d\sigma(\pi-\theta) + dB(\theta) \\ dN_{\rm obs}(\pi-\theta) &= p(\pi-\theta)\cdot\eta(\pi-\theta)\cdot\mathcal{L}\cdot d\sigma(\pi-\theta) + \bar{p}(\theta)\cdot\eta(\theta)\cdot\mathcal{L}\cdot d\sigma(\theta) + dB(\pi-\theta) \end{cases} \tag{5.8}$$

where $\eta(\theta)$ is the acceptance, $p(\theta)$ ($\bar{p}(\theta)$) is the probability of correctly (wrongly) assigning the charge sign at production angle θ, and $\mathcal{L}$ is the integrated luminosity.

$p(\theta)$ and $\bar{p}(\theta)$ are plotted in Fig. 9 as the black and red lines, respectively.

The figure shows no θ-dependency, allowing us to set $p(\theta) = p$ and $\bar{p}(\theta) = \bar{p}$. Solving for $d\sigma(\theta)$, we thus obtain the following formula for the differential cross section:

$$d\sigma(\theta) = \frac{p\cdot(dN_{\rm obs}(\theta) - dB(\theta)) - \bar{p}\cdot(dN_{\rm obs}(\pi-\theta) - dB(\pi-\theta))}{(p^2-\bar{p}^2)\eta(\theta)\cdot\mathcal{L}}. \tag{5.9}$$

Figure 10 shows the production angle distribution after the correction for the charge mis-identification.

The acceptance function $\eta(\theta)$ is in general θ-dependent. In our case, however, it turned out at that the θ-dependence was negligible[‡]. The acceptance hence cancels out in the calculation of the forward-backward asymmetry, resulting in

$$A^t_{FB} = \frac{\int_{0<\theta<\pi/2} dN(\theta) - \int_{\pi/2<\theta<\pi} dN(\theta)}{\int_{0<\theta<\pi/2} dN(\theta) + \int_{\pi/2<\theta<\pi} dN(\theta)}, \tag{5.10}$$

[†]Strictly speaking, Eq. (4.7) does not hold on an event-by-event basis because of initial state radiation and beamstrahlung. On average, however, t_1 and t_2 are back-to-back, allowing us to merge the six cases with $C \neq 0$.

[‡]Notice that for the reconstructed t or $\bar{t}$, being a 3-jet system, there is no acceptance hole even at $\theta = 0$ or π.

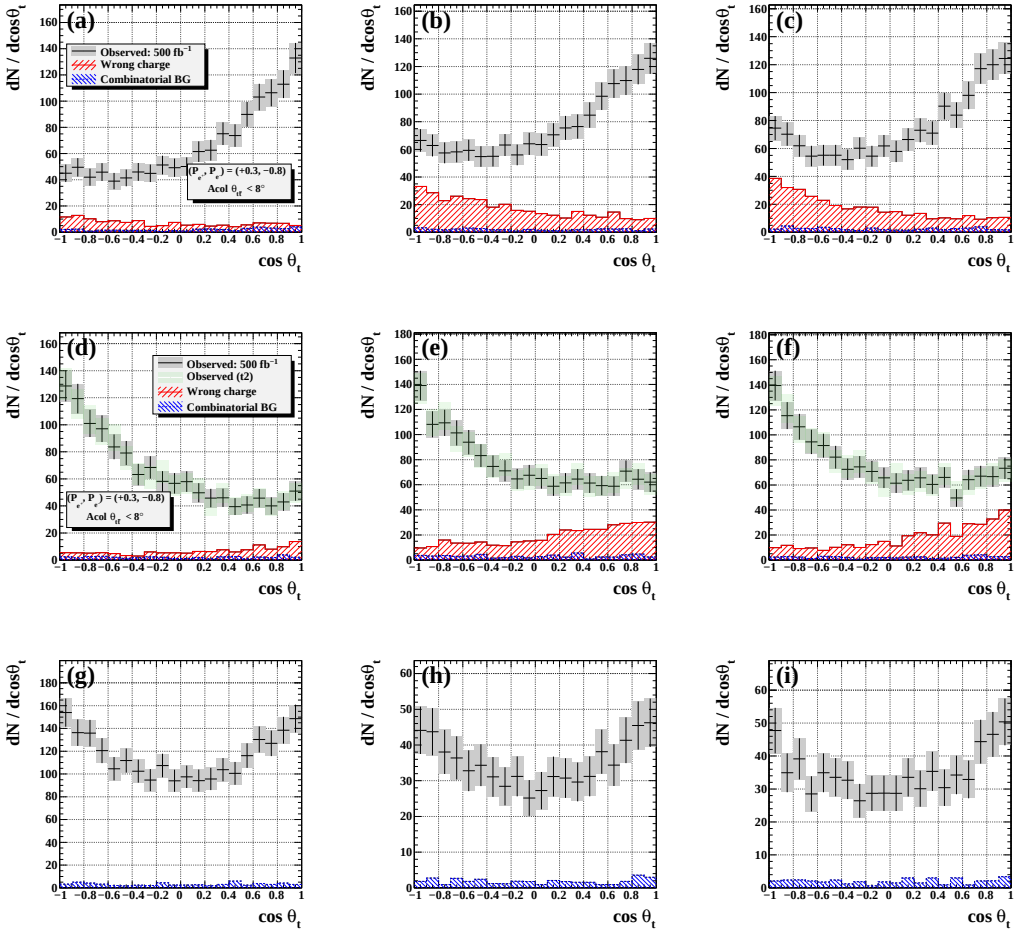

Figure 5: Distributions of the reconstructed polar angle of the identified top quark in fully-hadronic $t\bar{t}$ events, which are tagged as (Q_{b_1}, Q_{b_2}) = (a) $(+,-)$, (b) $(+,0)$, (c) $(0,-)$, (d) $(-,+)$, (e) $(-,0)$, (f) $(0,+)$, (g) $(0,0)$, (h) $(+,+)$, and (i) $(-,-)$ for the sample in which both W bosons decayed into light-quark pairs (***bbuddu*** sample).

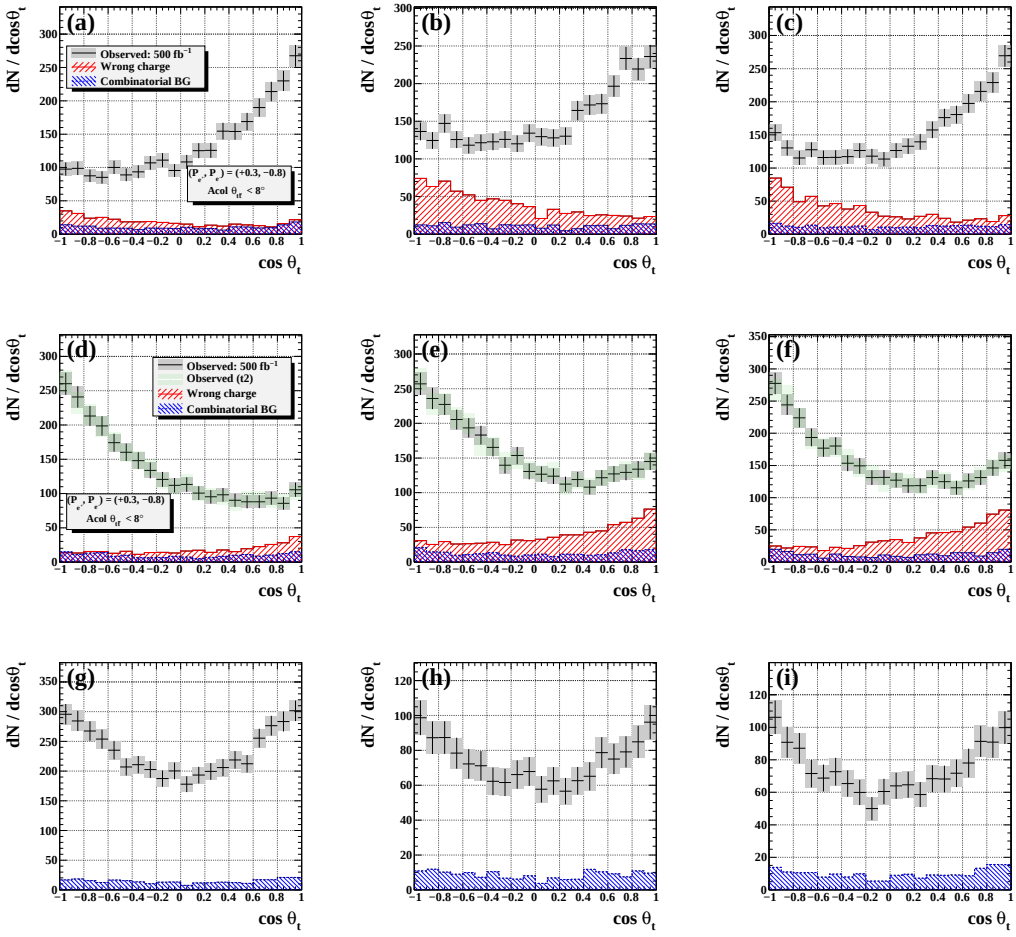

Figure 6: Distributions of the reconstructed polar angle of the identified top quark in fully-hadronic $t\bar{t}$ events, which are tagged as (Q_{b_1}, Q_{b_2}) = (a) $(+,-)$, (b) $(+,0)$, (c) $(0,-)$, (d) $(-,+)$, (e) $(-,0)$, (f) $(0,+)$, (g) $(0,0)$, (h) $(+,+)$, and (i) $(-,-)$ for the samples in which one of the two W bosons decayed into a $c/\bar{c}$-quark (***bbudsc/bbcsdu*** samples).

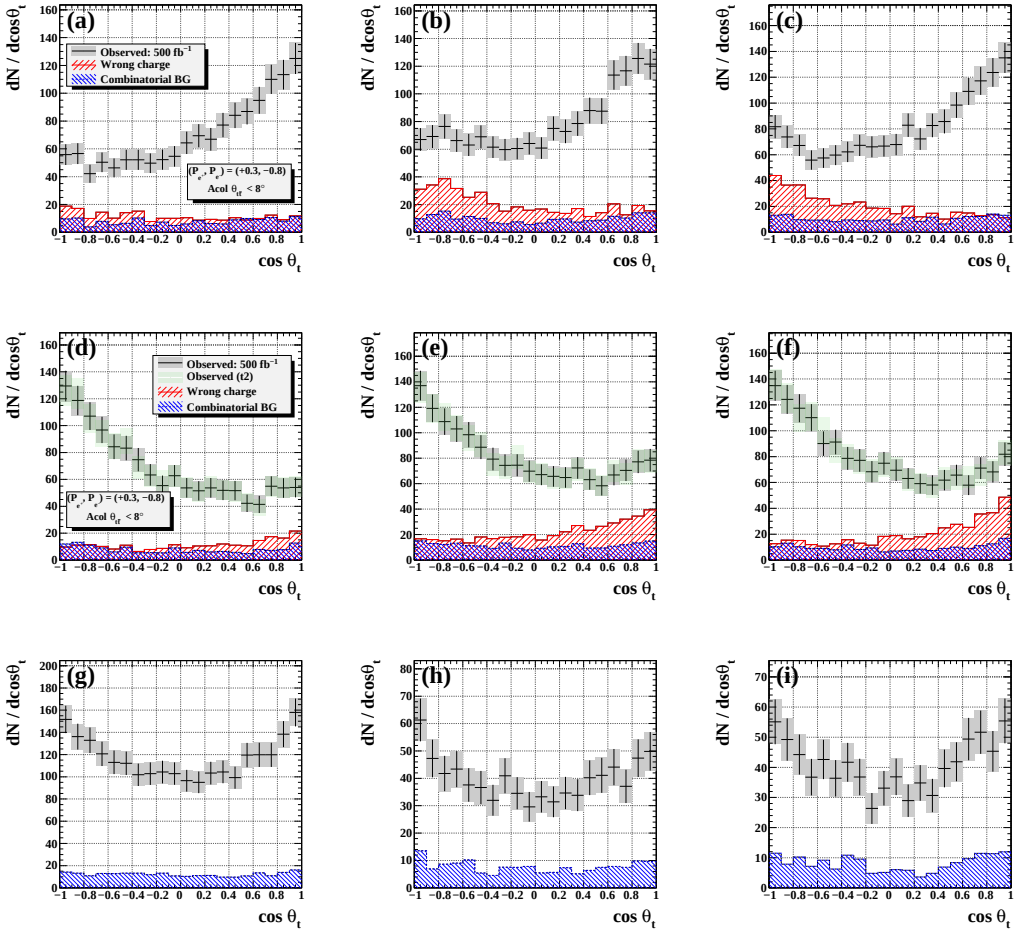

Figure 7: Distributions of the reconstructed polar angle of the identified top quark in fully-hadronic $t\bar{t}$ events, which are tagged as (Q_{b_1}, Q_{b_2}) = (a) $(+,-)$, (b) $(+,0)$, (c) $(0,-)$, (d) $(-,+)$, (e) $(-,0)$, (f) $(0,+)$, (g) $(0,0)$, (h) $(+,+)$, and (i) $(-,-)$ for the sample in which both W bosons decayed into $c/\bar{c}$-quarks (***bbcssc*** sample).

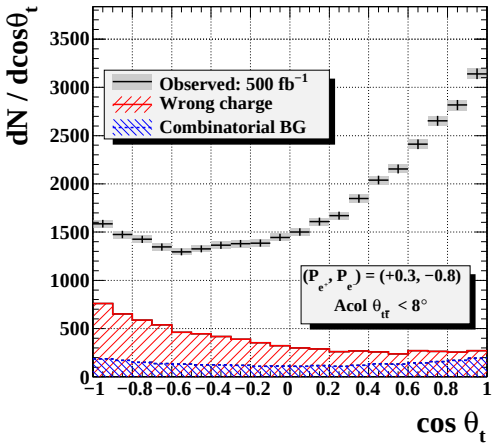

Figure 8: Distribution of the reconstructed polar angle of the identified top quark in fully-hadronic $t\bar{t}$ events. The contributions from events with the wrong charge (red) and the case where the b-quark is mis-identified are also shown (blue).

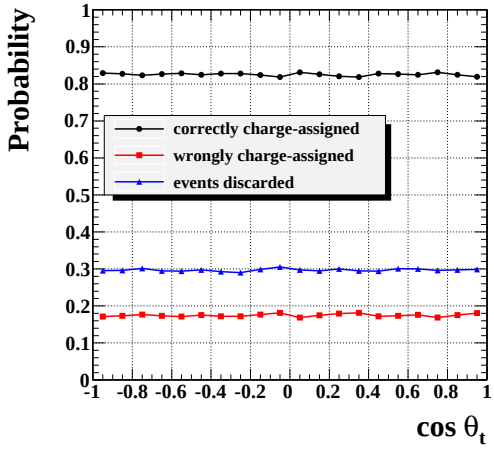

Figure 9: $\cos\theta_{t1}$ dependence of the charge-sign identification (black) and mis-identification (red) probabilities.

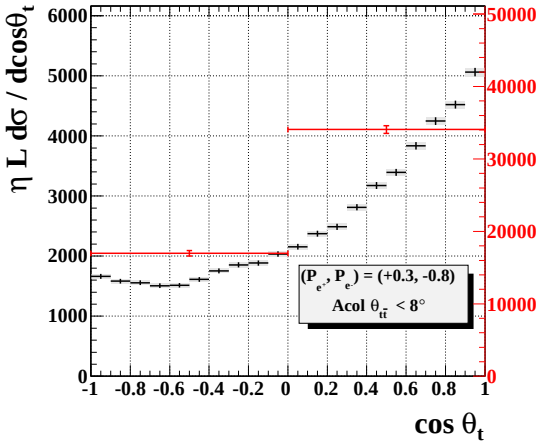

Figure 10: $\cos\theta_{t1}$ distribution after the correction for the charge mis-identification.

where $dN(\theta) \equiv \eta \cdot \mathcal{L} \cdot d\sigma(\theta)$.

From Fig. 10 we finally obtain

$$A_{FB}^{t} = 0.334 \pm 0.0079 \text{ (stat.)}, \tag{5.11}$$

where the center of mass energy of $\sqrt{s} = 500$ GeV, an integrated luminosity of $500\,\text{fb}^{-1}$, and a beam polarization combination of $P(e^+, e^-) = (+30\%, -80\%)$.

6 Summary

We have studied the measurement accuracy of the forward-backward asymmetry with the ILD detector for the $e^+e^- \to t\bar{t}$ process in the 6-jet mode at $\sqrt{s} = 500$ GeV. In the analysis the vertex charges of b-jets were used to identify t and $\bar{t}$. The efficiency to tag the vertex charge of a b-jet was 28% with the purity of 75%. Having two b-jets in each event, the probability to identify t and $\bar{t}$ in the event was 71% with the probability of wrong charge assignment of 12%. The measured angular distribution was corrected for wrong $t/\bar{t}$ charge assignments. From the number of events in forward and backward hemispheres after the correction, we obtained $A_{FB}^{t} = 0.334 \pm 0.0079$, where quoted error is statistical only.

Acknowledgments

The authors wish to thank all the members of the ILD optimization group for useful discussions and comments. This study is supported in part by the Creative Scientific Research Grant No. 18GS0202 of the Japan Society for Promotion of Science (JSPS) and the JSPS Core University Program.

References

[1] "Benchmark Reactions for the ILC LOI process", The WWSOC Software panel, http://ilcdoc.linearcollider.org/record/14681/files/Benchmark_Reactions_for_t he_ILC_LOI.pdf

[2] The ILD Letter of Intent, http://www.ilcild.org/documents/ild-letter-of-intent/

[3] D. Bailey *et al.* [LCFI Collaboration], Nucl. Instrum. Meth. A **610**, 573 (2009) [arXiv:0908.3019 [physics.ins-det]].

[4] Standard Model Data Samples, https://confluence.slac.stanford.edu/display/ilc/Standard+Model+Data+Samples

[5] StdHep, http://cepa.fnal.gov/psm/stdhep/

[6] W. Kilian, T. Ohl, and J. Reuter, "WHIZARD: Simulating Multi-Particle Processes at LHC and ILC" [arXiv: 0708.4233 [hep-ph]].

[7] T. Sjostrand, L. Lonnblad, and S. Mrenna, "PYTHIA 6.2: Physics and manual" [arXiv:hep-ph/0108264].

[8] D. Schulte, Ph. D. Thesis, University of Hamburg 1996 [TESLA-97-08].
D. Schulte, M. Alabau, P. Bambade, O. Dadoun, G. Le Meur, C. Rimbault and F. Touze, *In the Proceedings of Particle Accelerator Conference (PAC 07), Albuquerque, New Mexico, 25-29 Jun 2007, pp 2728.*

[9] P. Mora de Freitas and H. Videau, [LC-TOOL-2003-010].

[10] F. Gaede, Nucl. Instrum. Meth. A **559**, 177 (2006).

[11] O. Wendt, F. Gaede and T. Kramer, Pramana **69**, 1109 (2007) [arXiv:physics/0702171].

[12] M. A. Thomson, Nucl. Instrum. Meth. A **611**, 25 (2009) [arXiv:0907.3577 [physics.ins-det]].

[13] Yu. L. Dokshitzer. *J. Phys. G* **17**, 1537 (1991).

A study of top-quark Yukawa coupling measurement in $e^+e^- \to t\bar{t}H$ at $\sqrt{s} = 500\,\mathrm{GeV}$

Ryo Yonamine[(a)], **Katsumasa Ikematsu**[(b)], **Satoru Uozumi**[(c)], and **Keisuke Fujii**[(b)]

[(a)] *The Graduate University for Advanced Studies, Tsukuba, Japan*
[(b)] *IPNS, KEK, Tsukuba, Japan*
[(c)] *Department of Physics, Kobe University, Kobe, Japan*

We report on the feasibility of measuring the top Yukawa coupling in the process: $e^+e^- \to t\bar{t}H$. This measurement is crucial to test the mass generation mechanism for matter particles. Since the cross section for this process attains its maximum around $\sqrt{s} = 700\,\mathrm{GeV}$, most of the past studies were done assuming this energy region. It has been pointed out, however, that the QCD threshold correction enhances the cross section significantly and might enable its measurement at $\sqrt{s} = 500\,\mathrm{GeV}$, which will be accessible already in the first phase of the ILC project. We have implemented this threshold enhancement into our $t\bar{t}H$ event generator and carried out Monte Carlo simulations. Our results show that $t\bar{t}H$ events can be observed with a significance of $4.1\,\sigma$ with no beam polarization and $5.4\,\sigma$ with the e^- and e^+ beam polarization combination: $(-0.8, +0.3)$.

.

1 Introduction

The standard model of elementary particle physics is based on two pillars: one is the gauge principle and the other is the electroweak symmetry breaking and mass generation mechanism. The first pillar, the gauge principle, has been tested by precision electroweak measurements. On the other hand, the second pillar has not yet been tested. In order to confirm this second pillar we have to measure the Higgs self-coupling and the top Yukawa coupling.

In this study, we investigate the feasibility of measuring the top Yukawa coupling at 500 GeV with the process: $e^+e^- \to t\bar{t}H$. Since the top quark is the heaviest among all the matter particles, the measurement of its Yukawa coupling will be the most decisive test of the mass generation mechanism for matter particles. Since the cross section for the $e^+e^- \to t\bar{t}H$ process is 2-3 fb even near its maximum reached at around $\sqrt{s} = 700\,\mathrm{GeV}$, most of the past studies assumed the measurement energy in this region[1]. It has been pointed out, however, that the QCD threshold correction enhances the cross section significantly[2] and might open up the possibility of measuring the top Yukawa coupling at $\sqrt{s} = 500\,\mathrm{GeV}$, which is within the scope of the first phase of the ILC project. In order to investigate this possibility we have implemented this threshold enhancement into our $t\bar{t}H$ event generator and carried out Monte Carlo simulations.

In the next section we begin with clarifying the signatures of the $t\bar{t}H$ production and list up possible background processes that might mimic the signal. We then describe our analysis framework used for event generations and detector simulations in section 3. The

event selection procedure for the generated events is elaborated in section 4, considering characteristic features of the background processes. The results of the event selection are given in section 5. Section 6 summarizes our results and concludes this report.

2 Signal and Possible Background

The Feynman diagrams for the $e^+e^- \to t\bar{t}H$ process followed by $t(\bar{t}) \to b(\bar{b})W$ decays are shown in Figure 1. Notice that the first and second diagrams contain the top Yukawa coupling, which we want to measure. The signatures of $t\bar{t}H$ events depend on how the H and the Ws decay. In this study we concentrate on the dominant decay mode: $H \to b\bar{b}\,(68\%)$. The signal events hence have four b jets and two Ws. The $t\bar{t}H$ events can then be classified into 3 groups (8-jet, 1-lepton+6-jet, and 2-lepton+4-jet modes) corresponding to the combinations of leptonic and hadronic decays of the two Ws. For Ws that decayed leptonically we cannot reconstruct their invariant masses due to missing neutrinos. On the other hand, for the Ws that decayed hadronically we can reconstruct their masses and use them as a signature. For the t or the $\bar{t}$ with a hadronically decayed W we can also use the invariant mass of the 3-jet system to test if it is consistent with the top mass.

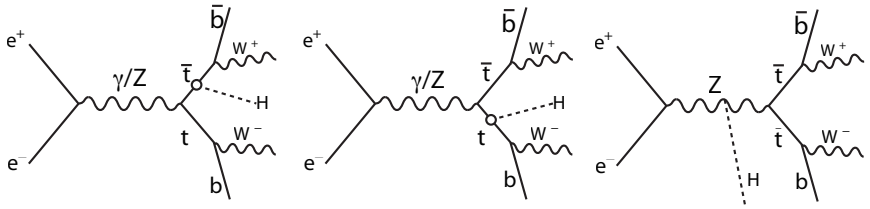

Figure 1: Feynmann diagrams for the $t\bar{t}H$ process

Possible background processes that might mimic the signatures of the $t\bar{t}H$ production include $e^+e^- \to t\bar{t}Z$, $t\bar{t}$, and $t\bar{t}g$ followed by $g \to b\bar{b}$. The cross sections for these background processes are plotted in Fig.2 together with that of the signal. Notice the smallness of the contribution from the third diagram in Fig.1, which does not contain the top Yukawa coupling. We can hence determine the top Yukawa coupling by just counting the number of signal events unless they are swamped by the background; the signal cross section is only $\sim 0.5\,\text{fb}$ with no beam polarization.

The production cross section for the $t\bar{t}Z$ background is $1.3\,\text{fb}^*$ with no beam polarization. It has four b-jets and two Ws in the final state just like the signal, if the Z boson decays into $b\bar{b}$ (15%). In this case the only difference that one can tell on an event-by-event basis lies in the invariant mass of the $b\bar{b}$ system, which should be consistent with M_H for the signal and M_Z for the background. The $t\bar{t}$ production, on the other hand, has only two b-jets in the final state. If reconstructed correctly, it could not be the background. Since the $t\bar{t}$ production cross section ($\sim 500\,\text{fb}$) is much larger than that of the signal, however, a small fraction of mis-reconstruction or failure in b-tagging may lead to significant background

*This value is with QCD threshold enhancement similar to that expected for the signal process. Without the correction the cross section is 0.7 fb.

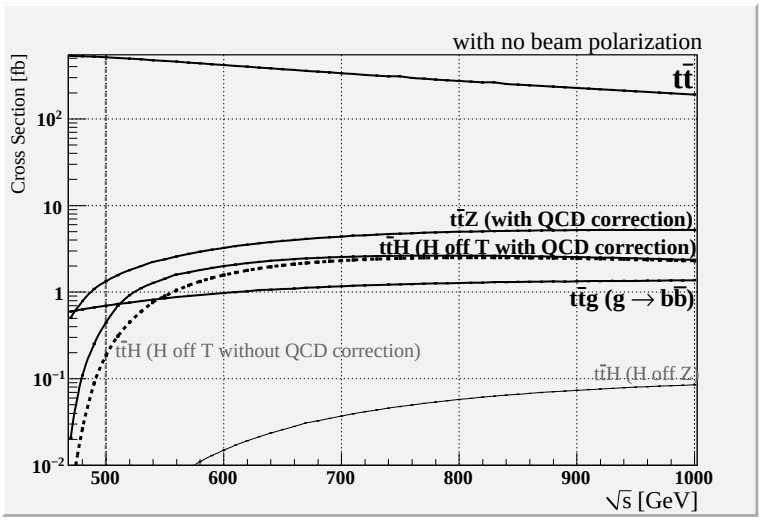

Figure 2: Production cross section of the signal, $t\bar{t}H$, together with those of the main background processes, $t\bar{t}H, t\bar{t}Z, t\bar{t}, t\bar{t}g$, as a function of the center of mass energy for no beam polarization.

contamination. The $t\bar{t}g$ production followed by $g \to b\bar{b}$ decay has the same signatures as the signal in terms of the number of b-jets and the number of Ws. As with the $t\bar{t}Z$ background the only difference is the invariant mass of the $b\bar{b}$ system. Its production cross section is also of the same order, 0.7 fb, as that of the $t\bar{t}Z$ background.

3 Analysis Framework

For Monte Carlo simulations, we generated signal and background events by using an event generator package (physsim[3]), which is based on full helicity amplitudes calculated with HELAS[4] including gauge boson decays, thereby correctly taking into account angular distributions of the decay products. The 4-momenta of the final-state quarks and leptons were passed to Pythia6.4[5] for parton showering and hadronization. The resultant particles were then swum through a detector model (see Table 1 for detector parameters) defined in our fast Monte Carlo detector simulator (QuickSim[6]). In the event generations we used $\alpha(M_Z) = 1/128$, $\sin^2\theta_W = 0.230$, $\alpha_s = 0.120$, $M_W = 80.0\,\text{GeV}$, $M_Z = 91.18\,\text{GeV}$, $M_t = 175\,\text{GeV}$, and $M_H = 120\,\text{GeV}$. We have included the initial state radiation and beamstrahlung in the event generations. The unique point of this study is the inclusion of the QCD threshold enhancement to the $t\bar{t}$ system (see Fig.3) for the signal event generation, which plays an important role especially in a low energy experiment: about a factor of 2 enhancement at $\sqrt{s} = 500\,\text{GeV}$.

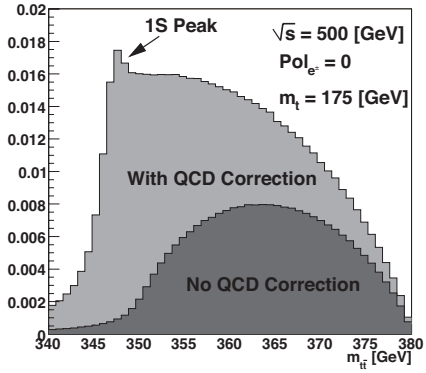

Figure 3: Invariant mass distribution for the $t\bar{t}$ sub-system.

Table 1: Detector Parameters, where p, p_T and E are measured in units of GeV

Detector	Performance	Coverage
Vertex detector	$\sigma_b = 7.0 \oplus (20.0/p)/\sin^{3/2}\theta \mu m$	$\lvert\cos\theta\rvert \leq 0.90$
Central drift chamber	$\sigma_{P_T}/P_T = 1.1 \times 10^{-4} p_T \oplus 0.1\%$	$\lvert\cos\theta\rvert \leq 0.95$
EM calorimeter	$\sigma_E/E = 15\%/\sqrt{E} \oplus 1\%$	$\lvert\cos\theta\rvert \leq 0.90$
Hadron calorimeter	$\sigma_E/E = 40\%/\sqrt{E} \oplus 2\%$	$\lvert\cos\theta\rvert \leq 0.90$

4 Event Selection

4.a Definition of our signal (1-lepton+6-jet mode on $t\bar{t}H$)

As explained in section 2 we can classify the $t\bar{t}H$ signal events into the following three decay modes according to how the two Ws from t and $\bar{t}$ decay:

1. 8-jet mode (45%)
2. 1-lepton + 6-jet mode (35%)
3. 2-lepton + 4-jet mode (7%)

where the lepton is required to be either $e^{\pm}$ or $\mu^{\pm}$ and the final-state H to decay into the dominant $b\bar{b}$ state. Notice that in all of these three modes we have four b-jets in the final states, which makes the separation of the $t\bar{t}$ background easier. In this study we concentrate on the 1-lepton + 6-jet mode as our first step because the branching ratio is not so low and the number of jets is not so high.

As shown in Figs.4 and 5 the signatures of our signal are

- an isolated energetic $e^{\pm}$ or $\mu^{\pm}$,

- six jets including four b-jets, two of which form a H boson,
- the remaining two jets being consistent with a W boson, and
- one of the two unused b-jets together with this W candidate comprising a t quark.

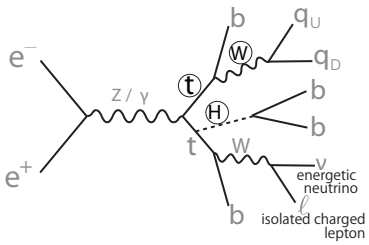

Figure 4: Schematic diagram defining our signal signatures

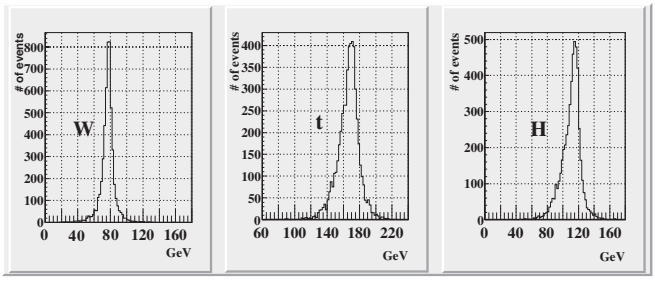

Figure 5: Invariant mass distributions for the hadronically decayed W, t, and H, which are reconstructed using generator information.

In what follows we will elaborate selection cuts designed to single out these signatures.

4.a.1 Isolated lepton search

Our event selection starts with the search for a lepton coming from a $W \to l\nu$ decay. Such a lepton from W tends to be energetic and isolated from the other tracks. In order to find such an isolated lepton, we consider a cone around each lepton track (see Fig.6) and define the cone energy to be the sum of the energies of the other tracks in the cone. Figure 7

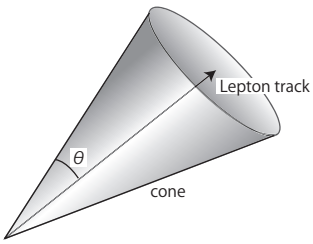

Figure 6: A cone around lepton track

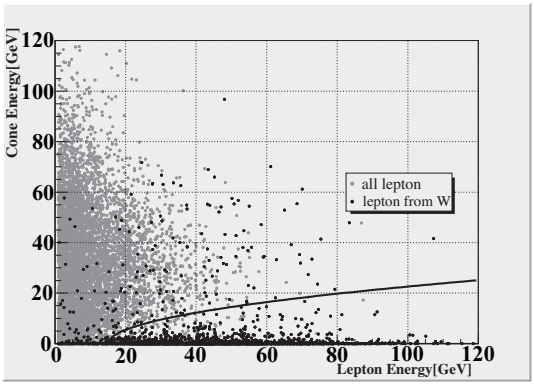

Figure 7: Cone energy distribution of isolated lepton: cut boundary $y = \sqrt{6(x-15)}$

plots the cone energy against the lepton energy. The energetic isolated leptons from Ws have to have a high lepton energy and a low cone energy, hence populating the bottom edge region (black points), while leptons from heavy flavor jets are likely to be less energetic and

have a higher cone energy (gray points). The smooth curve in the figure is our cut to select energetic isolated leptons.

4.a.2 Forced 6-Jet clustering

After finding and eliminating an energetic isolated lepton, we perform jet clustering to make six jets. For the jet clustering we use a variable Y defined by

$$Y = \frac{M_{jet}^2}{E_{visible}^2}.$$

We keep putting tracks together to form a jet while $Y < Y_{cut}$. By adjusting the Y_{cut} value, we can make arbitrary number of jets. We hence force the events to cluster into six jets by choosing an appropriate Y_{cut} value on the event-by-event basis (forced 6-jet clustering).

4.a.3 Y_{cut} cut

The Y_{cut} value for a $t\bar{t}$ background event to form six jets should be lower than the one for a signal $t\bar{t}H \to t\bar{t}b\bar{b}$ event because, after the energetic isolated lepton requirement, the $t\bar{t}$ event can hardly have more than four jets. The difference in the Y_{cut} value distributions between $t\bar{t}H(H \to b\bar{b})$ and $t\bar{t}$ is shown in Fig.8. As seen in the figure, by cutting Y_{cut} values at 0.002 we can reduce the $t\bar{t}$ background effectively.

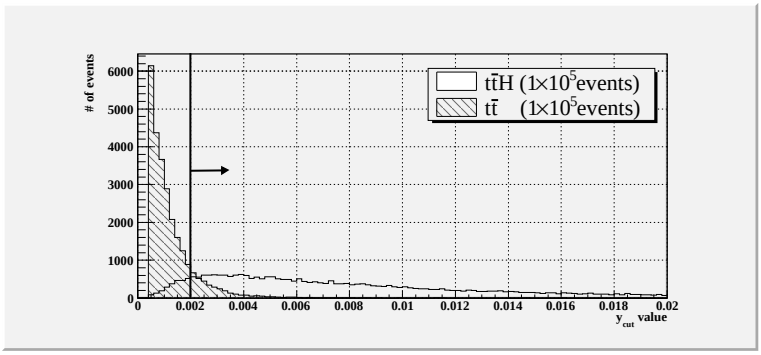

Figure 8: Ycut value distribution after isolated lepton finding

4.a.4 mass cut

After performing the jet clustering, we try to identify which jet is coming from which parent parton. We want to separate the correct combination from the other combinatorial background. Mass cut comes in handy to reduce the combinatorial background. Looping over all the 2-jet combinations we look for a pair having an invariant mass within the window of $\pm 15\,\mathrm{GeV}$ from the nominal W mass of $80.0\,\mathrm{GeV}$. From the remaining four jets we pick up one and attach it to the just found pair making a W candidate to see if the resultant 3-jet system has an invariant mass within $\pm 25\,\mathrm{GeV}$ from the nominal t mass of $175\,\mathrm{GeV}$.

If it does we search for a pair from the three jets left over that is within the mass window of $\pm 15\,\mathrm{GeV}$ from the nominal H mass of $120\,\mathrm{GeV}$. Since these mass cuts are rather loose there is a significant chance to have multiple combinations that pass them. For such a case we define a χ^2 variable with

$$\chi^2 = \left(\frac{M_{\text{2-jet}(W)} - M_W}{\sigma_{M_W}}\right)^2 + \left(\frac{M_{\text{3-jet}(t/\bar{t})} - M_t}{\sigma_{M_t}}\right)^2 + \left(\frac{M_{\text{2-jet}(H)} - M_H}{\sigma_{M_H}}\right)^2,$$

and select the combination with the smallest χ^2 value. Fig.9 shows the mass distributions for the best combinations. Although W and $t/\bar{t}$ peaks are present for both the signal and

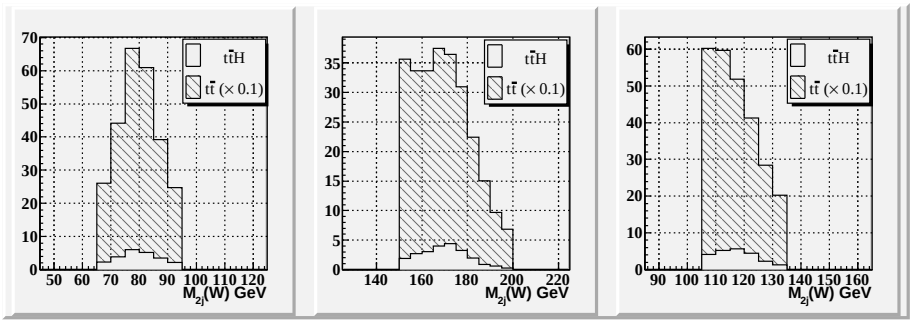

Figure 9: Invariant mass distributions after the cut on Y_{cut} values. Black open histograms are for the signal and gray histograms are for the $t\bar{t}$ background.

the $t\bar{t}$ background, a H peak is seen only for the signal process. The H peak is, however, swamped in the $t\bar{t}$ background.

4.a.5 b-tagging by the n-sig. method

For the $t\bar{t}$ background rejection, b-tagging is very powerful since the signal $t\bar{t}H(H \to b\bar{b})$ process has four b-jets, while the $t\bar{t}$ background process has only two b-jets. For b-tagging we use the so called n-sig. method descrived as follows.

Figure 10 sketches a jet from the interaction point (IP), which includes a b-hadron. The b-hadron decays at distance from the IP due to its long-life. It makes the b-jet to have some tracks which are away from the IP. When the distance (ℓ) between the IP and a track is larger than a given value ($m\sigma_\ell$), the track is defined as an off-vertex track. A jet is recognized as a b-jet if the number of such significantly off-vertex tracks exceeds a certain cut value (n). In this analysis, we define tight b-tagging with a tagging condition: $(m, n) = (3.0, 2)$ and loose b-tagging with $(m, n) = (2.0, 2)$, and require all of the four b-jet candidates have to satisfy the loose b-tagging condition and there has to be at least one tight b-tagged jet from each of the H and $t/\bar{t}$ candidates.

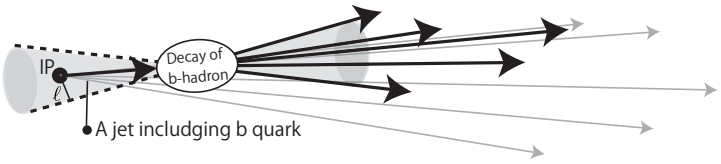

Figure 10: n-sig. method

The mass distributions after the b-tagging are shown in Fig.11. We can see that the $t\bar{t}$

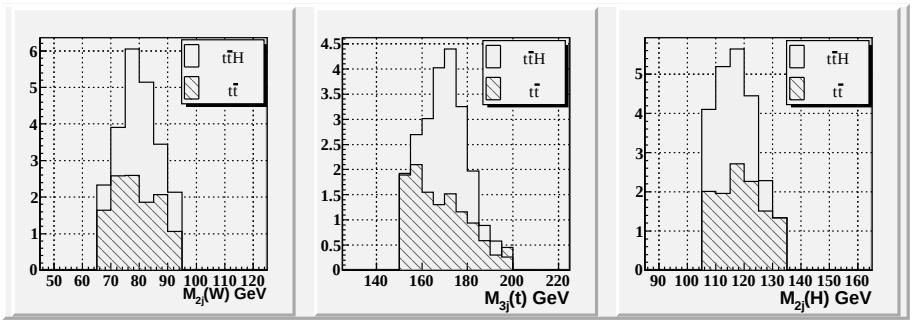

Figure 11: Invariant mass distribution after using both Y cut and b-tagging

background has been suppressed effectively. As mentioned above the $t\bar{t}Z$ and $t\bar{t}g$ $(g \to b\bar{b})$ background events have similar signatures as a signal and can be separated only with the invariant mass of the H candidate. In the next section we summarize the results of our event selection including these remaining background processes.

5 Results

In order to estimate the feasibility of measuring the top Yukawa coupling we need to specify the beam polarization and the integrated luminosity. In this study we assume an integrated luminosity of $1\,\mathrm{ab}^{-1}$. As for the beam polarization, it is worth noting that only the left-right or right-left combination contributes to the signal and background cross sections because of the γ^μ coupling of the beam particles to the vector bosons (γ/Z) in the intermediate states. It is hence sufficient to know the cross sections for the beam polarization combinations: $(e^-, e^+) = (-1, +1), (+1, -1)$. Table2 shows these cross sections.

For both of the beam polarization combinations: $(-1, +1)$ and $(+1, -1)$, we have generated 50k events each for the $t\bar{t}H$, $t\bar{t}Z$, and $t\bar{t}g\,(g \to b\bar{b})$ processes, and 5M events for the $t\bar{t}$ background. We performed the event selection described in the previous section and tabulated the results normalized to an integrated luminosity $1\,\mathrm{ab}^{-1}$ in Table 3 assuming the cross section shown in Table 2.

The corresponding distributions for the reconstructed W, $t/\bar{t}$, and H candidates are shown in Fig.12 for the beam polarization combination: $(-0.8, +0.3)$. We can see a clear

Table 2: Cross sections at $\sqrt{s} = 500\,\mathrm{GeV}$. $t\bar{t}H$ and $t\bar{t}Z$ are with QCD threshold enhancement. (-1,+1)/(+1,-1) corresponds to $(e_L^-, e_R^+)/(e_R^-, e_L^+)$, respectively.

Beam Polarization	(-1,+1)	(+1,-1)
$t\bar{t}H$	1.24 [fb]	0.540 [fb]
$t\bar{t}Z$	2.18 [fb]	0.712 [fb]
$t\bar{t}$	720. [fb]	309. [fb]
$t\bar{t}g$ $(g \to b\bar{b})$	1.93 [fb]	0.859 [fb]

Table 3: Cut Statistics (normalized to $1\,\mathrm{ab}^{-1}$)

Beam Polarization	(0.0,0.0)				(-0.8,+0.3)			
Processes	$t\bar{t}H$	$t\bar{t}Z$	$t\bar{t}$	$t\bar{t}g$ $(b\bar{b})$	$t\bar{t}H$	$t\bar{t}Z$	$t\bar{t}$	$t\bar{t}g$ $(b\bar{b})$
No Cut	449.0	1340.0	514040.5	697.5	759.0	2407	863500.4	1159.6
$N_{iso.lep}$=1	159.4	435.9	209718.4	242.2	269.4	783.0	303879.0	397.7
Y_{cut} (6 jets) > 0.002	139.2	307.8	22851.3	152.5	235.4	552.9	38477.2	249.6
btag & mass cut	23.0	12.2	11.9	6.9	38.9	21.8	19.7	11.3

evidence of signal events over the background in each of the three mass distributions.

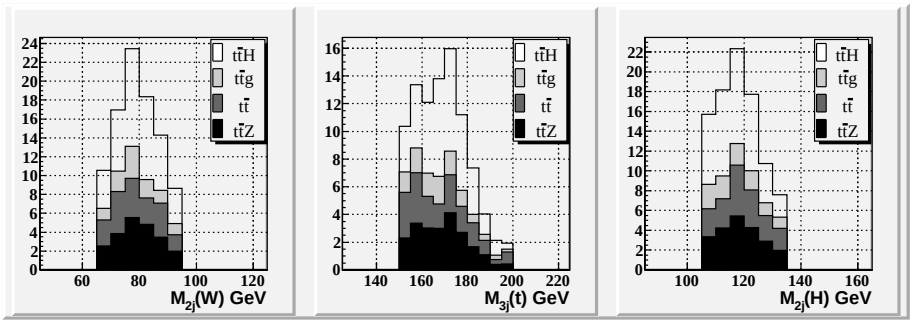

Figure 12: Mass distributions (cumulative) for the final selected sample for the beam polarization combination: $(-0.8, +0.3)$.

In the case of no beam polarization 23.0 signal events are left with 31.0 background events total. On the other hand we have 38.9 signal events with 52.8 background events total at the end of the event selection. The signal significance is $4.1\,\sigma$ for the polarization combination: $(0, 0)$ and $5.4\,\sigma$ for the polarization combination: $(-0.8, +0.3)$. Since the number of the signal events is proportional to the square of the top Yukawa coupling (g_Y), we can easily translate these numbers to its expected precisions: $\Delta g_Y/g_Y = \pm 0.12$ and ± 0.093 for the beam polarization polarization combinations: $(0, 0)$ and $(-0.8, +0.3)$, respectively.

6 Summary and Conclusion

We have performed a feasibility study of measuring the top Yukawa coupling at $\sqrt{s} = 500\,\mathrm{GeV}$, taking advantage of the QCD threshold enhancement to the $t\bar{t}$ sub-system. For this study we have implemented the threshold enhancement in the $t\bar{t}H$ and $t\bar{t}Z$ event generators in the physsim package. It is found that for an integrated luminosity of $1\,\mathrm{ab}^{-1}$ we can observe the $t\bar{t}H$ process with a significance of $4.1\,\sigma$ without beam polarization, and $5.4\,\sigma$ with the beam polarization combination: $(e^-, e^+) = (-0.8, +0.3)$. These numbers show that we can measure the top Yukawa coupling to an accuracy of about 10% at $\sqrt{s} = 500\,\mathrm{GeV}$, which is the energy already available in the first stage of the ILC.

7 Acknowledgments

The authors would like to thank all the members of the ILC physics subgroup [16] for useful discussions. Among them, A. Ishikawa, Y. Sumino, and Y. Kiyo deserve special mention for their contributions to the implementation of the QCD threshold correction. They are also grateful to T. Tanabe for providing us with the $t\bar{t}g\,(g \to b\bar{b})$ generator. This study is supported in part by the Creative Scientific Research Grant No. 18GS0202 of the Japan Society for Promotion of Science and the JSPS Core University Program.

References

[1] A. Gay, *Eur. Phys. J.* **C49**, p489 (2007)

[2] C. Farrell and A. H. Hoang, *Phys. Rev.* **D72**, 014007 (2005), C. Farrell and A. H. Hoang, *Phys. Rev.* **D74**, 014008 (2006).

[3] physsim-2007a, http://www-jlc.kek.jp/subg/offl/physsim/.

[4] H. Murayama, I. Watanabe, and K. Hagiwara, KEK Report No. 91-11 (1992).

[5] T. Sjöstrand, L. Lönnblad, S. Mrenna, and P. Skands, arXiv:hep-ph/0308153.

[6] JSF Quick Simulator, http://www-jlc.kek.jp/subg/offl/jsf/.

[7] http://www-jlc.kek.jp/subg/physics/ilcphys/.

Higgs boson pair production at the Photon Linear Collider in the two Higgs doublet model

Daisuke Harada[(a),(b)], **Eri Asakawa**[(c)], **Shinya Kanemura**[(d)], **Yasuhiro Okada**[(a),(b)], and **Koji Tsumura**[(e)]

[(a)] *KEK Theory Center, Institute of Particle and Nuclear Studies, KEK 1-1 Oho, Tsukuba, Ibaraki 305-0801, Japan*
[(b)] *Department of Particle and Nuclear Physics, the Graduate University for Advanced Studies (Sokendai) 1-1 Oho, Tsukuba, Ibaraki 305-0801, Japan*
[(c)] *Institute of Physics, Meiji Gakuin University Yokohama 244-8539, Japan*
[(d)] *Department of Physics, University of Toyama 3190 Gofuku, Toyama 930-8555, Japan*
[(e)] *International Centre for Theoretical Physics, Strada Costiera 11, 34014 Trieste, Italy*

We calculate the cross section of the lightest Higgs boson pair production at the Photon Linear Collider in the two Higgs doublet model. We focus on the scenario in which the lightest Higgs boson has the standard model like couplings to gauge bosons. We take into account the one-loop correction to the *hhh* coupling as well as additional one-loop diagrams due to charged bosons to the $\gamma\gamma \to hh$ helicity amplitudes. We discuss the impact of these corrections on the *hhh* coupling measurement at the Photon Linear Collider.

.

1 Introduction

The Higgs sector is the last unknown part of the standard model (SM). In the SM, the tree level Higgs self-coupling $\lambda_{hhh} = 3m_h^2/v$ and $\lambda_{hhhh} = 3m_h^2/v^2$ are uniquely determined by the Higgs boson mass m_h, where v is vacuum expectation value (VEV) of the Higgs boson. The effective Higgs potential is written as

$$V = \frac{1}{2}m_h^2 h^2 + \frac{1}{3!}\tilde{\lambda}_{hhh}h^3 + \frac{1}{4!}\tilde{\lambda}_{hhhh}h^4 + \cdots , \tag{1.12}$$

where the effective Higgs self-couplings $\tilde{\lambda}_{hhh}$ and $\tilde{\lambda}_{hhhh}$ are given by precision measurement of *hhh* and *hhhh* couplings. If the deviation from the SM tree level Higgs self-coupling (λ_{hhh} and λ_{hhhh}) is found, it can be regarded as an evidence of new physics beyond the SM. The origin of the spontaneous electroweak symmetry breaking (EWSB) would be experimentally tested after the discovery of a new scalar particle by measuring its mass and self-couplings. The Higgs self-coupling measurement is one of main purposes at the International Linear Collider (ILC). The structure of the Higgs potential depends on the scenario of new physics beyond the SM, so that precision measurement of the *hhh* coupling can be a probe of each new physics scenario[1, 2].

It is known that the measurement of the triple Higgs boson coupling is rather challenging at the CERN Large Hadron Collider (LHC). At the SLHC with luminosity of 3000 fb^{-1},

the hhh coupling can be determined with an accuracy of 20-30% for 160 GeV $\leq m_h \leq$ 180 GeV[3, 4]. At the ILC, the main processes for the hhh measurement are the double Higgs boson production mechanisms via the Higgs-strahlung and the W-boson fusion[5, 6]. At the ILC with a center of mass energy of 500 GeV, the double Higgs strahlung process $e^+e^- \to Zhh$ is dominant. On the other hand, W-boson fusion process $e^+e^- \to hh\nu\bar{\nu}$ becomes dominant due to its t-channel nature at 1 TeV or higher energies[7]. Sensitivity to the hhh coupling in these processes becomes rapidly worse for greater Higgs boson masses. In particular, for the intermediate mass range (140 GeV $\leq m_h \leq$ 200 GeV), it has not yet been known how accurately the hhh coupling can be measured by the electron-positron collision. The Photon Linear Collider (PLC) is an optional experiment of the ILC. The possibility of measuring the hhh coupling via the process of $\gamma\gamma \to hh$ has been discussed in Ref. [8]. In Ref. [9] the statistical sensitivity to the hhh coupling constant has been studied especially for a light Higgs boson mass in relatively low energy collisions.

In this paper, we study the double Higgs production process at the PLC. In Sect. 2, we discuss the statistical sensitivity to the hhh coupling constant via the process of $e^-e^- \to \gamma\gamma \to hh$ at the PLC in the SM. In Sect. 3, we study the new particle effects on the $\gamma\gamma \to hh$ process in the two Higgs doublet model (THDM).

2 The statistical sensitivity to the hhh coupling constant

We study the statistical sensitivity to the hhh coupling constant for wide regions of the Higgs boson masses and the collider energies at the PLC. The $\gamma\gamma \to hh$ process is an one-loop induced process. The Feynman diagrams for this process in the SM are given in Ref. [8]. There are two types of diagrams, which are the pole diagrams and the box diagrams. The amplitude of the pole diagrams describes as $\mathcal{M}_{\rm pole} \propto \tilde{\lambda}_{hhh}/s$, where $\sqrt{s}$ is the center of mass energy of the $\gamma\gamma$ system. It is suppressed by $1/s$ at the high energy region, so that the statistical sensitivity to the hhh coupling becomes rapidly worse for this region. On the other hand, the box diagrams do not depend on the hhh coupling.

In Fig. 1, we present the statistical sensitivity on the Higgs self-coupling constant at the PLC. We modify the triple Higgs coupling constant as $\tilde{\lambda}_{hhh} = \lambda_{hhh}(1 + \delta\kappa)$, where $\delta\kappa$ represents deviation from the SM prediction. We assume that the efficiency of the particle tagging is 100% with an integrated luminosity of 1/3 ab^{-1} and E_{ee} is the center of mass energy of the e^-e^- system. We plot $\delta\kappa$ based on statistical error of the event number in the $e^-e^- \to \gamma\gamma \to hh$ process in the SM. Namely, $\delta\kappa$ is determined by

$$|N(\delta\kappa) - N(\delta\kappa = 0)| = \sqrt{N(\delta\kappa = 0)}, \tag{2.13}$$

for assumed luminosity. Notice that $\delta\kappa$ is not symmetric with respect to $\delta\kappa = 0$ because there is interference between pole and box diagrams. The cases for $\delta\kappa > 0$ and $\delta\kappa < 0$ are shown separetly. The left [right] figure shows the sensitivity as a function of m_h [E_{ee}]. It is found that when the collision energy is limited to be lower than 500-600 GeV the statistical sensitivity to the hhh coupling can be better for the process in the $\gamma\gamma$ collision than that in the electron-positron collision for the Higgs boson with the mass of 160 GeV[10].

3 The $\gamma\gamma \to hh$ process in the THDM

We consider the new particle effects on the $\gamma\gamma \to hh$ process in the THDM, in which additional CP-even, CP-odd and charged Higgs boson appear. It is known that non-decoupling

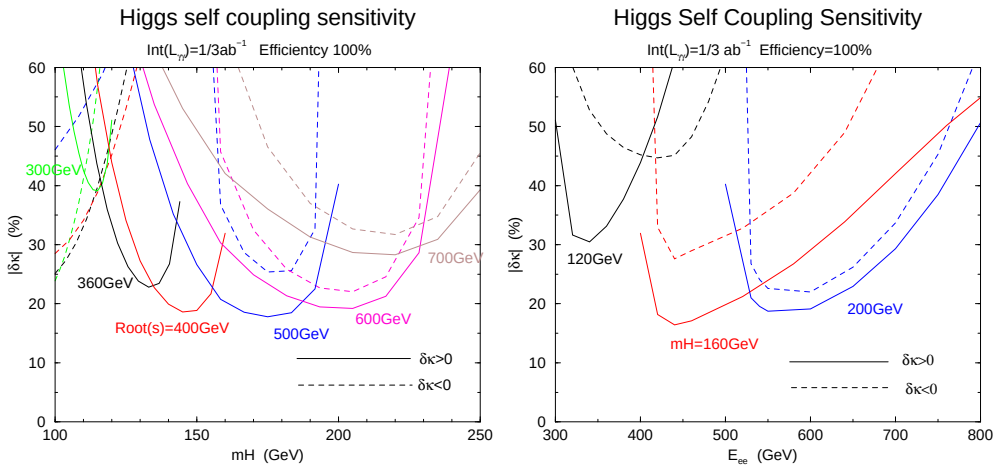

Figure 1: The statistical sensitivity to the hhh coupling constant at the PLC. In the left [right] figure, the statistical sensitivity is shown as a function of m_h [E_{ee}] for each value of E_{ee} [m_h]. Solid [Dotted] lines correspond to $\delta\kappa > 0$ [$\delta\kappa < 0$] case.

loop effect of extra Higgs bosons shift the hhh coupling value from the SM by $\mathcal{O}(100)\%$[1]. In the $\gamma\gamma \to hh$ helicity amplitudes, there are additional one-loop diagrams by the charged Higgs boson loop to the ordinary SM diagrams (the W-boson loop and the top quark loop). It is found that both the charged Higgs boson loop contribution to the $\gamma\gamma \to hh$ amplitudes and the non-decoupling effect on the hhh coupling can enhance the cross section from its SM value significantly[11].

In order to study the new physics effect on $\gamma\gamma \to hh$ process, we calculate the helicity amplitudes in the THDM. The THDM Higgs potential is given by

$$\begin{aligned} V_{\rm THDM} &= \mu_1^2|\Phi_1|^2 + \mu_2^2|\Phi_2|^2 - (\mu_3^2\Phi_1^\dagger\Phi_2 + \text{h.c.}) \\ &\quad +\lambda_1|\Phi_1|^4 + \lambda_2|\Phi_2|^4 + \lambda_3|\Phi_1|^2|\Phi_2|^2 + \lambda_4|\Phi_1^\dagger\Phi_2|^2 + \frac{\lambda_5}{2}\left\{(\Phi_1^\dagger\Phi_2)^2 + \text{h.c.}\right\}, \end{aligned} \tag{3.14}$$

where Φ_1 and Φ_2 are two Higgs doublets with hypercharge $+1/2$. The Higgs doublets are parametrized as

$$\Phi_i = \begin{bmatrix} \omega_i^+ \\ \frac{1}{\sqrt{2}}(v_i + h_i + iz_i) \end{bmatrix}, \quad (i = 1, 2), \tag{3.15}$$

where VEVs v_1 and v_2 satisfy $v_1^2 + v_2^2 = v^2 \simeq (246\ \text{GeV})^2$. The mass matrices can be diagonalized by introducing the mixing angles α and β, where α diagonalizes the mass matrix of the CP-even neutral bosons, and $\tan\beta = v_2/v_1$. Consequently, we have two CP-even (h and H), a CP-odd (A) and a pair of charged ($H^\pm$) bosons. We define α such that h is the SM-like Higgs boson when $\sin(\beta - \alpha) = 1$.

We concentrate on the case with so called the SM-like limit [$\sin(\beta - \alpha) = 1$], where the lightest Higgs boson h has the same tree-level couplings as the SM Higgs boson, and the

other bosons do not couple to gauge bosons and behave just as extra scalar bosons. In this limit, the masses of Higgs bosons are

$$m_h^2 = \{\lambda_1 \cos^4\beta + \lambda_2 \sin^4\beta + 2(\lambda_3+\lambda_4+\lambda_5)\cos^2\beta\sin^2\beta\}v^2, \quad (3.16)$$

$$m_H^2 = M^2 + \frac{1}{8}\{\lambda_1+\lambda_2-2(\lambda_3+\lambda_4+\lambda_5)\}(1-\cos 4\beta)v^2, \quad (3.17)$$

$$m_A^2 = M^2 - \lambda_5 v^2, \quad (3.18)$$

$$m_{H^\pm}^2 = M^2 - \frac{\lambda_4+\lambda_5}{2}v^2, \quad (3.19)$$

where $M(=|\mu_3|/\sqrt{\sin\beta\cos\beta})$ represents the soft breaking scale for the discrete symmetry, and determines the decoupling property of the extra Higgs bosons. When $M \sim 0$, the extra Higgs bosons H, A and $H^\pm$ receive their masses from the VEV, so that the masses are proportional to λ_i. Large masses cause significant non-decoupling effect in the radiative correction to the hhh coupling. On the other hand, when $M \gg v$ the masses are determined by M. In this case, the quantum effect decouples for $M \to \infty$.

It is known that in the THDM λ_{hhh} can be changed from the SM prediction by the one-loop contribution of extra Higgs bosons due to the non-decoupling effect (when $M \sim 0$). In the following analysis, we include such an effect on the cross sections. The effective hhh coupling $\Gamma_{hhh}^{\rm THDM}(\hat{s}, m_h^2, m_h^2)$ is evaluated at the one-loop level as[1]

$$\Gamma_{hhh}^{\rm THDM}(\hat{s}, m_h^2, m_h^2) \simeq \frac{3m_h^2}{v}\left[1 + \sum_{\Phi=H,A,H^+,H^-}\frac{m_\Phi^4}{12\pi^2v^2m_h^2}\left(1-\frac{M^2}{m_\Phi^2}\right)^3 - \frac{N_c m_t^4}{3\pi^2v^2m_h^2}\right]. \quad (3.20)$$

The exact one-loop formula for $\Gamma_{hhh}^{\rm THDM}$ is given in Ref. [2], which has been used in our actual numerical analysis.

In Fig. 2, we plot the cross sections of $\gamma\gamma \to hh$ for the helicity set $(+,+)$ as a function of the photon-photon collision energy $E_{\gamma\gamma}$. The five curves correspond to the following cases,

(a) THDM 2-loop: the cross section in the THDM with additional one-loop corrections to the hhh vertex, $\Gamma_{hhh}^{\rm THDM}$.

(b) THDM 1-loop: the cross section in the THDM with the tree level hhh coupling constant λ_{hhh}.

(c) SM 2-loop: the cross section in the SM with additional top loop correction to the hhh coupling $\Gamma_{hhh}^{\rm SM}$ given in Ref. [2].

(d) SM 1-loop: the cross section in the SM with the tree level hhh coupling constant $\lambda_{hhh}^{\rm SM}$ $(= \lambda_{hhh}$ for $\sin(\beta-\alpha)=1)$.

(e) For comparison, we also show the result which corresponds to the SM 1-loop result with the effective hhh coupling $\Gamma_{hhh}^{\rm THDM}$.

In the left figure, there are three peaks in the case (a) (THDM 2-loop). The one at the lowest $E_{\gamma\gamma}$ is the peak just above the threshold of hh production. There the cross section is by about factor three enhanced as compared to the SM prediction due to the effect of $\Delta\Gamma_{hhh}^{\rm THDM}/\Gamma_{hhh}^{\rm SM}$ $(\sim 120\%)$ because of the dominance of the pole diagrams in $\gamma\gamma \to hh$. The

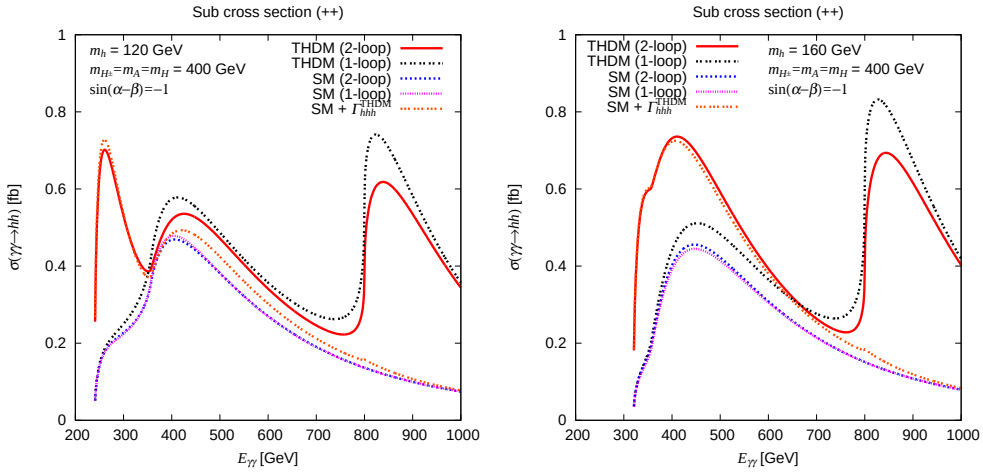

Figure 2: The cross section $\hat{\sigma}(+,+)$ for the sub process $\gamma\gamma \to hh$ with the photon helicity set $(+,+)$ as a function of the collision energy $E_{\gamma\gamma}$. In the left [right] figure the parameters are taken to be $m_h = 120$ [160] GeV for $m_\Phi (\equiv m_H = m_A = m_{H^\pm}) = 400$ GeV, $\sin(\beta - \alpha) = 1$, $\tan\beta = 1$ and $M = 0$.

second peak at around $E_{\gamma\gamma} \sim 400$ GeV comes from the top quark loop contribution which is enhanced by the threshold of top pair production. Around this point, the case (a) can be described by the case (e) (SM+$\Gamma_{hhh}^{\rm THDM}$). For $E_{\gamma\gamma} \sim$ 400-600 GeV, the cross section in the case (a) deviates from the case (c) (SM 2-loop) due to both the charged Higgs loop effect and the effect of $\Delta\Gamma_{hhh}^{\rm THDM}/\Gamma_{hhh}^{\rm SM}$. The third peak at around $E_{\gamma\gamma} \sim 850$ GeV is the threshold enhancement of the charged Higgs boson loop effect, where the real production of charged Higgs bosons occurs. The contribution from the non-pole one-loop diagrams are dominant. In the right figure, we can see two peaks around $E_{\gamma\gamma} \sim$ 350-400 GeV and 850 GeV. At the first peak, the contribution from the pole diagrams is dominant so that the cross section is largely enhanced by the effect of $\Delta\Gamma_{hhh}^{\rm THDM}/\Gamma_{hhh}^{\rm SM}$ by several times 100% for $E_{\gamma\gamma} \sim 350$ GeV. It also amounts to about 80% for $E_{\gamma\gamma} \sim 400$ GeV. For $E_{\gamma\gamma} <$ 600-700 GeV, the result in the case (e) gives a good description of that in the case (a). The second peak is due to the threshold effect of the real H^+H^- production as in the left figure.

In Fig. 3, the full cross section of $e^-e^- \to \gamma\gamma \to hh$ is given from the sub cross sections by convoluting the photon luminosity spectrum[8]. In our study, we set $x = 4E_b\omega_0/m_e^2 = 4.8$ where E_b is the energy of electron beam, ω_0 is the laser photon energy and m_e is the electron mass. In order to extract the contribution from $\hat{\sigma}(+,+)$ that is sensitive to the hhh vertex, we take the polarizations of the initial laser beam to be both -1, and those for the initial electrons to be both $+0.45$. The full cross section for $m_\Phi = 400$ GeV has similar energy dependences to the sub cross section $\hat{\sigma}(+,+)$ in Fig. 2, where corresponding energies are rescaled approximately by around $\sqrt{s} \sim E_{\gamma\gamma}/0.8$ due to the photon luminosity spectrum. For smaller m_Φ, the peak around $\sqrt{s} \sim 350$ GeV becomes lower because of smaller $\Delta\Gamma_{hhh}^{\rm THDM}/\Gamma_{hhh}^{\rm SM}$.

In Fig. 4, five curves correspond to the cases (a) to (e) in Fig. 2. In the left figure, one

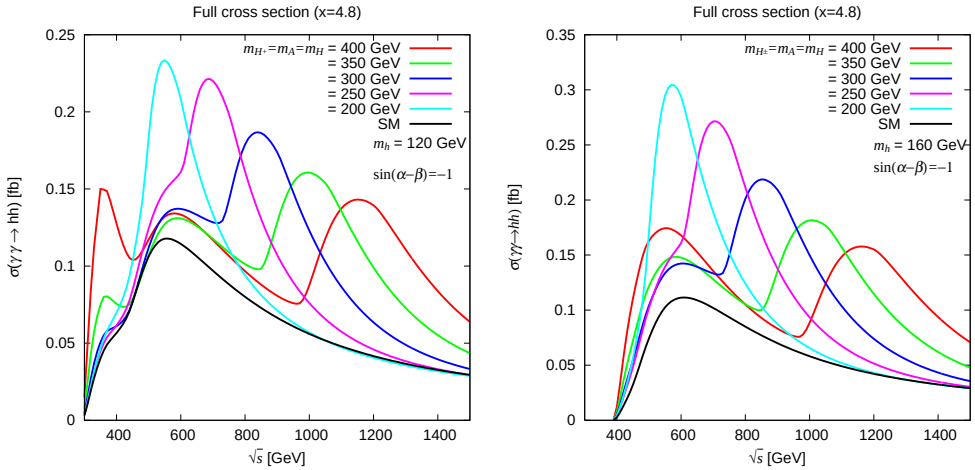

Figure 3: The full cross section of $e^-e^- \to \gamma\gamma \to hh$ as a function of $\sqrt{s}$ for each value of $m_\Phi (= m_H = m_A = m_{H^\pm})$ with $\sin(\beta-\alpha) = 1$, $\tan\beta = 1$ and $M = 0$. The case for $m_h = 120$ [160] GeV is shown in the left [right] figure.

can see that the cross section is enhanced due to the enlarged $\Gamma^{\rm THDM}_{hhh}$ for larger values of m_Φ which is proportional to m_Φ^4 (when $M \sim 0$). This implies that the cross section for these parameters is essentially determined by the pole diagram contributions. The effect of the charged Higgs boson loop is relatively small since the threshold of charged Higgs boson production is far. Therefore, the deviation in the cross section from the SM value is smaller for relatively small m_Φ (10-20% for $m_\Phi < 300$ GeV due to the charged Higgs loop effect) but it becomes rapidly enhanced for greater values of m_Φ ($\mathcal{O}(100)$ % for $m_\Phi > 350$ GeV due to the large $\Delta\Gamma^{\rm THDM}_{hhh}$). A similar enhancement for the large m_Φ values can be seen in the right figure. The enhancement in the cross section in the THDM can also be seen for $m_\Phi < 250$ GeV, where the threshold effect of the charged Higgs boson loop appears around $\sqrt{s} \sim 600$ GeV in addition to that of the top quark loop diagrams. For $m_\Phi = 250$-400 GeV, both contributions from the charged Higgs boson loop contribution and the effective hhh coupling are important and enhance the cross section from its SM value by 40-50%.

4 Conclusions

In this paper, we have analysed the new physics loop effects on the cross section of $\gamma\gamma \to hh$ in the THDM with SM-like limit including the next to leading effect due to the extra Higgs boson loop diagram in the hhh vertex. Our analysis shows that the cross section can be largely changed from the SM prediction by the two kinds of contributions; i.e., additonal contribution by the charged Higgs boson loop effect, and the effective one-loop hhh vertex $\Gamma^{\rm THDM}_{hhh}$ enhanced by the non-decoupling effect of extra Higgs bosons. The cross section strongly depends on m_h and $\sqrt{s}$ and also on m_Φ. The approximation of the full cross section in the case (a) (THDM 2-loop) by using the result in the case (e) (SM+$\Gamma^{\rm THDM}_{hhh}$) is a good description for $\sqrt{s} \ll 2m_\Phi/0.8$. On the other hand, in a wide region between

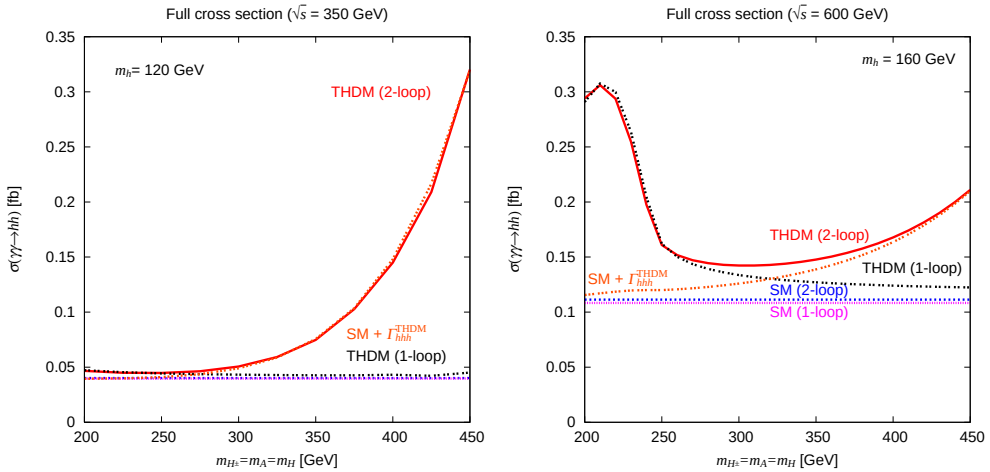

Figure 4: In the left [right] figure, the full cross section of $e^-e^- \to \gamma\gamma \to hh$ at $\sqrt{s} = 350$ GeV [600 GeV] for $m_h = 120$ [160] GeV is shown as a function of $m_\Phi (= m_H = m_A = m_{H^\pm})$ with $\sin(\beta - \alpha) = 1$, $\tan\beta = 1$ and $M = 0$.

threshold of top pair production and that of charged Higgs boson pair production, both the contributions (those from charged Higgs boson loop effect and from $\Gamma^{\rm THDM}_{hhh}$) are important. In the region below the threshold of the real production of extra Higgs bosons, cross section is largely enhanced from the SM value by the effects of the charged Higgs boson loop and the effective $\Gamma^{\rm THDM}_{hhh}$ coupling. These New Physics effects would be detectable at the future Photon Linear Collider.

5 Acknowledgments

The authors would like to thank all the members of the ILC physics subgroup [16] for useful discussions. This study is supported in part by the Creative Scientific Research Grant No. 18GS0202 of the Japan Society for Promotion of Science. The work of S. K. was supported in part by Grant-in-Aid for Science Research, Japan Society for the Promotion of Science (JSPS), No. 18034004. The work of Y. O. was supported in part by Grant-in-Aid for Science Research, MEXT-Japan, No. 16081211, and JSPS, No. 20244037.

References

[1] S. Kanemura, S. Kiyoura, Y. Okada, E. Senaha and C. P. Yuan, Phys. Lett. B **558**, 157 (2003) [arXiv:hep-ph/0211308].

[2] S. Kanemura, Y. Okada, E. Senaha and C. P. Yuan, Phys. Rev. D **70**, 115002 (2004) [arXiv:hep-ph/0408364].

[3] U. Baur, T. Plehn and D. L. Rainwater, Phys. Rev. Lett. **89**, 151801 (2002) [arXiv:hep-ph/0206024]; U. Baur, T. Plehn and D. L. Rainwater, Phys. Rev. D **67**, 033003 (2003) [arXiv:hep-ph/0211224].

[4] U. Baur, T. Plehn and D. L. Rainwater, Phys. Rev. D **68**, 033001 (2003) [arXiv:hep-ph/0304015].

[5] G. J. Gounaris, D. Schildknecht and F. M. Renard, Phys. Lett. B **83**, 191 (1979); V. D. Barger, K. m. Cheung, A. Djouadi, B. A. Kniehl and P. M. Zerwas, Phys. Rev. D **49**, 79 (1994) [arXiv:hep-ph/9306270]; A. Djouadi, H. E. Haber and P. M. Zerwas, Phys. Lett. B **375**, 203 (1996) [arXiv:hep-ph/9602234]; V. A. Ilyin, A. E. Pukhov, Y. Kurihara, Y. Shimizu and T. Kaneko, Phys. Rev. D **54**, 6717 (1996) [arXiv:hep-ph/9506326].

[6] W. Kilian, M. Kramer and P. M. Zerwas, Phys. Lett. B **373**, 135 (1996) [arXiv:hep-ph/9512355]; J. i. Kamoshita, Y. Okada, M. Tanaka and I. Watanabe, arXiv:hep-ph/9602224; A. Djouadi, W. Kilian, M. Muhlleitner and P. M. Zerwas, Eur. Phys. J. C **10**, 45 (1999) [arXiv:hep-ph/9904287]; C. Castanier, P. Gay, P. Lutz and J. Orloff, arXiv:hep-ex/0101028; G. Belanger *et al.*, Phys. Lett. B **576**, 152 (2003) [arXiv:hep-ph/0309010].

[7] M. Battaglia, E. Boos and W. M. Yao, [arXiv:hep-ph/0111276]; Y. Yasui, S. Kanemura, S. Kiyoura, K. Odagiri, Y. Okada, E. Senaha and S. Yamashita, arXiv:hep-ph/0211047; Talk given by S. Yamashita at LCWS2004 (`http://polywww.in2p3.fr/actualites/congres/lcws2004/`).

[8] G. V. Jikia, Nucl. Phys. B **412**, 57 (1994).

[9] R. Belusevic and G. Jikia, Phys. Rev. D **70**, 073017 (2004) [arXiv:hep-ph/0403303].

[10] E. Asakawa, D. Harada, S. Kanemura, Y. Okada and K. Tsumura, arXiv:0902.2458 [hep-ph]; Talk given by E. Asakawa at LEI 2007 (`http://home.hiroshima-u.ac.jp/lei2007/index.html`), talk given by S. Kanemura at TILC 08 (`http://www.awa.tohoku.ac.jp/TILC08/`), and talk given by D. Harada at LCWS 08 (`http://www.linearcollider.org/lcws08/`).

[11] E. Asakawa, D. Harada, S. Kanemura, Y. Okada and K. Tsumura, Phys. Lett. B **672**, 354 (2009) [arXiv:0809.0094 [hep-ph]].

[12] http://www-jlc.kek.jp/subg/physics/ilcphys/.

Measuring Higgs boson associated Lepton Flavour Violation in electron-photon collisions at the ILC *

Shinya Kanemura[(a)], and **Koji Tsumura**[(b)]

[(a)] *Department of Physics, University of Toyama, 3190 Gofuku, Toyama 930-8555, Japan*
[(b)] *The Abdus Salam ICTP of UNESCO and IAEA, Strada Costiera 11, 34151 Trieste, Italy*

We study the LFV Higgs production processes $e^-\gamma \to \ell^-\varphi$ ($\ell = \mu, \tau; \varphi = H, A$) as a probe of Higgs mediated LFV couplings at an electron-photon collider, where H and A are extra CP even and odd Higgs bosons, respectively, in the two Higgs doublet model. Under the constraints from the current data of muon and tau rare decay, the cross section can be significantly large. It would improve the experimental upper bounds on the effective LFV coupling constants. In addition, the chirality nature of the LFV Higgs coupling constants can be measured by selecting electron beam polarizations.

1 Introduction

Lepton Flavour Violation (LFV) is clear evidence of new physics beyond the standard model (SM). It can be naturally induced in various new physics scenarios such as supersymmetric extensions of the SM. The origin of LFV would be related to the structure of the fundamental theory at high energies. Therefore, new physics models can be explored by measuring the LFV processes. In the minimal supersymmetric SM with heavy right-handed neutrinos (MSSMRN), the LFV Yukawa interactions can be radiatively generated via the slepton mixing [2, 3]. The slepton mixing can be induced by the running effect from the neutrino Yukawa interaction even when flavour blind structure is realized at the grand unification scale [2].

The experimental bound on the effective LFV Yukawa couplings have been studied extensively [4, 5, 6]. These constraints will be improved at PSI MEG [7] and J-PARC COMET [8] experiments via muon rare decays, and at CERN LHCb [9] and KEK super-B factory [10] via tau rare decays. In addition, collider signatures of the LFV phenomena have also been investigated at the CERN Large Hadron Collider (LHC) [11], the International Linear Collider (ILC) [12], and the Neutrino Factory [13]. These collider experiments would be useful to test the Higgs-boson-associated LFV couplings [14, 15, 6, 16].

In this report, we discuss the physics potential of the LFV Higgs boson production process $e^-\gamma \to \ell^-\varphi$ ($\ell = \mu, \tau; \varphi = h, H, A$) where h, H and A are neutral Higgs bosons. It can be an useful tool for measuring Higgs-boson-mediated LFV parameters in two Higgs doublet models (THDMs) including Minimal Supersymmetric SMs (MSSMs). The total cross sections for these processes can be large for allowed values of the LFV couplings under the constraint from the current experimental data. Measuring these processes, the bounds for the Higgs boson associated LFV coupling constants can be improved significantly.

*This proceeding paper is based on Ref [1].

Furthermore, the chirality of these couplings can be measured by using the polarized initial electron beam.

2 Higgs boson associated LFV coupling constants

The effective Yukawa interaction for charged leptons is given in the general framework of the THDM by [5, 6]

$$\mathcal{L}_{\rm lepton} = -\overline{\ell_{Ri}}\left\{Y_{\ell_i}\delta_{ij}\Phi_1 + \left(Y_{\ell_i}\epsilon^L_{ij} + \epsilon^R_{ij}Y_{\ell_j}\right)\Phi_2\right\}\cdot L_j + \text{H.c.}, \tag{2.21}$$

where $\ell_{Ri}(i = 1\text{–}3)$ represent isospin singlet fields of right-handed charged leptons, L_i are isospin doublets of left-handed leptons, Y_{ℓ_i} are the Yukawa coupling constants of ℓ_i, and Φ_1 and Φ_2 are the scalar iso-doublets with hypercharge $Y = 1/2$. Parameters $\epsilon^X_{ij}(X = L, R)$ can induce LFV interactions in the charged lepton sector in the basis of the mass eigenstates. In Model II THDM [17], ϵ^X_{ij} vanishes at the tree level, but it can be generated radiatively by new physics effects [3]. The effective Lagrangian can be rewritten in terms of physical Higgs boson fields. Assuming the CP invariant Higgs sector, there are two CP even Higgs bosons h and H $(m_h < m_H)$, one CP odd state A and a pair of charged Higgs bosons $H^\pm$. From Eq. (2.21), interaction terms can be deduced to [3, 6]

$$\mathcal{L}_{e\rm LFV} = -\frac{m_{\ell_i}}{v\cos^2\beta}\left(\kappa^L_{i1}\overline{\ell_i}\mathrm{P}_L e + \kappa^R_{1i}\bar{e}\mathrm{P}_L\ell_i\right)\{\cos(\alpha-\beta)h + \sin(\alpha-\beta)H - i\,A\} + \text{H.c.}, \tag{2.22}$$

where P_L is the projection operator to the left-handed fermions, m_{ℓ_i} are mass eigenvalues of charged leptons, $v = \sqrt{2}\sqrt{\langle\Phi^0_1\rangle^2 + \langle\Phi^0_2\rangle^2}$ $(\simeq 246$ GeV), α is the mixing angle between the CP even Higgs bosons, and $\tan\beta \equiv \langle\Phi^0_2\rangle/\langle\Phi^0_1\rangle$.

Once a new physics model is assumed, κ^X_{ij} can be predicted as a function of the model parameters. In supersymmetric SMs, LFV Yukawa coupling constants can be radiatively generated by slepton mixing. Magnitudes of the LFV parameters κ^X_{ij} can be calculated as a function of the parameters of the slepton sector. For the scale of the dimensionful parameters in the slepton sector to be of TeV scales, we typically obtain $|\kappa^X_{ij}|^2 \sim (1\text{–}10)\times 10^{-7}$ [2, 3]. In the MSSMRN only κ^L_{ij} are generated by the quantum effect via the neutrino Yukawa couplings assuming flavour conservation at the scale of right-handed neutrinos.

Current experimental bounds on the effective LFV parameters κ^X_{ij} are obtained from the data of non-observation for various LFV processes [18]. For e–τ mixing, we obtain the upper bound from the semi-leptonic decay $\tau \to e\eta$ [5]; $|\kappa^L_{31}|^2 + |\kappa^R_{13}|^2 \lesssim 6.4\times 10^{-6}(\frac{50}{\tan\beta})^6(\frac{m_A}{350\text{GeV}})^4$, for $\tan\beta \gtrsim 20$ and $m_A \simeq m_H \gtrsim 160$ GeV (with $\sin(\beta-\alpha) \simeq 1$). The most stringent bound on e–μ mixing is derived from $\mu \to e\gamma$ data [19] as $(4/9)|\kappa^L_{21}|^2 + |\kappa^R_{12}|^2 \lesssim 4.3\times 10^{-4}(\frac{50}{\tan\beta})^6(\frac{m_A}{350\text{GeV}})^4$, for $\tan\beta \gtrsim 20$ and $m_A \simeq m_H \gtrsim 160$ GeV (with $\sin(\beta-\alpha) \simeq 1$). The upper bound on $(4/9)|\kappa^L_{21}|^2 + |\kappa^R_{12}|^2$ is expected to be improved at future experiments such as MEG and COMET for rare muon decays by a factor of $10^{2\text{–}3}$, while that on $|\kappa^L_{31}|^2 + |\kappa^R_{13}|^2$ is by $10^{1\text{–}2}$ at LHCb and SuperKEKB via rare tau decays [7, 8, 9, 10].

3 LFV Higgs production processes

We now discuss the lepton flavour violating Higgs boson production processes $e^-\gamma \to \ell^-\varphi$ $(\ell = \mu, \tau; \varphi = h, H, A)$ in $e\gamma$ collisions. The differential cross section is calculated

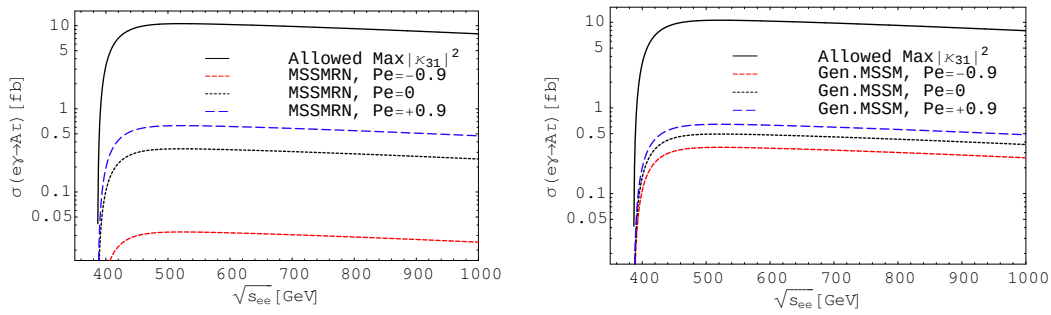

Figure 1: The production cross section of $e^-\gamma \to \tau^- A$ as a function of the center-of-mass energy $\sqrt{s_{ee}}$ of the electron-electron system. Solid curve represents the result in the THDM with the maximal allowed value of $|\kappa_{31}|^2$ under the current experimental data in both figures.

by using the effective LFV parameters κ_{ij}^X as

$$\frac{d\widehat{\sigma}_{e^-\gamma\to\ell_i^-\varphi}(\sqrt{s_{e\gamma}})}{d\cos\theta} = \frac{G_F\alpha_{\rm EM}m_\ell^2\beta_{\ell\varphi}}{16\sqrt{2}s_{e\gamma}}\frac{|\kappa_{i1}|^2}{\cos^4\beta}\frac{\eta_-(\eta_+^2+4z^2)-16z\,m_\ell^2/s_{e\gamma}}{\eta_-^2}, \tag{3.23}$$

where $z = (m_{\ell_i}^2 - m_\varphi^2)/s_{e\gamma}$ and $\beta_{\ell\varphi} = \sqrt{\lambda(m_{\ell_i}^2/s_{e\gamma}, m_\varphi^2/s_{e\gamma})}$ with $\lambda(a,b) = 1+a^2+b^2-2a-2b-2ab$. The functions are defined as $\eta_\pm = 1+z\pm\beta_{\ell\varphi}\cos\theta$ where θ is the scattering angle of the outgoing lepton from the beam direction. The effective LFV parameters can be written by

$$|\kappa_{i1}|^2 = \left[|\kappa_{i1}^L|^2(1-P_e)+|\kappa_{1i}^R|^2(1+P_e)\right]\times\begin{cases}\cos^2(\alpha-\beta) & \text{for } h\\ \sin^2(\alpha-\beta) & \text{for } H\\ 1 & \text{for } A\end{cases}, \tag{3.24}$$

where P_e is the polarization of the incident electron beam: $P_e = -1$ $(+1)$ represents that electrons in the beam are 100% left- (right-) handed.

At the ILC, a high energy photon beam can be obtained by Compton backward-scattering of laser and an electron beam [20]. The full cross section can be evaluated from that for the sub process by convoluting with the photon structure function as [20]

$$\sigma\left(\sqrt{s_{ee}}\right) = \int_{x_{min}}^{x_{max}} dx\, F_{\gamma/e}(x)\,\widehat{\sigma}_{e^-\gamma\to\ell^-\varphi}(\sqrt{s_{e\gamma}}), \tag{3.25}$$

where $x_{max} = \xi/(1+\xi)$, $x_{min} = (m_\ell^2+m_\varphi^2)/s_{ee}$, $\xi = 4E_e\omega_0/m_e^2$ with ω_0 to be the frequency of the laser and E_e being the energy of incident electrons, and $x = \omega/E_e$ with ω to be the photon energy in the scattered photon beam. The photon distribution function is given in Ref. [20]. We note that when $\sin(\beta-\alpha) \simeq 1$ and $m_H \simeq m_A$ (In the MSSM, this automatically realizes for $m_A \gtrsim 160$ GeV) signal from both $e^-\gamma \to \ell^- H$ and $e^-\gamma \to \ell^- A$ can be used to measure the LFV parameters, while the cross section for $e^-\gamma \to \ell^- h$ is suppressed.

In FIG. 1, we show the full cross sections of $e^-\gamma \to \tau^- A$ as a function of the center-of-mass energy of the e^-e^- system for $\tan\beta = 50$ and $m_A = 350$ GeV. Scattered leptons

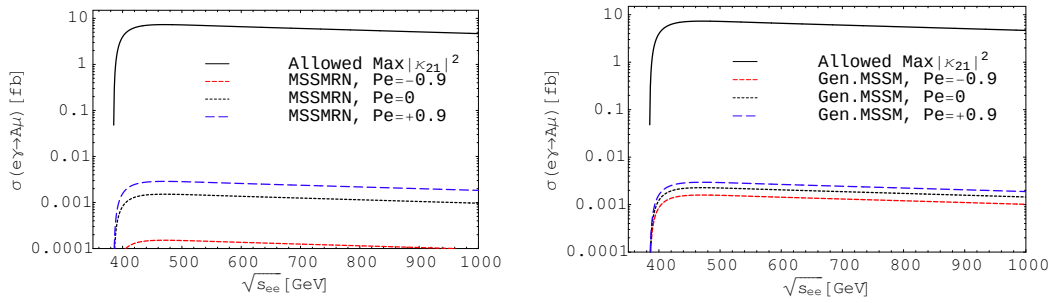

Figure 2: The production cross section of $e^-\gamma \to \mu^- A$ as a function of the center-of-mass energy $\sqrt{s_{ee}}$ of the electron-electron system. Solid curve represents the result in the THDM with the maximal allowed value of $|\kappa_{21}|^2$ under the current experimental data in both figures.

mainly go into the forward direction, however most of events can be detected by imposing the escape cut $\epsilon \leq \theta \leq \pi - \epsilon$ where $\epsilon = 20$ mrad [21]. The cross section can be around 10 fb with the maximal allowed values for $|\kappa_{31}|^2$ under the constraint from the $\tau \to e\eta$ data. The results correspond that, assuming the integrated luminosity of the $e\gamma$ collision to be 500 fb^{-1} and the tagging efficiencies of a b quark and a tau lepton to be 60% and 30%, respectively, about 10^3 of $\tau^- b\bar{b}$ events can be observed as the signal, where we multiply factor of two by adding both $e^-\gamma \to \ell^- A \to \ell^- b\bar{b}$ and $e^-\gamma \to \ell^- H \to \ell^- b\bar{b}$. Therefore, we can naively say that non-observation of the signal improves the upper bound for the e-τ mixing by 2–3 orders of magnitude if the backgrounds are suppressed. In FIG. 1 (left), those with a set of the typical values of $|\kappa^L_{31}|^2$ and $|\kappa^R_{13}|^2$ in the MSSMRN are shown for $P_e = -0.9$ (dashed), $P_e = +0.9$ (long dashed), and $P_e = 0$ (dotted), where we take $(|\kappa^L_{31}|^2, |\kappa^R_{13}|^2) = (2\times10^{-7}, 0)$. The cross sections are sensitive to the polarization of the electron beam. They can be as large as 0.5 fb for $P_e = -0.9$, while it is around 0.03 fb for $P_e = +0.9$. In FIG. 1 (right), the results with $(|\kappa^L_{31}|^2, |\kappa^R_{13}|^2) = (2\times10^{-7}, 1\times10^{-7})$ in general supersymmetric models are shown for each polarization of the incident electrons. The cross sections are a few times 1 fb and not sensitive for polarizations. Therefore, by using the polarized beam of the electrons we can separately measure $|\kappa^L_{31}|^2$ and $|\kappa^R_{13}|^2$ and distinguish fundamental models with LFV.

In FIG. 2, the full cross sections of $e^-\gamma \to \mu^- A$ are shown for $\tan\beta = 50$ and $m_A = 350$ GeV. Those with the maximally allowed values for $|\kappa_{21}|^2 = |\kappa^L_{21}|^2 + |\kappa^R_{12}|^2$ from the $\mu \to e\gamma$ datacan be 7.3 fb where we here adopted the same escape cut as before discussed [†]. This means that about a few times 10^3 of the signal $\mu^- b\bar{b}$ can be produced for the integrated luminosity of the $e\gamma$ collision to be 500 fb^{-1}, assuming tagging efficiencies to be 60% for a b quark and 100% for a muon, and using both $e^-\gamma \to \mu^- A$ and $e^-\gamma \to \mu^- H$. These results imply that $e\gamma$ collider can improve the bound on the e-μ by a factor of 10^{2-3}. Obtained sensitivity can be as large as those at undergoing MEG and projected COMET experiments. Because of the different dependencies on the parameters in the model, $\mu \to e\gamma$ can be sensitive than the LFV Higgs boson production for very high $\tan\beta (\gtrsim 50)$ with fixed Higgs boson mass. We also note that rare decay processes can measure the effect of

[†]If 10 mrad for the cut is taken instead of 20 mrad, the numbers of events are slightly enhanced; 10.6 fb to 11.0 fb (7.3 fb to 8 fb) for the τ-φ (μ-φ) process.

other LFV origin when Higgs bosons are heavy. Therefore, both the direct and the indirect measurements of LFV processes are complementary to each other. In FIG. 2 (left), those in the MSSMRN are shown for $P_e = -0.9$ (dashed), $P_e = +0.9$ (long dashed), and $P_e = 0$ (dotted), where we take $(|\kappa_{21}^L|^2, |\kappa_{12}^R|^2) = (2 \times 10^{-7}, 0)$. They can be as large as a few times 10^{-3} fb for $P_e = -0.9$ and $P_e = 0$, while it is around 10^{-4} fb for $P_e = +0.9$. In FIG. 2 (right), the results with $(|\kappa_{21}^L|^2, |\kappa_{12}^R|^2) = (2 \times 10^{-7}, 1 \times 10^{-7})$ are shown in general supersymmetric models in a similar manner.

It is understood that these processes are clear against backgrounds. For the processes of $e^-\gamma \to \tau^-\varphi \to \tau^- b\bar{b}$. The tau lepton decays into various hadronic and leptonic modes. The main background comes from $e^-\gamma \to W^- Z\nu$, whose cross section is of the order of 10^2 fb. The backgrounds can strongly be suppressed by the invariant mass cut for $b\bar{b}$. The backgrounds for the process $e^-\gamma \to \mu^-\varphi \to \mu^- b\bar{b}$ also comes from $e^-\gamma \to W^- Z\nu \to \mu^- b\bar{b}\nu\overline{\nu}$ which is small enough. Signal to background ratios are better than $\mathcal{O}(1)$ before kinematic cuts. They are easily improved by the invariant mass cut, so that our signals can be almost background free.

4 Conclusion

We have studied the Higgs boson associated LFV at an electron photon collider. Lots of new physics model can predict the LFV Yukawa interactions. The cross section for $e^-\gamma \to \ell^-\varphi$ ($\ell = \mu, \tau; \varphi = H, A$) can be significant for the allowed values of the effective LFV couplings under the current experimental data. By measuring these processes at the ILC, the current upper bounds on the effective LFV Yukawa coupling constants are expected to be improved in a considerable extent. Such an improvement can be better than those at MEG and COMET experiments for the e-μ-φ vertices, and those at LHCb and SuperKEKB for the e-τ-φ vertices. Moreover, the chirality of the LFV Higgs coupling can be separately measured via these processes by using the polarized electron beam. The electron photon collider can be an useful tool of measuring Higgs boson associated LFV couplings.

Acknowledgments
The authors would like to thank the members of the ILC physics subgroup [22] for useful discussions. The work of S.K. was supported, in part, by Grant-in-Aid, Ministry of Education, Culture, Sports, Science and Technology, Government of Japan, No. 18034004.

References

[1] S. Kanemura and K. Tsumura, Phys. Lett. B **674** (2009) 295.

[2] F. Borzumati and A. Masiero, Phys. Rev. Lett. **57**, 961 (1986); J. Hisano, T. Moroi, K. Tobe, M. Yamaguchi and T. Yanagida, Phys. Lett. B **357**, 579 (1995); J. Hisano, T. Moroi, K. Tobe and M. Yamaguchi, Phys. Rev. D **53**, 2442 (1996);

[3] J. Hisano and D. Nomura, Phys. Rev. D **59**, 116005 (1999); A. Brignole and A. Rossi, Phys. Lett. B **566**, 217 (2003), Nucl. Phys. B **701**, 3 (2004).

[4] K. S. Babu and C. Kolda, Phys. Rev. Lett. **89**, 241802 (2002); A. Dedes, J. R. Ellis and M. Raidal, Phys. Lett. B **549**, 159 (2002).

[5] M. Sher, Phys. Rev. D **66**, 057301 (2002).

[6] S. Kanemura, T. Ota and K. Tsumura, Phys. Rev. D **73**, 016006 (2006).

[7] T. Mori *et al.*, "Search for $\mu \to e\gamma$ Down to 10^{-14} Branching Ratio". Research Proposal to Paul Scherrer Institut. See also `http://meg.web.psi.ch/`.

[8] D. Bryman *et al.*, "An Experimental Proposal on Nuclear and Particle Physics Experiments at J-PARC 50 GeV Proton Synchrotron". Research Proposal to J-PARC.

[9] P. Bartalini *et al.* [LHCb Collaboration], Nucl. Phys. Proc. Suppl. **98**, 359 (2001).

[10] A. G. Akeroyd *et al.* [SuperKEKB Physics Working Group], arXiv:hep-ex/0406071.

[11] ATLAS Collaboration, `http://atlas.web.cern.ch/Atlas/`; CMS Collaboration, `http://cms.cern.ch/`.

[12] A. Djouadi *et al.* [ILC Collaboration], arXiv:0709.1893; See also `http://www.linearcollider.org/cms/`.

[13] NFMCC Collaboration, `http://www.cap.bnl.gov/mumu/`; Y. Kuno and Y. Mori, "NufactJ Feasibility Study Report".

[14] K. A. Assamagan, A. Deandrea and P. A. Delsart, Phys. Rev. D **67**, 035001 (2003).

[15] S. Kanemura, K. Matsuda, T. Ota, T. Shindou, E. Takasugi and K. Tsumura, Phys. Lett. B **599**, 83 (2004); E. Arganda, A. M. Curiel, M. J. Herrero and D. Temes, Phys. Rev. D **71**, 035011 (2005).

[16] S. Kanemura, Y. Kuno, M. Kuze and T. Ota, Phys. Lett. B **607**, 165 (2005).

[17] J. F. Gunion, H. E. Haber, G. Kane, and S. Dawson, *The Higgs Hunters Guide, Perseus Publishing, Cambridge, MA, 1990.*

[18] M. L. Brooks *et al.* [MEGA Collaboration], Phys. Rev. Lett. **83**, 1521 (1999); U. Bellgardt *et al.* [SINDRUM Collaboration], Nucl. Phys. B **299**, 1 (1988); B. Aubert *et al.* [BABAR Collaboration], Phys. Rev. Lett. **96**, 041801 (2006); Y. Miyazaki *et al.* [BELLE Collaboration], Phys. Lett. B **648**, 341 (2007); B. Aubert *et al.* [BaBar Collaboration], Phys. Rev. Lett. **95**, 191801 (2005); K. Abe *et al.* [Belle Collaboration], arXiv:0708.3272.

[19] C. Amsler *et al.* [Particle Data Group], Phys. Lett. B **667**, 1 (2008).

[20] I. F. Ginzburg, G. L. Kotkin, S. L. Panfil, V. G. Serbo and V. I. Telnov, Nucl. Instrum. Meth. A **219**, 5 (1984).

[21] D. A. Anipko, M. Cannoni, I. F. Ginzburg, K. A. Kanishev, A. V. Pak and O. Panella, arXiv:0806.1760.

[22] http://www-jlc.kek.jp/subg/physics/ilcphys/.

Feasibility study of Higgs pair creation in $\gamma\gamma$ collider

Nozomi Maeda[(a)], **Keisuke Fujii**[(b)], **Katsumasa Ikematsu**[(b)], **Shinya Kanemura**[(c)], **Yoshimasa Kurihara**[(b)], and **Tohru Takahashi**[(a)]

[(a)] *Advanced Sciences of Matter, Hiroshima University, Higashi-Hiroshima, Japan*
[(b)] KEK, Tsukuba, Japan
[(c)] Department of Physics, University of Toyama, Japan

We studied a feasibility of measuring Higgs boson pair production in a Photon Linear Collider. The optimum energy of $\gamma\gamma$ collision was estimated with a realistic luminosity distribution. We also discussed simulation study for detecting the signal against W boson pair backgrounds.

1 Introduction

As a possible option of the International Linear Collider, feasibility of physics orotundities of high energy photon-photon interaction has been considered. In the high energy photon linear colliders(PLCs), high energy photon beams are generated by inverse Compton scattering between the electron and the laser beams as illustrated in figure 1. Feasibility of the PLC for both physics and technical aspect, has been studied and summarized in [1]. In these study, one assumed integrated luminosity of 3 4 years PLC operation which, for example, may happens after initial operation of e^+e^- mode of the ILC at $\sqrt{s} = 500$GeV.

In this study, we investigated a feasibility of self-coupling of the Higgs boson as an example of a precise measurement with the PLC by assuming an ultimate integrated luminosity, i.e., 10years operation with a high luminosity parameters.

The Higgs boson self-coupling constant is reprensented by $\lambda = \lambda^{SM}(1 + \delta\kappa)$ which contributes Higgs boson pair production via a diagram shown in figure 2. Here, λ^{SM} is Higgs boson self-coupling constant which is included in the Standard Model. $\delta\kappa$ represent the deviation from the Standard Model.

The self-coupling of the Higgs boson can also be studied in e^+e^- collision via the diagram shown in figure 3. Comparing with the

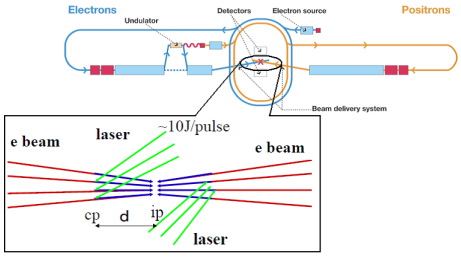

Figure 1: An outline of PLC. Positron beam of ILC is replaced with electron beam. High energy photon is generated by collision between laser and electron beam.

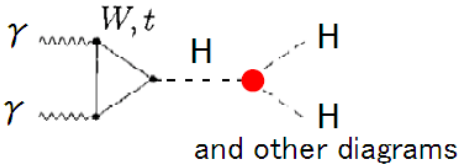

Figure 2: An example of $\gamma\gamma \to HH$ diagram. Higgs self-coupling occurs at red point.

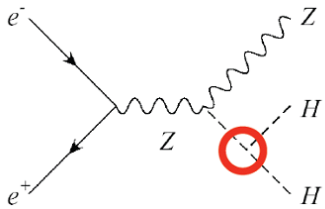

Figure 3: $e^+e^- \to ZHH$ diagram. Higgs self-coupling occurs at red circle.

$e^+e^- \to ZHH$ channel, where Higgs boson pairs are associated with the Z boson production, the Higgs bosons are produced by s channel via loop diagrams in $\gamma\gamma$ collision. Therefore, contribution of the $\delta\kappa$ to the production cross section is difference for the e^+e^- and for $\gamma\gamma$ and studies in these two modes will be complementary each other. Detail of the theoritical background in this analysis can be found in [2].

2 Sensitivity Sutdy

For optimization photon-photon collision energy, we defined the sensitivity for the $\delta\kappa$ as;

$$sensitivity = \frac{|N(\delta\kappa) - N_{SM}|}{\sqrt{N_{obs}}} = \frac{L|\eta\sigma(\delta\kappa) - \eta\sigma_{SM}|}{\sqrt{L(\eta\sigma(\delta\kappa) + \eta_B\sigma_B)}}$$

where, $N(\delta\kappa)$ is a expected number of events as a function of $\delta\kappa$ and N_{SM} is the number of events expected from the Standard Model. $L, \eta, \sigma(\delta\kappa), \sigma_{SM}, \eta_B$ and σ_B are integrated luminosity, detection efficiency of signal, cross section with $\delta\kappa$, cross section with the Standard model, detection efficiency for background events and the cross section for background processes, respectively. For $\eta = 1$, $\eta_B = 0$, sensitivity is written;

$$sensitivity = \sqrt{L}\frac{|\sigma(\delta\kappa) - \sigma_{SM}|}{\sqrt{\sigma(\delta\kappa)}}$$

The Higgs boson mass of 120GeV and the integrated luminosity of 1000fb^{-1} was assumed in the study. The cross section is calculated by the formula which is described in [3] with a theoretically calculated PLC luminosity spectrum. The sensitivity as a function of the center of mass energy of the $\gamma\gamma$ collision for $\delta\kappa = 1$ and -1 is plotted in figure 4.

From the figure, the optimum energy for the $\gamma\gamma$ collision for Higgs boson mass of 120GeV was found to be around 270GeV.

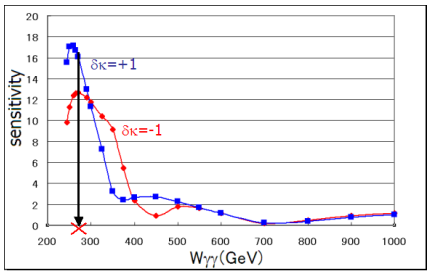

Figure 4: A graph showing sensitivity v.s. $W_{\gamma\gamma}$. $W_{\gamma\gamma}$ means photon-photon collision energy. Sensitivity has peak at near $W_{\gamma\gamma} \simeq 270$GeV, not depend on $\delta\kappa$.

3 Background

Figure 5 shows cross section as a function of collision energy for photon-photon interactions. Figure 5 indicates that $\gamma\gamma \to WW$ is main background with the production cross section of about 90pb. On the other hand,

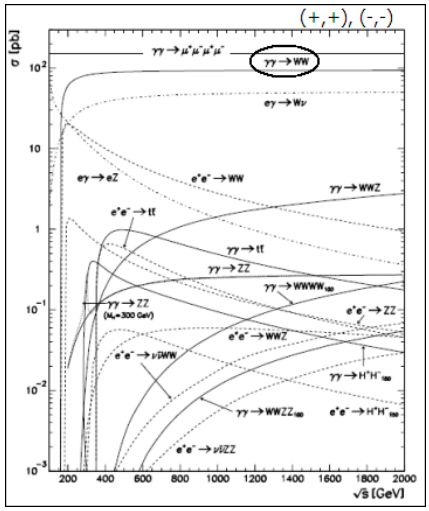

Figure 5: cross section v.s. collision energy. $\gamma\gamma \to WW$ is main background against $\gamma\gamma \to HH$.

signal cross section is 0.044fb at optimized energy. Therefore, observation of signal requires background suppression of 10^{-7}. The other reaction that has large cross section such as $\gamma\gamma \to WWZ$ and $\gamma\gamma \to t\bar{t}$. However the optimum energy for $\gamma\gamma \to HH$ is below these threshold for these channel.

4 Simulation Framework

JLC Study Framework(JSF) is used as simulation framework in this study [15].

The helicity amplitude for the signal is calculated by theoritical calculation program [5]. The helicity amplitude for background processes were calculated by a helicity amplitude calculation package; HELAS [6].

The luminosity distribution used in the analysis were generated using the CAIN[7] program with the input parameters shown in table 1 [8]. The luminosity spectrum simulated with the CAIN is shown in figure 6.

From these helicity amplitude and luminosity spectrum, BASES/SPRING integrated and generated events. Pythia made parton shower and hadronized. Quick detector simulator read particle list that from pythia. Finaly, data from Quick Detector Simulator is analyzed.

With this spectrum, we expect signal of 16event/year, while 10^7event/year for background.

5 Analysis

The decay branching ratio of the Higgs boson of 120GeV is shown in table 2. Since main decay mode of the Higgs boson of 120GeV is b-quark pairs with the branching ratio of about 0.67, we tried the case that both Higgs boson decayed into b-quark pairs.

For each event, we applied forced four jets analysis in which a clustering algorithm is applied to an event by changing the clustering parameter until the event is catego-

Table 1: Input parameters to CAIN. This parameters set make luminosity peak at optimum energy.

$E_e[GeV]$	190
$N/10^{10}$	2
$\sigma_z[mm]$	0.35
$\gamma\varepsilon_{x/y}/10^{-6}[mrad]$	2.5/0.03
$\beta_{x/y}[mm]@IP$	1.5/0.3
$\sigma_{x/y}[nm]$	96/4.7
$\lambda_L[nm]$	1054
Pulse energy$[J]$	10
$x = 4\omega E_e/m_e^2$	3.76

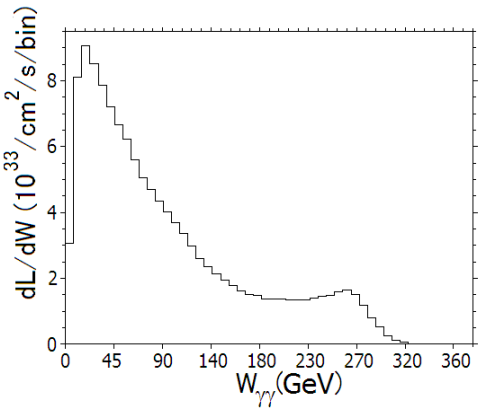

Figure 6: Luminosity spectrum generated by CAIN using table 1 parameters set.

Table 2: Branching ratio of Higgs particle.

particles	Branching ratio
$b\bar{b}$	0.6774
$\mu\mu$	0.00024
$c\bar{c}$	0.02982
$\tau\tau$	0.06916
$s\bar{s}$	0.00051
gg	0.0713
$\gamma\gamma$	0.002231
γZ	0.001084
WW	0.1331
ZZ	0.0152

rized as a four jets event. After the forced four jets analysis, invariant masses for jet pairs were calculated. For a four jets event, we must to choose a right jets pairs originating from parent Higgs (or W for the background) bosons out of three possible combinations. For this purpose, we defined χ^2s as;

$$\chi^2_H = \frac{(M_1 - M_H)^2}{\sigma^2_{2j}} + \frac{(M_2 - M_H)^2}{\sigma^2_{2jH}}$$

$$\chi^2_W = \frac{(M_1 - M_W)^2}{\sigma^2_{2j}} + \frac{(M_2 - M_W)^2}{\sigma^2_{2jW}}$$

where, M_1 and M_2 are reconstructed particle mass, M_H and M_W are Higgs boson and W boson mass respectively, with σ_{2jH} and σ_{2jW} being their resolutions. The jet of the least χ^2 was chosen to be the most probable combination for an event. Figure 7 shows correlation of χ^2_H and χ^2_W for the most probable combination. To enhance Higgs boson from the W boson events, we choosed an event satisfies $-140/20 \times \chi^2_H + 140 \geq \chi^2_W$. The mass distributions for the Higgs and W boson events after χ^2 cut are shown in figure 8.

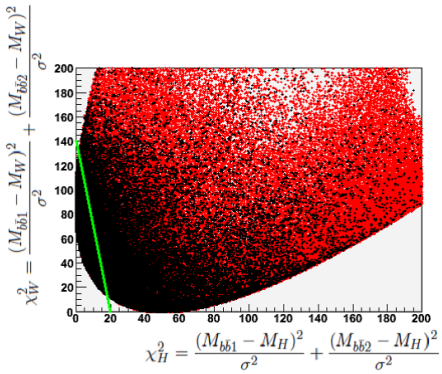

Figure 7: Reconstructed particles χ^2 distribution. Black indicates signal events, red indicates background events. Green line is represented by $-140/20 \times \chi^2_H + 140 = \chi^2_W$. Here, to make signal clear, signal cross section is about 5×10^4 times as large as usual.

6 b-tagging

By the χ^2 analysis described in previous section, the W boson background was suppressed by 0.0541 while keeping the 46% efficiency for the Higgs boson events. In order further improve signal to background ratio, we applied b-quark tagging method for remaing events.

Figure 9 illustrates a b-quark tagging method we applied. For each track in a reconstucted jet, $N_{sig} = L/\sigma_L$ was calculated, where L is the least approach to the interaction point of the track in the plane perpendicular to the beam and σ_L being its resolution. Then, $N_{off}(a)$, number of track which has $N_{sig} > a$, is calculated for each jet as a function of a. In current analysis we requied all jets must satisfy $N_{off}(3.5) \geq 2$. Figure 10 is the χ^2 plot after b-tagging but before χ^2 cuts. We obtaned backgroud suppression of $1.35 \pm 0.18 \times 10^{-6}$ and efficiency of signal of 0.1454 ± 0.0044, where the errors

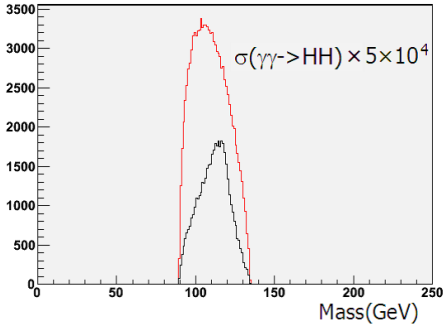

Figure 8: Reconstructed particle mass spectrum that cutted. Background is suppressed, but not enough.

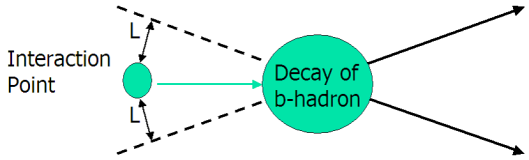

Figure 9: An outline of nsig method. B-hadron is generated at interaction point and decay at "Decay of b-hadron". Arrows mean particle tracks. Dotted line means extrapolate particle tracks.

are from statistic of the Monte Carlo simulation. For remaining envents, χ^2 cut were applyied. As a results, no WW events survied out of 3.85×10^7 simulated events while keeping signal efficiency of 0.1096 ± 0.0014.

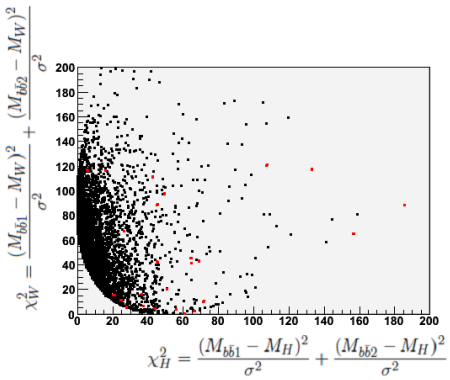

Figure 10: A result of b-tag selection. Number of b-tagged jets = 4 is required. Black indicates signal event. Red indicates background event. Number of remained background event is 52.

7 Summary and prospect

We studied feasibility of measurement of Higgs self-coupling constant at the PLC. For Higgs mass of 120GeV, optimum photon-photon collision energy for observe $\gamma\gamma \rightarrow HH$ was found to be about 270GeV. With a parameters of PLC(TESLA-optimistic), 16events/year is expected for Higgs boson events while main background of $\gamma\gamma \rightarrow WW$ is about 10^7events/year.

We tried an event selection with kinematical parameters and b-quark tagging by the simulation and found that backgound suppression of 10^{-7} with keeping signal efficiency of about 10% seemed to be possible.

For further analysis, we plan to improve signal efficicency by :

optimization of selection criteria for $HH \rightarrow b\bar{b}b\bar{b}$ mode.

study for $HH \rightarrow b\bar{b}WW^*$ decay.

For the backgound, it is necessary to estimate contribution from $\gamma\gamma \rightarrow ZZ$ events.

8 Acknowledgement

The authors would like to thank the ILC physics working group for valuable discussion and suggestion.

References

[1] E.Boos, A.De Roeck, I.F.Ginzburg, K.Hagiwara, R.D.Heuer, G.Jikia, J.Kwiecinski, D.J.Miller, T.Takahashi, V.I.Telnov, T.Rizzo, I.Watanabe, P.M.Zerwas *"Gold-plated processes at photon colliders"* (2001) arXiv:hep-ph/0103090v1

[2] G.Jikia *"Pair production of W bosons at the photon linear collider:a window to the electroweak symmetry breaking?"* (1997) arXiv:hep-ph/9708373v1

[3] E.Asakawa, D.Harada, S.Kanemura, Y.Okada, K.Tsumura *"Higgs boson pair production at a photon-photon collision in the two Higgs doublet model"* (2008) arXiv:0809.0094v2[hep-ph]

[4] *"The JSF home page"* http://www-jlc.kek.jp/subg/offl/jsf/

[5] *"Shinya Kanemura's page"* http://jodo.sci.u-toyama.ac.jp/~kanemu/

[6] *"HELAS Tutorial"* http://madgraph.kek.jp/~kanzaki/Tutorial/tutorial.html

[7] *"Available computer programs on FFIR"* http://www-jlc.kek.jp/subg/ir/Program-e.html

[8] IB.Badelek *et al.*, *"The Photon Collider at TESLA"* (2004) International Journal of Modern Physics A19/, 5097-5186

Analysis of Tau-pair process in the ILD reference detector model

Taikan Suehara[(a)]

[(a)] *International Center for Elementary Particle Physics The University of Tokyo, Hongo 7-3-1, Bunkyo District, Tokyo 113-0033, Japan*

Tau-pair process has been analyzed in the ILD detector model as a benchmark process for LoI. Results of background rejection, forward-backward asymmetry and polarization measurements are obtained with full detector simulation.

1 Goals for LoI

Tau-pair process ($e^+e^- \to Z^*, \gamma \to \tau^+\tau^-$) at $\sqrt{s} = 500$ GeV is one of the benchmark processes[1] proposed by Research Director. According to the report, this process is a good sample to examine detector performances of

- tau reconstruction, aspects of particle flow,
- π_0 reconstruction,
- tracking of very close-by tracks.

In this process, tau leptons are highly boosted ($\gamma \sim 140$), thus decay daughters (mainly charged and neutral pions, muons and electrons) are concentrated in a very narrow angle. Reconstruction of π_0 from two photons is especially challenging for the ILC detectors.

Observables for the LoI are cross section, forward-backward asymmetry and polarization of tau leptons. The polarization measurement requires identification of tau decays, including reconstruction of π_0. Efficiency and purity of event selection cuts should be also a good measure of detector performance.

For physics motivation, tau-pair process is important as a precision measurement of the electroweak theory. For example, measuring cross section and forward-backward asymmetry of tau-pair process very precisely can probe existence of heavy Z' boson.

2 Analysis framework and events

2.a Event samples

Events of ILD_00 LoI mass production[2] are used for this study. Events reconstructed and listed at DESY by approximately end of February are used in this analysis. 10.3 M SM events generated in SLAC are processed for background estimation with appropriate event weight.

Since the SLAC events have a polarization issues for tau-pair events, tau-pair events generated in DESY are used instead of SLAC events in this analysis. For other modes including tau, SLAC events are used. Whizard 1.51 and TAUOLA[14] are used to generate

the DESY events. Statistics of the signal channel is 500 fb^{-1} both for $e^-_L e^+_R$ and $e^-_R e^+_L$ (total 2.3 M events).

Bhabha process (e^+e^- elastic scattering) is an important background for tau-pair analysis. Since the cross section of Bhabha process is too large ($\sim$ 17 nb for each polarization in SLAC events), following preselection is applied to the SLAC events before simulation.

- $|\cos\theta|$ of electron or positron must be smaller than 0.96.
- Opening angle between electron and positron must be larger than 165 deg.

After the preselection, the cross section is reduced to 50-90 pb. $\sim$1.0 fb^{-1} of preselected Bhabha events are simulated.

Preselection is also applied to $\gamma\gamma \to \tau\tau$ events with following cuts:

- Opening angle between two taus must be larger than 170 deg.
- Energy sum of two taus is greater than 30 GeV.

The total cross section after the cuts is around 18 pb. Around 100 k events passing preselection are processed.

Integrated luminosity is assumed to be 500 fb^{-1} each for two polarization setups, $e^-_L e^+_R$ and $e^-_R e^+_L$. Assumed polarization ratio is 80% for electron and 30% for positron (i.e. for $e^-_L e^+_R$ setup 90% of electrons are leftly polarized and 65% of positrons are rightly polarized).

2.b Tau clustering

For tau clustering, an original clustering processor (TaJet) is applied to the output of PandoraPFA. Following is a procedure of the processor.

1. Sort particles in energy order.
2. Select the most energetic charged particle (a tau candidate).
3. Search particles to be associated to the tau candidate. Criteria is:
   (a) Opening angle to the tau candidate is smaller than 50 mrad., or
   (b) Opening angle to the tau candidate is not larger than 1 rad. and invariant mass with the tau candidate is less than 2 GeV (m_τ = 1.777 GeV).
4. Combine energy and momentum of the tau candidate and associated particle and treat the combined particle as the new tau candidate.
5. Repeat from 3.
6. After all remaining particles do not meet the criteria, remaining most energetic charged particle is the next tau candidate. (Repeat from 2.)
7. After all charged particles are associated to tau candidates, remaining neutral particles are independently included in the cluster list as neutral fragments.

In the clustering stage, events with > 6 tracks are pre-cut to accelerate clustering since $> 99\%$ of tau decays have ≤ 3 charged particles. Event with only one positive and one negative tau clusters are processed with latter analysis.

Cuts	Tau-pair	Bhabha	$\mu\mu$	nℓ + nν	$\gamma\gamma \to \ell\ell$	other $\gamma\gamma$, eγ	other
# tracks, # clusters	573180	2.88e+07	590770	1.15e+06	5.58e+08	4.07e+06	1.21e+06
Opening angle > 178 deg.	152865	1.89e+07	157430	7938	6.93e+06	59454	2633
$\lvert\cos\theta\rvert < 0.95$	142371	1.39e+07	147571	5020	6.25e+06	57746	610
ee, $\mu\mu$ veto	130383	96482	1606	3225	616265	45645	141
$70 < E_{vis} < 450$ GeV	125400	5071	635	2953	1641	0	32

(a) e^-_L (80%) e^+_R (30%)

Cuts	Tau-pair	Bhabha	$\mu\mu$	nℓ + nν	$\gamma\gamma \to \ell\ell$	other $\gamma\gamma$, eγ	other
# tracks, # clusters	446551	2.68e+07	460874	116198	5.58e+08	46898050	1194395
Opening angle > 178 deg.	127070	1.73e+07	133628	519	6.93e+06	59920	2934
$\lvert\cos\theta\rvert < 0.95$	118426	1.23e+07	125113	326	6.25e+06	58987	512
ee, $\mu\mu$ veto	108778	88385	1027	200	616265	46196	107
$70 < E_{vis} < 450$ GeV	103197	4857	383	183	1641	0	16

(b) e^-_R (80%) e^+_L (30%)

Table 1: Cut statistics for background suppression. Preselection (See Section 2.a for details) is applied for Bhabha events before these cuts. Number of events are normalized to 500 fb^{-1}. The same statistics is used for (a) and (b): only event weighting is different.

3 Background suppression

Main background of tau-pair analysis is Bhabha ($e^+e^- \to e^+e^-$), WW $\to \ell\nu\ell\nu$ and $\gamma\gamma \to \tau^+\tau^-$. Since cross sections of Bhabha and two-photon events are huge (about 10^4 and 10^3 larger than signal, respectively), we need tight selection cuts for those background events. Following cuts are applied to signals and all SM background events after the tau clustering.

1. Number of tracks ≤ 6. Included as a pre-cut in tau clustering processor.

2. Only one positive and one negative tau clusters must exist in the event. (Neutral clusters are allowed.)

3. Opening angle of two tau candidates must be > 178 deg.

   This cut efficiently suppresses WW $\to \ell\nu\ell\nu$ background.

4. ee and $\mu\mu$ events are rejected.

   Charged particles depositing > 90% of their energy in ECAL are identified as electrons, and charged particles depositing < 70% of their energy (estimated by curvature of their tracks) in ECAL+HCAL are identified as muons. Events with two electrons or two muons are rejected in this cut. This cut is especially for suppressing Bhabha and $e^+e^- \to \mu^+\mu^-$ events. Signal loss is about 6%.

5. $\lvert\cos\theta\rvert < 0.95$ for both tau clusters.

   t-channel Bhabha events are almost completely suppressed by this cut. 20% of signal events are lost.

6. $70 < E_{vis} < 450$ GeV. E_{vis} does not include energy of neutral clusters.

   Lower bound suppresses $\gamma\gamma \to \tau^+\tau^-$ events, and upper bound suppresses Bhabha events. Signal lost is negligibly small.

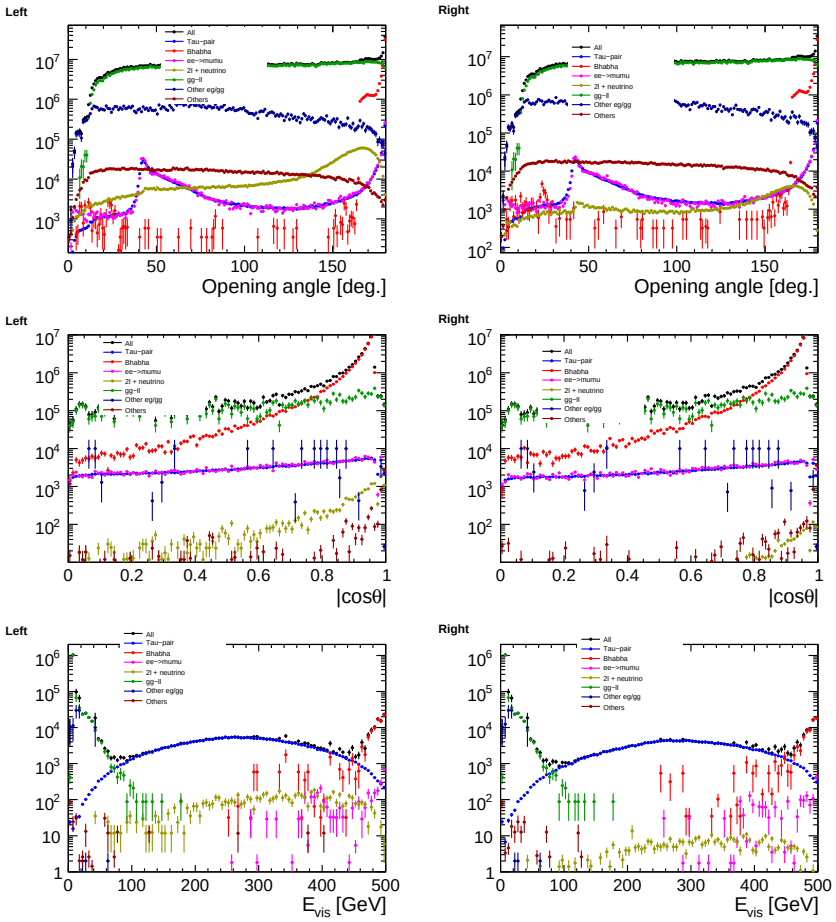

Figure 1: Distribution of cut values. Left column shows $e^-_L e^+_R$ distribution and Right column shows $e^-_R e^+_L$ distribution. Cuts are applied from top, and ee and $\mu\mu$ veto cuts are applied between second and third rows, whose distributions are omitted.

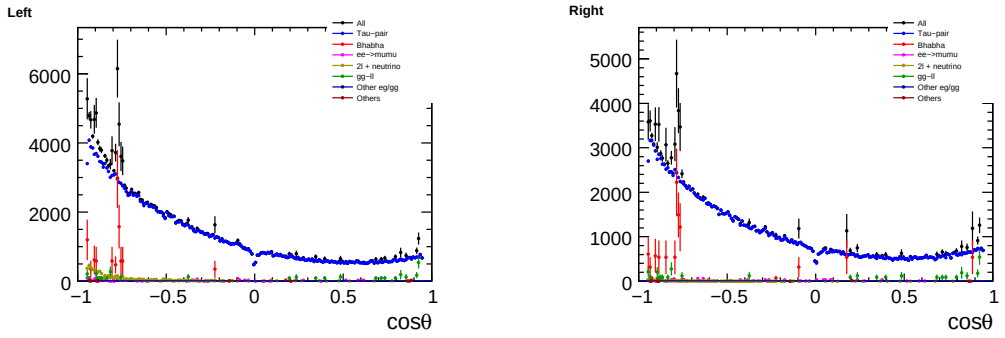

(a) e_L^- (80%) e_R^+ (30%)

(b) e_R^- (80%) e_L^+ (30%)

Figure 2: Angular distribution of τ^+ momentum direction. Number of events are normalized to 500 fb^{-1}. Error bars stand for statistical errors in current MC statistics. The same statistics is used for (a) and (b): only event weighting is different.

Table 1 shows the result of these cuts and Figure 1 shows distribution of cut values. Most of the background is effectively cut off by the cuts, ∼10% level of the signal. Remaining background is mainly Bhabha, $\gamma\gamma \to \tau\tau$ and WW→ $\ell\nu\ell\nu$.

Purity of tau selection is 92.4% in $e_L^- e_R^+$ sample and 93.6% in $e_R^- e_L^+$. The difference is mainly from difference of the cross section between each polarization.

Selection efficiency of tau-pair events is literally low (15.8% in $e_L^- e_R^+$ and 16.3% in $e_R^- e_L^+$). However, the 'nocut' number contains radiative events, which have effectively lower $\sqrt{s}$ and should not be used in the analysis. These radiative events are cut by the opening angle selection. The real efficiency varies by the definition of the events. The acceptance of 'softly-radiated' tau-pair events is determined by the opening angle cuts. Loosing the cut accepts more events, although $\gamma\gamma \to \tau\tau$ and WW→ $\ell\nu\ell\nu$ background significantly increase.

4 Cross section

Cross section can be easily obtained by count-based method since background amount is low. Assuming background subtraction can be performed in the error of statistics, we obtain number of signal event as 125400±368 ($e_L^- e_R^+$) and 103197±332 ($e_R^- e_L^+$), ie. 0.29% and 0.32% statistical error, respectively. The statistical error is dominated by signal statistics, so poor statistics of background events in the current MC sample can only have small effect on these numbers (0.30% and 0.33% statistical error, even if background is doubled). Systematic error can be introduced by polarization error, MC incorrespondance to real detector etc., but it cannot be accurately estimated in this stage of detector development and thus not considered now.

5 Forward-backward asymmetry

Figure 2 shows a result on angular distribution of τ^+ leptons (τ^- events are essentially the same event-by-event since we require opening angle > 178 deg.).

Assuming that background can be subtracted effectively, forward-backward asymmetry is calculated by following formulae.

$$A_{FB} = \frac{N_F - N_B}{N_F + N_B}, \tag{5.26}$$

$$\sigma A_{FB} = \sqrt{\left(\frac{\partial A_{FB}}{\partial N_F}\sigma N_F\right)^2 + \left(\frac{\partial A_{FB}}{\partial N_B}\sigma N_B\right)^2}, \tag{5.27}$$

$$\sigma N_F = \sqrt{N_F + N_{FBG}}, \quad \sigma N_B = \sqrt{N_B + N_{BBG}}, \tag{5.28}$$

where N_B is number of signal events in backward region ($\cos\theta < 0$), N_F is number of signal events in forward region ($\cos\theta > 0$), N_{BBG} is number of background events in the backward region and N_{FBG} is number of background events in the forward region. The formulae can be reduced to

$$\sigma A_{FB} = \frac{2\sqrt{N_B^2(N_F + N_{FBG}) + N_F^2(N_B + N_{BBG})}}{(N_F + N_B)^2}. \tag{5.29}$$

Result of the calculation is:

$$e_L^- e_R^+ \quad : \quad N_F = 95529, N_B = 29872, N_{FBG} = 9201, N_{BBG} = 1130, A_{FB} = 52.36 \pm 0.25\% \tag{5.30}$$

$$e_R^- e_L^+ \quad : \quad N_F = 75556, N_B = 27640, N_{FBG} = 5477, N_{BBG} = 1605, A_{FB} = 44.19 \pm 0.28\% \tag{5.31}$$

Statistical accuracy of A_{FB} is 0.48% and 0.63%, respectively.

6 Decay mode separation

Separating decay modes of tau is essential for the polarization measurement. There are five dominant decay modes of tau, $\tau^+ \to e^+\overline{\nu_e}\nu_\tau$ (17.9%), $\tau^+ \to \mu^+\overline{\nu_\mu}\nu_\tau$ (17.4%), $\tau^+ \to \pi^+\nu_\tau$ (10.9%), $\tau^+ \to \rho^+\nu_\tau \to \pi^+\pi^0\nu_\tau$ (25.2%), and $\tau^+ \to a_1^+\nu_\tau \to \pi\pi\pi\nu_\tau$ (9.3% (1-prong) and 9.0% (3-prong)). Other decay modes (10.3%) include Kaons and multi-pions in other resonant modes or continuum.

We utilize a neural network for the decay mode selection. Two separate networks are trained for 1-prong and 3-prong events. 1-prong decay includes $e^+\overline{\nu_e}\nu_\tau$, $\mu^+\overline{\nu_\mu}\nu_\tau$, $\pi^+\nu_\tau$, $\rho^+\nu_\tau$ and $a_1^+\nu_\tau$ modes. Input variables of the 1-prong neural net are as follows.

- Two lepton-ID values. Likelihood-based lepton ID software was developed, but due to the known issues of the event production the lepton ID is not properly worked on the mass production sample. As a simpler lepton ID, we use ratio between the energy deposit of the electromagnetic calorimeter (ECAL) and the total deposit energy for the electron ID, and ratio between the calorimeter energy deposit and the track momentum for the muon ID. These two variables are included in the neural network. (Variable (a) and (b).)

- Energy of the charged particle and two kinds of energy sums of the neutral particles. The neutral energy sums contain particles whose ECAL energy deposit is $> 80\%$, and $< 80\%$ of the total energy deposit, respectively. Particles with ECAL energy deposit $< 80\%$ are considered to be hadrons, which contain more spurious particles from a mis-fragmentation of energetic charged particles mainly at HCAL. The energy sums are especially expected to discriminate π mode. (Variable (c), (d) and (e).)

- Number of neutral particles except neutral hadrons. Number of photons is a powerful information to separate ρ (expected number of photons is 2) and a_1 (expected number of photons is 4). (Variable (f).)

- Invariant masses of all reconstructed particles except neutral hadrons and invariant masses of photons. Invariant masses of all reconstructed particles should equal to the masses of intermediate particles, ρ and a_1. If photons are reconstructed properly, invariant masses of photons are close to that of π_0. For the photon / hadron separation, above criteria is used again. (Variable (g) and (h).)

- Energy of the third-energetic neutral particle. This variable is also to separate ρ and a_1. Since ρ can have at most two photons, energy of the third photon should be small even if it exists in the ρ mode. (Variable (i).)

We use two hidden layers, first layer has 18 neurons and second has 9 neurons. The output neurons are likelihood value of $e^+\overline{\nu_e}\nu_\tau$, $\mu^+\overline{\nu_\mu}\nu_\tau$, $\pi^+\nu_\tau$, $\rho^+\nu_\tau$ and $a_1^+\nu_\tau$ modes (5 neurons), which is set to 1(true)/0(false) by the MC information in the training samples.

For the 3-prong events, only a_1 is the discriminating decay mode. Input variables (a), (b), (c), (d), (f), (g), (h) (noted with (a')-(h') in Fig. 4) in the 1-prong selection are also included in the 3-prong selection. There is one additional variable, which is:

- Invariant mass of all charged particles. This should equals to the mass of a_1 if the decay is a_1 mode. (Variable (j').)

We use two hidden layers with 16 and 5 neurons. The only output neuron stands for likelihood value of a_1 mode, set to 1/0 in the training samples as well.

For the training, half of the tau-pair events in the mass production are used. Number of epochs is 1000 for both 1-prong and 3-prong network.

Fig. 3 and 4 shows distributions of the input variables, and Fig. 5 shows distribution of the output neurons. The mode selection is applied based on the values of the output neurons, as follows.

- If one or more of the values of the output neurons exceed 0.5, The neurons which gives the highest output value is used as the selection.

- If no output values exceed 0.5, the event is classified as 'others'.

Table 2 shows the obtained efficiency and purity for the mode selection. These values are obtained with the half of the tau-pair events which are not used for the training. $\gtrsim 90\%$ efficiency and purity is obtained for all decay modes except 1-prong a_1 decay.

7 Polarization Measurement

7.a Optimal Observable

To identify tau polarization, optimal observables[4] are used for $e^+\overline{\nu_e}\nu_\tau$, $\mu^+\overline{\nu_\mu}\nu_\tau$, $\pi^+\nu_\tau$ and $\rho^+\nu_\tau$ decay modes. Decay distribution of all tau decay can be described as the same form,

$$W = \frac{1}{2}(1 + p\cos\theta_h) \tag{7.32}$$

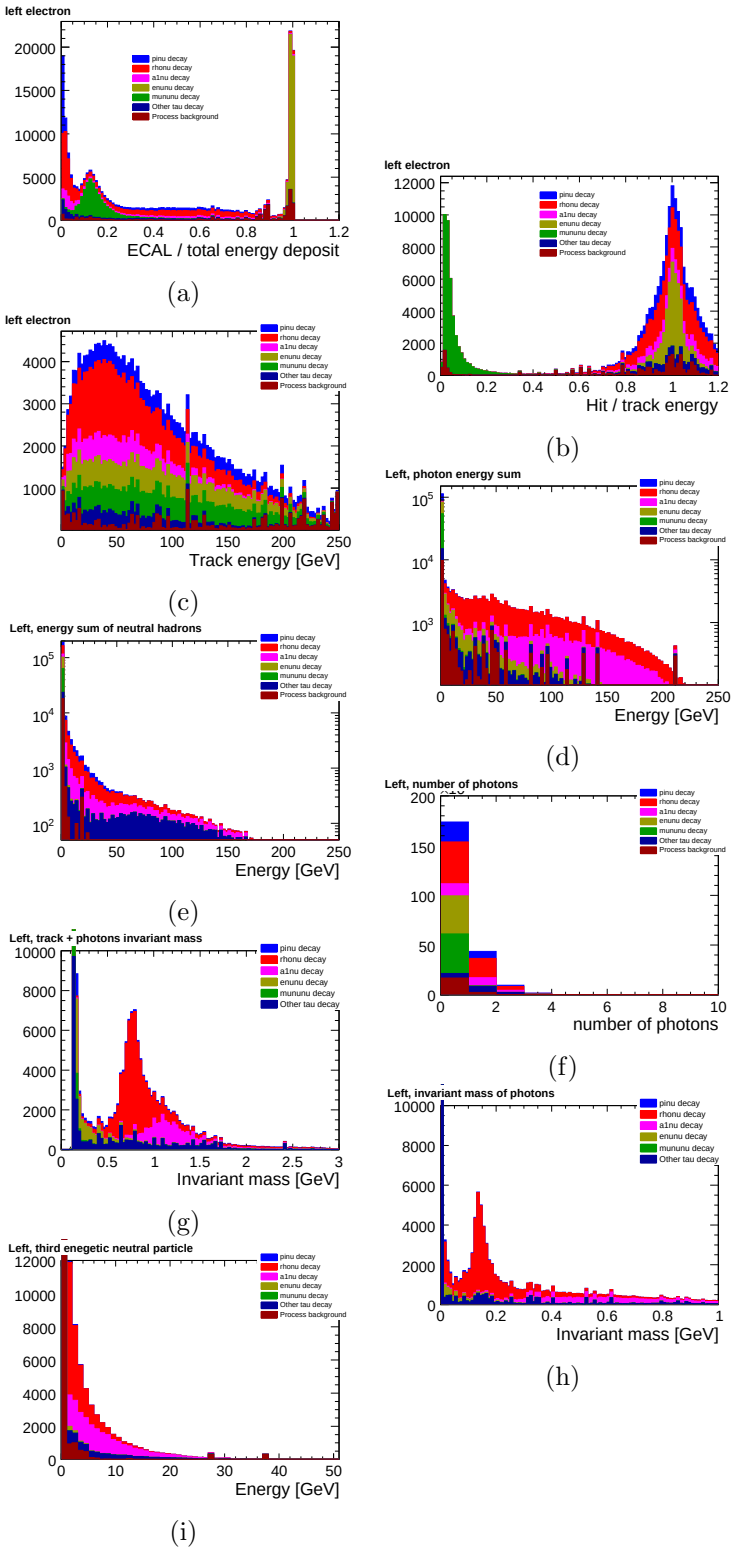

Figure 3: Distributions of the input variables for the 1-prong neural network. e_L^- (80%) e_R^+ polarization is used for the plots.

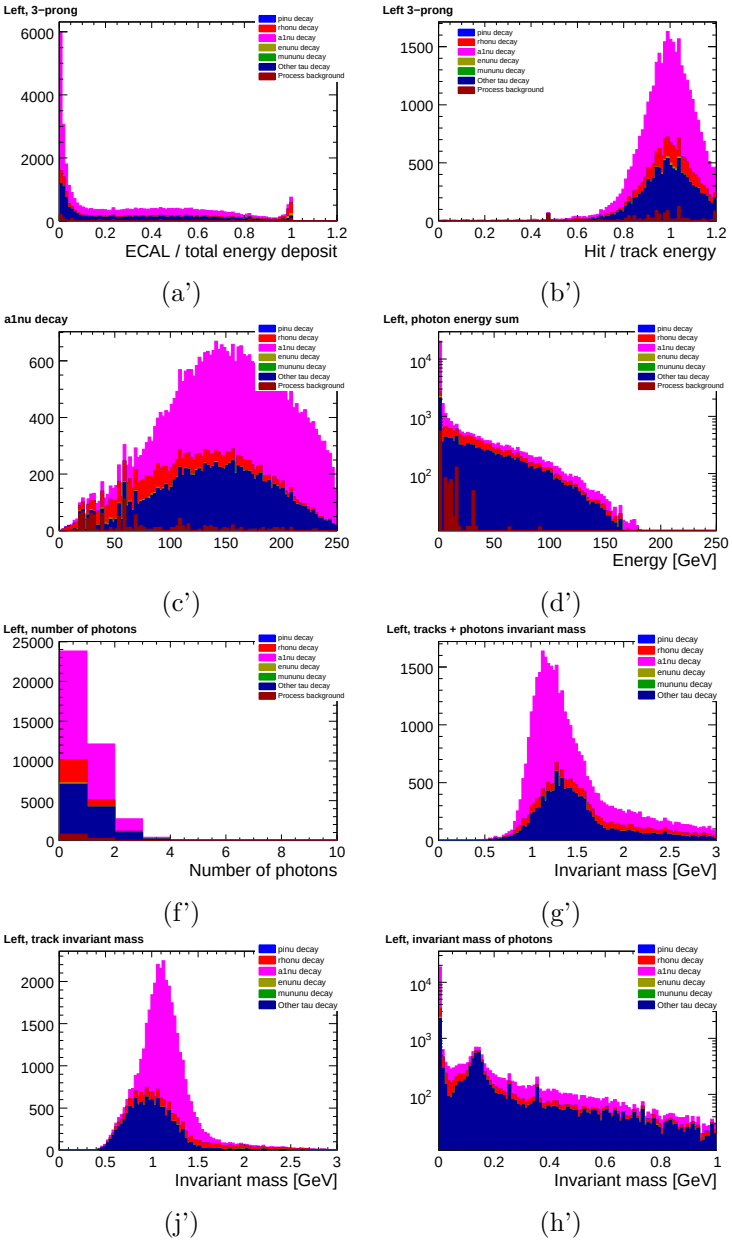

Figure 4: Distributions of the input variables for the 3-prong neural network. e_L^- (80%) e_R^+ polarization is used for the plots.

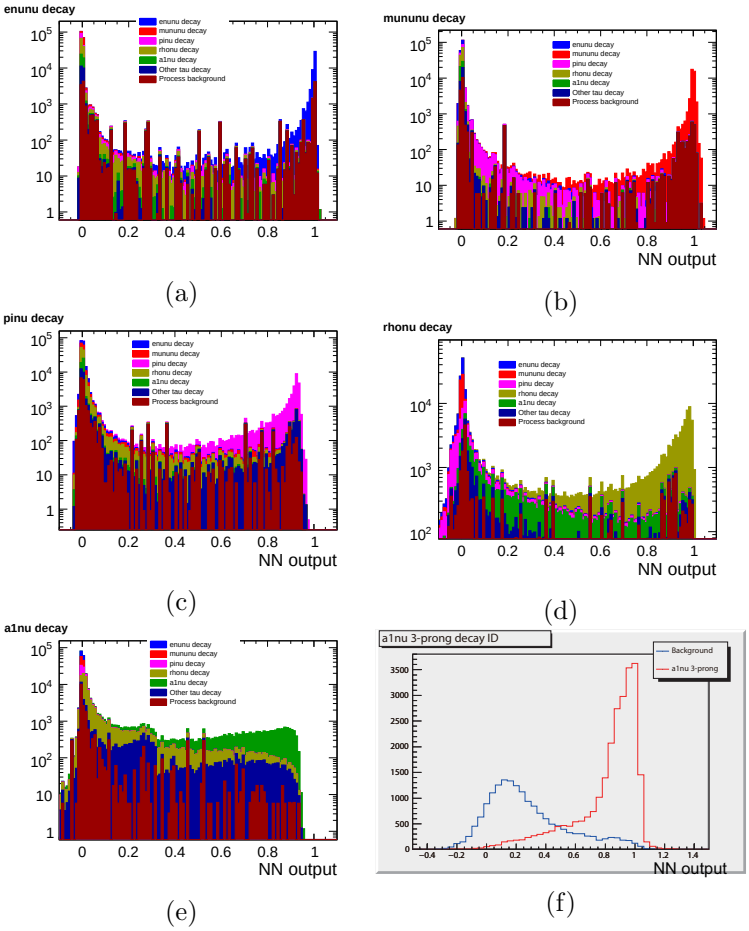

Figure 5: Output variables for the neural net selection. (a)-(e) are the output of the 1-prong neural net for $e^+\overline{\nu_e}\nu_\tau$, $\mu^+\overline{\nu_\mu}\nu_\tau$, $\pi^+\nu_\tau$, $\rho^+\nu_\tau$ and $a_1^+\nu_\tau$ modes, respectively. (f) is the output of the 3-prong neural net for $a_1^+\nu_\tau$ identification. e_L^- (80%) e_R^+ polarization is used for the plots.

Modes	Purity	Efficiency
$e\nu\nu$	98.9%	98.9%
$\mu\nu\nu$	98.8%	99.3%
$\pi\nu$	96.0%	89.5%
$\rho\nu$	91.6%	88.6%
$a_1\nu$ (1-prong)	67.2%	73.4%
$a_1\nu$ (3-prong)	91.1%	88.9%

Table 2: Purity and efficiency of the tau decay mode selection with neural networks. Process background is not included in the purity & efficiency numbers.

where p is polarization of τ (-1 to 1) and θ_h is the opening angle of polarimator vector $\vec{h}$ with respect to the τ momentum vector. Explicit notation of $\vec{h}$ varies by the decay modes: for pure-leptonic decay, flight direction of antineutrino is $\vec{h}$ and for $\pi^+\nu_\tau$ decay, flight direction of pion is $\vec{h}$. For the multipion decay, $\vec{h}$ is constructed from the hadronic current.

To reconstruct p from a set of observables, we split W to p-dependent and p-independent components such as

$$W(\vec{\xi}) = f(\vec{\xi}) + pg(\vec{\xi}), \tag{7.33}$$

and the optimal observable ω is defined as

$$\omega = \frac{g(\vec{\xi})}{f(\vec{\xi})}. \tag{7.34}$$

By definition, probability density P at ω for the polarization p gives

$$\frac{P(\omega;p) - P(\omega;p=0)}{P(\omega;p=0)} = \omega \tag{7.35}$$

and p can be easily obtained from the ω distribution.

The explicit formula of ω for each decay mode is as follows[5].

1. Pure-leptonic decay:
$$\omega_\ell = \frac{1 + x - 8x^2}{5 + 5x - 4x^2} \tag{7.36}$$
where x is the lepton energy divided by τ energy (250 GeV in this case). Since the pure-leptonic decay mode has two missing neutrinos, polarization discrimination power is weaker than semi-leptonic decay modes.

2. $\pi^+\nu_\tau$ decay:
$$\omega_\pi = 2x - 1. \tag{7.37}$$
This mode has maximum polarization discrimination power since $\vec{h}$ can be fully reconstructed.

3. $\rho^+\nu_\tau$ decay: This decay mode has multiple observable particles and thus more complicated formula to describe ω. Tau momentum direction is unobservable in this decay, so it is integrated out in the ω formulation. The explicit formula is:
$$\omega_\rho = \frac{\left(-1+\frac{m_\tau^2}{Q^2}+2\left(1+\frac{m_\tau^2}{Q^2}\right)\frac{3\cos^2\psi-1}{2}\frac{3\cos^2\beta-1}{2}\right)\cos\theta + 3\sqrt{\frac{m_\tau^2}{Q^2}}\frac{3\cos^2\beta-1}{2}\sin 2\psi \sin\theta}{2+\frac{m_\tau^2}{Q^2}-2\left(1-\frac{m_\tau^2}{Q^2}\right)\frac{3\cos^2\psi-1}{2}\frac{3\cos^2\beta-1}{2}} \tag{7.38}$$
$$\cos\psi = \frac{x(m_\tau^2 + Q^2) - 2Q^2}{(m_\tau^2 - Q^2)\sqrt{x^2 - 4Q^2/s}} \tag{7.39}$$
$$x = 2\frac{E_h}{\sqrt{s}} \tag{7.40}$$
where E_h is the energy sum of ρ (which equals to the cluster energy), Q^2 is the invariant mass of the visible particles (should equals to $m_\rho = 0.77$ GeV but obtained from the event), $\sqrt{s}$ is the center-of-mass energy (500 GeV), θ is the angle of the ρ flight direction with repect to τ direction in τ-rest frame, and β is the angle of the charged pion flight direction with repect to ρ direction in ρ-rest frame.

7.b Polarization measurement

Figure 6 shows the ω distribution for each decay mode passing the neural net selection. For the leptonic mode, most of the events are concentrated on the $\omega \sim 0$ region, reflecting to the weak discrimination power. For the $\pi^+\nu_\tau$ and $\rho^+\nu_\tau$ modes, ω distribution is broadly distributed and large difference between left and right polarization can be seen.

Polarization p can be obtained by following procedure.

1. Mode and process background is eliminated from each bin of the ω histograms and statistical error of background remains included in the error of each bin.
2. Histograms from all decay modes are summed into one histogram.
3. The histogram with polarizing sample (polarization p) is divided by non-polarizing sample after normalizing both histograms.
4. Perform linear fit passing (0,1) to the divided histogram (one parameter fit). Obtained slope stands for p.

Figure 7 shows the combined ω distribution and Figure 8 shows the linear fits to obtain p value. Obtained p is $-63.82 \pm 0.66\%$ ($e^-_L e^+_R$, 80% and 30%) and $50.83 \pm 0.79\%$ ($e^-_R e^+_L$, 80% and 30%).

8 Summary

Tau-pair process has been analysed in the ILD_00 detector model. After the tau selection cuts, statistical error of cross section measurement is 0.29% ($e^-_L e^+_R$, with 80% and 30% polarization, respectively) and 0.32% ($e^-_R e^+_L$). Process background can be suppressed to around 10% of signal events. Forward-backward asymmetry can be determined with 0.48% and 0.63% statistical error.

Polarization measurement needs separation of decay modes. The neural net selection gives $> 91\%$ efficiency and $> 88\%$ purity of mode selection for all major decay modes except $a_1\nu$ 1 prong mode. Polarization analysis of $e^+\overline{\nu_e}\nu_\tau$, $\mu^+\overline{\nu_\mu}\nu_\tau$, $\pi^+\nu_\tau$ and $\rho^+\nu_\tau$ decay mode is performed using the optimal observable method, and it results in $P(\tau) = -63.82 \pm 0.66\%$ ($e^-_L e^+_R$) and $P(\tau) = 50.83 \pm 0.79\%$ ($e^-_L e^+_R$).

The $a_1\nu_\tau$ mode is not included in the current polarization measurement. For the 3-prong a_1 decay, τ direction can be reconstructed from the vertex information and it can improve the analysis power to the same level as $\pi^+\nu_\tau$ mode. However, since the branching ratio of 3-prong a_1 decay is only about 9%, the expected improvement with 3-prong a_1 decay is about 20%.

References

[1] The WWOC Software panel: T. Behnke, N. Graf and A. Miyamoto, ILC-MEMO-2008-001.

[2] `http://ilcsoft/desy.de/portal/data_samples`

[3] S. Jadach, Z. Ws, R. Decker, JH. Kuehn, Comp. Phys. Comm. **76** 361 (1993).

[4] M. Davier, L. Duflot, F. Le Diberder and A. Rouge, Phys. Lett. B. **306** 411 (1993).

[5] L. Duflot, PhD. thesis, Paris-Sud 11 University in Orsay, 1993.

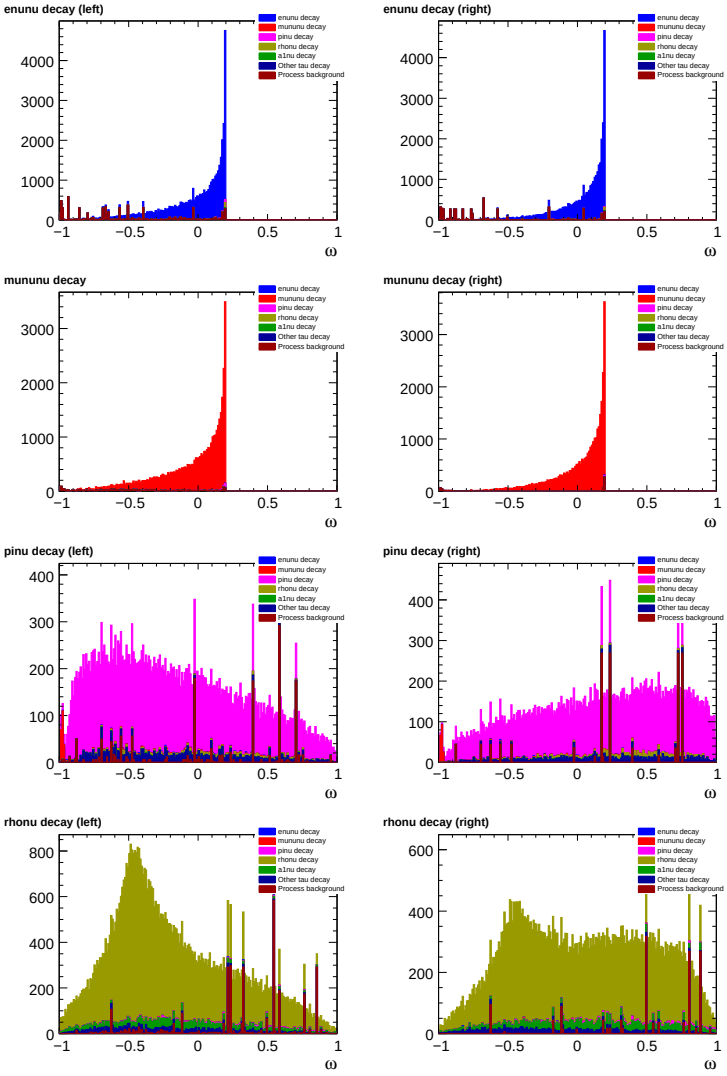

Figure 6: Distribution of the optimal observable for each decay mode. The left column shows distribution of e_L^- (80%) e_R^+ (30%) events, and the right column shows distribution of e_R^- (80%) e_L^+ (30%) events.

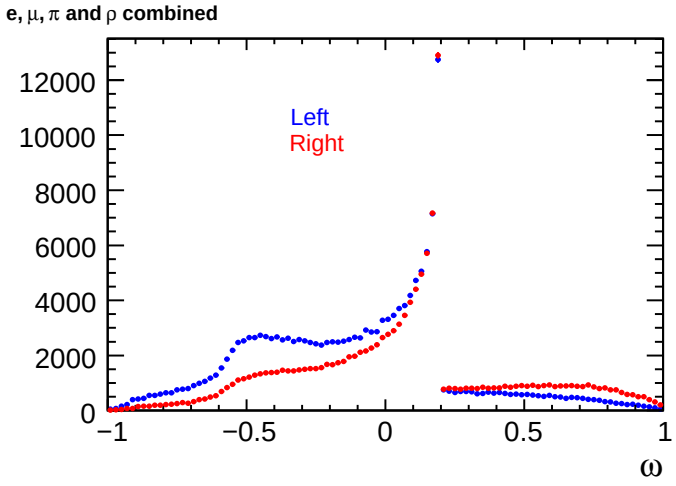

Figure 7: Distribution of the optimal observable after summing up all decay modes.

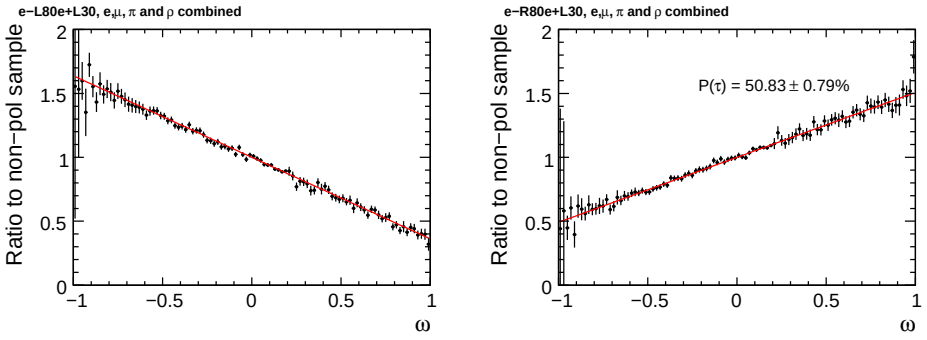

Figure 8: Ratio of the polarizing sample to the non-polarizing sample. Linear fit is applied to obtain p value.

DESY 09-099 ISSN 0418-9833

June 2009

Chargino and Neutralino Separation with the ILD Experiment

Taikan Suehara[(a)] and **Jenny List**[(b)]

[(a)] *International Center for Elementary Particle Physics The University of Tokyo, Hongo 7-3-1, Bunkyo District, Tokyo 113-0033, Japan*
[(b)] *Deutsches Elektronen-Synchrotron (DESY), Notkestr. 85, D-22607 Hamburg, Germany*

One of the benchmark processes for the optimisation of the detector concepts proposed for the International Linear Collider is Chargino and Neutralino pair production in an mSugra scenario where $\tilde{\chi}_1^\pm$ and $\tilde{\chi}_2^0$ are mass degenerate and decay into $W^\pm\tilde{\chi}_1^0$ and $Z^0\tilde{\chi}_1^0$, respectively. In this case the separation of both processes in the fully hadronic decay mode is very sensitive to the jet energy resolution and thus to the particle flow performance. The mass resolutions and cross-section uncertainties achievable with the ILD detector concept are studied in full simulation at a center of mass energy of 500 GeV, an integrated luminosity of 500 fb^{-1} and beam polarisations of $P(e^+, e^-) = (30\%, -80\%)$. For the $\tilde{\chi}_1^\pm$ and $\tilde{\chi}_2^0$ pair production cross-sections, statistical precisions of 0.84% and 2.75% are achieved, respectively. The masses of $\tilde{\chi}_1^\pm$, $\tilde{\chi}_2^0$ and $\tilde{\chi}_1^0$ can be determined with a statistical precision of 2.9 GeV, 1.7 GeV and 1.0 GeV, respectively.

1 Introduction

In anticipation of the International Linear Collider (ILC), a proposed e^+e^- collider with center-of-mass energies between 90 and 500 GeV, upgradable to 1 TeV, and polarised beams, several detector concepts are being discussed. In order to evaluate the performance of these concepts, benchmark processes have been chosen which are challenging for key aspects of the detector designs [1].

In order to test the jet energy resolution, a supersymmetric scenario which assumes non-universal soft SUSY-breaking contributions to the Higgs masses has been defined. In this scenario, the mass differences between the lightest SUSY particle (LSP) and the heavier gauginos become large, while at the same time the sleptons are so heavy that gaugino decays into sleptons are kinematically forbidden. The corresponding benchmark point has been defined in [1] as "Point 5" with the following SUSY parameters:

$$m_0 = 206 \text{ GeV}, \quad m_{1/2} = 293 \text{ GeV}, \quad \tan\beta = 10, \quad A = 0, \quad \mu = 375 \text{ GeV} \tag{1.41}$$

With a top quark mass of $M_t = 178$ GeV, the following gaugino masses are obtained by Spheno [2]:

$$M_{\tilde{\chi}_1^0} = 115.7 \text{ GeV}, \quad M_{\tilde{\chi}_1^\pm} = 216.5 \text{ GeV}, \quad M_{\tilde{\chi}_2^0} = 216.7 \text{ GeV}, \quad M_{\tilde{\chi}_3^0} = 380 \text{ GeV}. \quad (1.42)$$

The lightest sleptons are even heavier than the gauginos, thus leading to branching fractions of 99.4% for the decay $\tilde{\chi}_1^\pm \to W^\pm \tilde{\chi}_1^0$ and 96.4% for $\tilde{\chi}_2^0 \to Z^0 \tilde{\chi}_1^0$:

$$M_{\tilde{\tau}_1} = 230.8 \text{ GeV} \qquad M_{\tilde{e}_R} = 237.4 \text{ GeV} \quad (1.43)$$

In order to benchmark the jet energy reconstruction, the fully hadronic decay mode of the gauge bosons is considered here. In this mode, Chargino and Neutralino events can only be separated via the mass of the vector bosons they decay into. The motivation of this study is not to evaluate the final precision which could be achieved at the ILC by combining several final states, or even by performing threshold scans, but to test the detector performance in the most challenging decay mode.

The analysis is performed at a center of mass energy of 500 GeV for an integrated luminosity of 500 fb^{-1} with beam polarisations of $P(e^+, e^-) = (30\%, -80\%)$. It is based on a detailed simulation of the ILD detector based on GEANT4 [3], which is described briefly in the next section. Section 3 discusses the event reconstruction and selection procedure, including a pure Standard Model control selection. The results for the cross-section and mass measurement are presented in sections 4 and 5, respectively.

2 The ILD Detector Concept and its Simulation

The proposed ILD detector has been described in detail in the ILD Letter of Intent [4]. Its main characteristics comprise a time projection chamber as a main tracking device, which is complemented by silicon tracking and vertexing detectors, and highly granular electromagnetic and hadronic calorimeters as required for the particle flow approach [5]. Both, tracking system and calorimeters, are included in a solenoidal magnetic field with a strength of 3.5 T provided by a superconducting coil. The magnetic flux is returned in an iron yoke, which is instrumented for muon detection. Special calorimeters at low polar angles complement the hermeticity of the detector and provide luminosity measurement.

While previous studies were based on fast simulation programs which smear four-vectors with expected resolutions, we have used a full GEANT4 based simulation of all ILD components. Many details are included, in particular gaps in the sensitive regions and realistic estimates of dead material due to cables, mechanical support, cooling and so on.

With this detector simulation, the following performance has been achieved [4]: For tracks with a transverse momentum p_t larger than 1 GeV, the tracking efficiency is 99.5% across almost the entire polar angle range of $|\cos\theta| < 0.995$ covered by the tracking detectors, with a p_t resolution of better than $\sigma_{1/p_t} = 2 \times 10^{-5} \oplus 1 \times 10^{-3}/(p_t \sin\theta)$. The calorimetric system has been designed to deliver a jet energy resolution of 3.0% to 3.7% over a large range of energies from 250 GeV down to 45 GeV for polar angles θ in the range $|\cos\theta| < 0.9$. The luminosity is expected to be known to 10^{-3} from measurements of the Bhabha scattering cross-sections at small angles. The beam polarisations and the beam energies will be measured to $\delta P/P = 0.25\%$ and 2×10^{-4}, respectively by dedicated instrumentation in the beam delivery system.

The event sample used in this analysis has been generated using the matrix element generator Whizard [6]. It comprises all Standard Model processes plus all kinematically

accessible SUSY processes in the chosen scenario. In total, about 12×10^6 events have been generated and processed through the full simulation and reconstruction chain for this analysis.

3 Event Reconstruction and Selection

The reconstruction and also the first event selection steps are implemented in the MarlinReco framework [7]. The central part of the reconstruction for this analysis is the particle flow algorithm Pandora [5], which forms charged and neutral particle candidates - so-called "particle flow objects" or PFOs - from tracks and calorimeter clusters. The resulting list of PFOs for each event is forced into a 4–jet configuration using the Durham algorithm. The jet energy scale is raised by 1%, determined from dijet samples. No special treatment of b-quark jets is considered here.

As a final step of the reconstruction, a constrained kinematic fit [8], which requires the two dijet masses of the event to be equal, is performed on each event. All three possible jet pairings are tested. The resulting improvement in mass resolution is evaluated on Standard Model events, as described in section 3.b.

3.a SUSY Selection

The major part of the Standard Model events is rejected by applying the following selection to all events in the SUSY and SM samples:

- In order to eliminate pure leptonic events, the total number of tracks in the event should be larger than 20 and each jet has to contain at least two tracks.
- Since the two LSPs escape undetected, the visible energy of the event E_{vis} should be less than 300 GeV. In order to remove a substantial fraction of 2-photon events with very low visible energy, $E_{\mathrm{vis}} > 100$ GeV is required as well.
- To ensure a proper jet reconstruction, each jet should have a reconstructed energy of at least 5 GeV and a polar angle θ fulfilling $|\cos(\theta_{\mathrm{jet}})| < 0.99$.
- 2-jet events are rejected by requiring the distance parameter of the Durham jet algorithm for which the event flips from 4-jet to 3-jet configuration, y_{34} to be larger than 0.001.
- Coplanar events (e.g. W^+W^- with ISR/beamstrahlung photons) are removed by requiring $|\cos(\theta)|$ of the missing momentum to be smaller than 0.99.
- No lepton candidate with an energy larger than 25 GeV is allowed in order to suppress semi-leptonic events.

The upper part of table 1 shows the reduction for these cuts. The selection efficiency of hadronic Chargino and Neutralino pair events is very high, 88.1% and 90.8%, respectively. Therefore, we will refer to this stage in the selection process as "high efficiency" selection. Although the SM background is significantly reduced already by these cuts, the contribution from 4-fermion events is still large, about 6 times the Chargino signal.

Figure 1a) shows the reconstructed boson mass distribution as obtained by the constrained kinematic fit after these selection cuts. A large fraction of the remaining Standard

Model background features low invariant dijet masses, but nevertheless a sizable amount of background remains also in the signal region.

For the cross-section measurement, the sample is therefore cleaned further by four additional cuts:

- The number of particle flow objects (PFOs) in each jet should be $N_{\mathrm{PFO}} > 3$ in order to reject τ jets more effectively.
- The direction of the missing momentum should fulfill $|\cos\theta_{\mathrm{pmiss}}| < 0.8$: This cut is quite powerful to reject all kinds of SM backgrounds, which tend to peak in the forward region, while the signal follows a flat $\cos\theta_{\mathrm{pmiss}}$ distribution. Nevertheless, it reduces the signal efficiency substantially, which could be avoided for example by placing a more stringent cut on the missing mass instead (see next item). However, the missing mass distribution of the signal directly depends on the LSP mass, thus it should not be too finely tuned to specific mass values, since we want to measure the gaugino masses. The prediction of a flat $\cos\theta_{\mathrm{pmiss}}$ distribution depends only on the spin, and can thus be considered model-independent (within SUSY).
- The missing mass should be larger than 220 GeV to further reject 6-fermion events (semi-leptonic $t\bar{t}$). The value of this cut is chosen such that it is in a region with no SUSY contribution, i.e. where the data should agree with the SM expectation. Thus in a real experiment an adequate cut position could be found from the data. For this reason, no upper cut is placed on M_{miss}, since other SUSY processes contribute there, and it would not be trivial to determine a suitable cut value from real data.
- The kinematic fit constraining the two dijet masses to be equal should converge for at least one jet pairing: This is necessary in order to use the fit result for further analysis. The efficiency and resolution of the fit can be cross-checked easily on real data, for instance with the control selection decribed in the previous section.

The obtained reduction due to these cuts is shown in the last four lines of table 1. The final distribution of the reconstructed boson mass, again obtained by the constrained kinematic fit, is displayed in figure 1b. It illustrates the achieved boson mass resolution and thus W and Z pair separation, however at significantly reduced efficiency. Fitting the total spectrum by a fourth order polynomial for the background plus the sum of two Breit-Wigner functions folded with a Gaussian for the W and Z contributions, the mass resolutions can be determined to 3.4 %.

Table 2 shows the final purity and efficiency of signal and major background processes. According to this table, $e^+e^- \to qqqq$ is the dominant process in the remaining background.

3.b Standard Model Control Selection

Since the Chargino and Neutralino separation relies on reconstructing the masses of the W and Z bosons from their decay products, the dijet mass resolution is a crucial parameter in this analysis and has to be determined from Standard Model W and Z pair events. For this purpose, the "high efficiency" selection from above is applied to all simulated data, inverting only the cut on the visible energy to $E_{\mathrm{vis}} > 300$ GeV. This yields an event sample which is vastly dominated by 4-fermion events, with a small contribution from 6-fermion events, but no SUSY events. The corresponding dijet mass spectrum is shown in figure 2.

The mass resolution has been determined for two cases:

a) The jet pairing is chosen such that the difference between the two dijet masses in each event is minimized.

b) A kinematic fit, which constrains the two dijet masses in each event to be equal, is performed for all three possible jet-boson associations. The jet pairing which yields the highest fit probability is chosen.

The resulting mass distributions are fitted with the sum of two Breit-Wigner functions convoluted with a Gaussian, fixing the W and Z widths as well as the Z pole mass to their PDG values and having the same σ for both Gaussians, plus a forth order polynomial for all non-resonant contributions.

Figure 3 shows the fitted spectra and the resulting fit parameters. In case a), without the kinematic fit, the dijet mass resolution is determined as $\sigma_m^a = 3.5$ GeV, while it is reduced to $\sigma_m^b = 3.0$ GeV when the kinematic fit is applied.

These mass resolutions are even better than in the SUSY case, since the kinematics of the events is more favourable here. While the SM gauge boson pairs are highly boosted and thus finding the correct jet pairing is relatively easy, the bosons in our SUSY scenario are produced nearly at rest, resulting in a higher combinatorical background and a slightly worse boson mass resolution. Nevertheless, a SM control selection will be crucial to demonstrate the level of detector understanding, since the actual SUSY measurement will rely on template distributions and selection efficiencies determined from simulations.

4 Cross-Section Measurement

The cross-sections of $e^+e^- \to \tilde{\chi}_1^+\tilde{\chi}_1^-$ and $e^+e^- \to \tilde{\chi}_2^0\tilde{\chi}_2^0$ can be measured by determining the amount of W and Z pair like events. For the hadronic events we are concerned with here, a 2-dimensional fit in the plane of the two dijet masses per event is performed to obtain the amount of W and Z pair candidates.

Figure 4 shows the dijet mass distributions without the kinematic fit. All three possible jet-boson associations are taken into account in the histograms. 4a shows the dijet mass distribution of all Standard Model and SUSY point5 events passing the selection cuts; 4b is the SM part of 4a; 4c and 4d are statistically independent template samples for $\tilde{\chi}_1^\pm$ and $\tilde{\chi}_2^0$, made by 500 fb^{-1}. Before the fitting, the SM contribution (4b) is subtracted from the distribution of all events (4a). SUSY contributions other than $\tilde{\chi}_1^\pm$ and $\tilde{\chi}_2^0$ pair are not corrected for, but the contribution is negligibly small.

Figure 4e shows the result of a fit using a linear combination of the Chargino and Neutralino template distributions depicted 4c and d in. The residuals of the fit are displayed in figure 4f. They are sufficiently small and don't show any specific structures, indicating a well working fit.

While it can be assumed that the SM distribution is well known and can be controlled for instance with the SM selection above, the assumption that the shape of the Chargino and Neutralino spectra is known is not evident. However, the shape of the dijet mass distribution on generator level is quite independent of the details of the SUSY scenario, as long as the decay into real W and Z bosons is open. As discussed already in section 3.b, the shape of the reconstructed dijet mass distribution is influenced by the mass differences between $\tilde{\chi}_1^\pm$ / $\tilde{\chi}_2^0$ and the LSP, which determines the boost of the vector bosons and thus has an

effect on the amount of combinatorical background and the mass resolution. As shown in the next section, the masses of the gauginos can be measured purely from edge positions in the energy spectra of the gauge bosons, without any assumption on the cross-section. Thus, with the gaugino masses measured, we are confident that enough is known about the SUSY scenario at hand to apply the template method.

The background subtraction and the fit have been performed 10000 times, varying the bin contents of the SUSY and the SM distribution according to their statistical errors. The fitted fractions of Chargino and Neutralino contribution have been averaged over all fit outcomes, while the expected uncertainty is estimated from the variance of the fit results. Expressed in percent of the expected cross-section, this procedure yields $99.97 \pm 0.84\%$ for the Chargino and $97.50 \pm 2.75\%$ for the Neutralino case. In terms of absolute cross-sections this is equivalent to $\sigma(e^+e^- \to \tilde{\chi}_1^+\tilde{\chi}_1^-) = 124.80 \pm 1.05\text{fb}^{-1}$ (MC: 124.84 fb^{-1}), and $\sigma(\sigma(e^+e^- \to \tilde{\chi}_2^0\tilde{\chi}_2^0) = 21.90 \pm 0.62\text{fb}^{-1}$ (MC: 22.46 fb^{-1}).

If we use a best jet pairing rather than all combinations for the dijet mass, the statistical error grows by about 10%. This illustrates the fact that the true jet-boson association cannot always be found and that the jet pairings not classified as "best" still contain valuable information.

5 Mass Measurement

The masses of gauginos can be obtained via the energy spectrum of the W and Z boson candidates, since the distribution of gauginos is box-like with edges determined by the masses and the center-of-mass energy. Deviations from the pure box shape are due to the finite width of the W and Z bosons, the beam energy spectrum and the detector resolution. For the mass measurement, we have to separate the sample on an event-by-events basis into $\tilde{\chi}_1^\pm$ and $\tilde{\chi}_2^0$ pair candidates. This is done via the dijet masses, as described in the next subsection. Afterwards, the edge positions are fitted for both the Chargino and Neutralino selected sample. Finally, the actual masses are calculated from the edge positions.

5.a Dijet Selection

For each event, the jet pairing with the highest probability in the kinematic fit is chosen. An event is selected as a Chargino or Neutralino candidate using the following χ^2 variables, which are constructed from the invariant masses calculated from the four-vectors before the kinematic fit:

$$\chi^2_W(m_1, m_2) = \frac{(m_1 - m_W)^2 + (m_2 - m_W)^2}{\sigma^2} \tag{5.44}$$

$$\chi^2_Z(m_1, m_2) = \frac{(m_1 - m_Z)^2 + (m_2 - m_Z)^2}{\sigma^2}, \tag{5.45}$$

where m_1 and m_2 are dijet masses of selected jet-pairs, m_W and m_Z are the nominal W and Z pole masses and σ= 5 GeV. Events with $\chi^2_W < 4$ are classified as $\tilde{\chi}^\pm$, while events with $\chi^2_W > 4$ & $\chi^2_Z < 4$ are selected as $\tilde{\chi}^0_2$.

Figure 5a) shows the energy spectrum of the selected W candidates, while figure 5b) presents the same spectrum for the Z candidates. The edge positions can be seen in the spectra, although the four-fermion background is still large, especially in the Z energy distribution. The SM background can be fitted separately, as described below.

5.b Fitting the Edges

In the next step, the energy spectra of the W and Z candidates are fitted according to the following procedure.

1. First, the Standard Model contribution is fitted with the following function:

$$f_{SM}(x; t_0, a_{0-2}, \sigma, \Gamma) = \int_{t_0}^{\infty} (a_2 t^2 + a_1 t + a_0) V(t - x, \sigma, \Gamma) dt \tag{5.46}$$

   Here, x denotes the boson energy, and $V(x, \sigma, \Gamma)$ is the Voigt function, i.e. a Breit-Wigner function of width Γ convoluted with a Gaussian of resolution σ. The t_0 parameter adjusts the threshold position, while the parameters a_0, a_1 and a_2 are used to describe the shape of the plateau with a second order polynomial. The result of this fit is shown in figure 5.

2. Since the available statistics of the Standard Model sample is limited, the actual background used in the SUSY fit is generated from the fitted functions, including fluctuations according to the statistical errors expected from 500 fb^{-1} of integrated luminosity.

3. Finally, the sum of the SUSY spectra and the SM spectra generated in the previous step are fitted. The SUSY part of the fitting function is similar to the one used on the Standard Model, but this time also an upper edge position t_1 is introduced. Furthermore, the Gaussian resolution σ is allowed to have two different values at the edge positions, namely σ_0 and σ_1, with intermediate values obtained by linear interpolation.

$$f(x; t_{0-1}, b_{0-2}, \sigma_{0-1}, \Gamma) = f_{SM} + \int_{t_0}^{t_1} (b_2 t^2 + b_1 t + b_0) V(t - x, \sigma(t), \Gamma) dt \tag{5.47}$$

$$\sigma(t; \sigma_0, \sigma_1) = \sigma_0 + \frac{(\sigma_1 - \sigma_0)(t - 80)}{40}. \tag{5.48}$$

   All parameters of f_{SM} are fixed to the values obtained in the first step. For the $\tilde{\chi}_2^0$ fit, b_2 is also fixed to 0.

Figure 5 shows the results of the SM fit as well as the results of SUSY mass fit for both the Chargino and the Neutralino selection.

To obtain edge positions, the fit is performed 100 times with different Standard Model spectra generated from the SM fit function. As final result, the averaged edge position and error are given:

- $\tilde{\chi}_1^{\pm}$ lower edge: 79.88 ± 0.19 (MC: 79.80) GeV,
- $\tilde{\chi}_1^{\pm}$ upper edge: 131.49 ± 0.74 (MC: 132.77) GeV,
- $\tilde{\chi}_2^0$ lower edge: 92.34 ± 0.44 (MC: 93.09) GeV, and
- $\tilde{\chi}_2^0$ upper edge: 127.67 ± 0.76 (MC: 129.92) GeV.

There is a tendency that the fitted numbers are slightly smaller than MC numbers. Better jet energy correction or modification of the fitting function can reduce the shift, but principally the shift could be corrected with a dedicated MC study.

5.c Mass Determination from Edge Positions

The relation between the gaugino masses and the energy endpoints of the gauge bosons is determined by pure kinematics. Neglecting radiation losses, the energy of the gauginos is equal to the beam energy:$E_\chi = E_{\text{beam}}$. In the gaugino restsystem, denoted with *, the energy of the vector boson (i.e. W or Z) is given by the usual formula for two-body decays:

$$E_V^* = \frac{M_\chi^2 + M_V^2 - M_{\text{LSP}}^2}{2 \cdot M_\chi}, \tag{5.49}$$

where subscript χ denotes the decaying gaugino (i.e. $\tilde{\chi}_1^\pm$ or $\tilde{\chi}_2^0$), V the vector boson (i.e. W or Z) and the LSP $\tilde{\chi}_1^0$. Boosting this into the laboratory system yields:

$$E_V = \gamma E_V^* \pm \gamma\beta\sqrt{E_V^{*2} - M_V^2} \tag{5.50}$$

The Lorentz boost γ is given by $\gamma = E_\chi/M_\chi$, and $\beta = \sqrt{1 - 1/\gamma^2}$. The plus sign will give the upper edge of the allowed energy range, E_+, and the minus sign the lower one, E_-. For further calculations it is useful to introduce the center point of the allowed energy range, E_M, and its width E_D:

$$E_M = \frac{E_+ + E_-}{2}, \quad E_D = \frac{E_+ - E_-}{2} \tag{5.51}$$

In solving equation 5.50 for the gaugino masses, it is useful to note that $\gamma \cdot E_V^* = E_M$. With this relation, E_V^* can be eliminated and thus the LSP mass in obtained from E_D:

$$\begin{aligned} E_D &= \gamma\sqrt{1 - 1/\gamma^2}\sqrt{E_V^{*2} - M_V^2} && (5.52)\\ &= \sqrt{1 - 1/\gamma^2}\sqrt{\gamma^2 \cdot E_V^{*2} - \gamma^2 \cdot M_V^2} && (5.53)\\ &= \sqrt{1 - 1/\gamma^2}\sqrt{E_M^2 - \gamma^2 \cdot M_V^2} && (5.54) \end{aligned}$$

This is a quadratic equation in γ^2, which has two solutions:

$$\gamma^2 = \frac{1}{2 \cdot M_V^2}\left[(E_+ \cdot E_- + M_V^2) \pm \sqrt{(E_+^2 - M_V^2)(E_-^2 - M_V^2)}\right] \tag{5.55}$$

Inserting this into $\gamma \cdot E_V^* = E_M$, the LSP mass can be solved for:

$$M_{\text{LSP}}^2 = M_V^2 + \frac{E_{\text{beam}}^2}{\gamma^2}\left(1 - \frac{E_+ + E_-}{E_{\text{beam}}}\right) \tag{5.56}$$

For a single energy spectrum, we thus have two solutions in the general case. However with the constraint that the LSP mass has to be the same for both the Chargino and the Neutralino decay, a unique solution can be determined - in this case the one with the upper sign.

For the point5 SUSY parameters, the lower edge of the W energy spectrum is just equal to the W rest mass, meaning that the W bosons from the decay can be produced at rest, with the LSP carrying away all the momentum. This case has to be distinguished from

a configuration where the boost is so large that the W could actually fly into the same direction as the LSP in the laboratory frame. In this case, since the energy cannot become lower than the W rest mass, the lower part of the spectrum would be "folded over" and create a second falling edge above the W mass, precisely at $E_V = \sqrt{M_V^2 + p_{V,\min}^2}$, where $p_{V,\min} = -\gamma\beta E_V^* + \gamma\sqrt{E_V^{*2} - M_V^2}$. Moreover, this case of $E_- = M_W$ corresponds to the case where the equation for γ^2 has only one solution, with the $\pm$ term of equation 5.55 vanishing. At this point, the partial derivative $\partial E_-/\partial M_{\tilde{\chi}_1^\pm}$ becomes zero. So the inverse derivative which appears in the error propagation becomes undefined - or more realistically, with $E_- = M_W$ not exactly fulfilled, at least very large.

Since the discrimination between models is beyond the scope of this paper, but will be subject of future studies, we ignore here possible information from the lower edge of the W energy spectrum. Instead, the lower and upper edge of the Z energy spectrum are used to calculate the masses of $\tilde{\chi}_2^0$ and $\tilde{\chi}_1^0$. In a second step, the Chargino mass is calculated from the LSP mass and the upper edge of the W spectrum.

The error propagation is done by using a toy Monte Carlo, taking into account the correlations between the two masses determined from one energy spectrum. It calculates the gaugino masses by above equations with edge positions varying randomly according to their errors obtained from the edge fit. For the center edge positions two patterns were tried, the fitted edge positions and the MC truth positions.

Table 3 shows the obtained mass values and errors. Without correction of the edge position, the average value of obtained masses deviates by 3-4 GeV from the MC truth. This might be due to the fact that phase space was not considered, and could be reduced by an improved fitting function. with better fitting functions. Without the kinematic fit, the mass resolution is worse by typically 400 to 500 MeV, which corresponds to 15 to 40% of the errors, depending on the gaugino considered.

6 Summary

The physics performance of the ILD detector concept has been evaluated using a SUSY benchmark scenario referred to as "Point 5", where $\tilde{\chi}_1^\pm$ and $\tilde{\chi}_2^0$ are nearly mass degenerate and decay into real $W^\pm$ and Z^0 bosons, respectively, plus a $\tilde{\chi}_1^0$. The cross-sections for Chargino and Neutralino pair production have been obtained by a fit to the two-dimensional dijet mass spectrum relying on Monte-Carlo templates. The resulting statistical errors are 0.84% in the Chargino case and 2.75% in the Neutralino case.

The gaugino masses have been determined from a fit to the edges of the energy spectra of the $W^\pm$ and Z^0 bosons obtained by a kinematic fit. The resulting mass resolutions are 2.9 GeV, 1.7 GeV and 1.0 GeV for $\tilde{\chi}_1^\pm$, $\tilde{\chi}_2^0$ and $\tilde{\chi}_1^0$, respectively. Without the kinematic fit, the mass resolution is worse by 400 to 500 MeV.

Acknowledgements

We thank Frank Gaede, Steve Aplin, Jan Engels and Ivan Marchesini for simulating the event samples for this study, and we thank Timothy Barklow and Mikael Berggren for generating the corresponding four-vector files for SM backgrounds and SUSY, respectively. We further thank François Richard and Tohru Takeshita for the fruitful discussions about the

analysis. This work has been supported by the Emmy-Noether programme of the Deutsche Forschungsgemeinschaft (grant LI-1560/1-1).

References

[1] M. Battaglia *et al.*, "Physics benchmarks for the ILC detectors," *In the Proceedings of 2005 International Linear Collider Workshop (LCWS 2005), Stanford, California, 18-22 Mar 2005, pp 1602* [arXiv:hep-ex/0603010].

[2] W. Porod, "SPheno, a program for calculating supersymmetric spectra, SUSY particle decays and SUSY particle production at e^+e^- colliders," Comput. Phys. Commun. **153** (2003) 275 [arXiv:hep-ph/0301101].

[3] S. Agostinelli *et al.* [GEANT4 Collaboration], "GEANT4: A simulation toolkit," Nucl. Instrum. Meth. A **506** (2003) 250.

[4] ILD Concept Group, "The International Large Detector — Letter of Intent," DESY-09-087, http://www.ilcild.org/documents/ild-letter-of-intent

[5] M. A. Thomson, "Particle flow calorimetry at the ILC," AIP Conf. Proc. **896**, 215 (2007).

[6] W. Kilian, T. Ohl and J. Reuter, "WHIZARD: Simulating Multi-Particle Processes at LHC and ILC," arXiv:0708.4233 [hep-ph].

[7] O. Wendt, F. Gaede and T. Kramer, "Event reconstruction with MarlinReco at the ILC," Pramana **69** (2007) 1109 [arXiv:physics/0702171].

[8] B. List, J. List, "MarlinKinfit: An Object–Oriented Kinematic Fitting Package," LC-TOOL-2009-001, http://www-flc.desy.de/lcnotes/

	$\tilde{\chi}_1^+\tilde{\chi}_1^-$ → hadrons	$\tilde{\chi}_2^0\tilde{\chi}_2^0$ → hadrons	other SUSY	SM $\gamma\gamma$	SM 6f	SM 4f	SM 2f
nocut	28529	5488	74650	3.66e+09	521610	1.48e+07	2.14e+07
Total # of tracks ≥ 20	27897	5449	24305	3.03e+06	495605	6.68e+06	5.33e+06
$100 < E_{\rm vis} < 300$ GeV	27895	5449	22508	1.06e+06	44394	959805	1.56e+06
$E_{\rm jet} > 5$	27889	5446	20721	908492	44096	916507	1.47e+06
$\lvert\cos(\theta)_{\rm jets}\rvert < 0.99$	26560	5240	19200	350364	41098	678083	874907
$y_{34} > 0.001$	26416	5218	15255	202510	38638	423080	166305
# of tracks $\geq$ 2/jets	25717	5146	9559	162193	22740	255870	145270
$\lvert\cos\theta_{\rm miss}\rvert < 0.99$	25463	5099	9487	25087	22311	193706	4039
$E_{\rm l} < 25$	25123	4981	6463	23133	14407	154927	3534
$N_{\rm PFO} > 3$	25029	4975	6103	23014	13696	139429	3518
$\lvert\cos\theta_{\rm miss}\rvert < 0.8$	20144	4079	5180	681	9950	62668	529
$M_{\rm miss} > 220$ GeV	20139	4079	5180	630	3687	45867	389
kin. fit converged	20085	4068	4999	626	3649	44577	341

Table 1: Event numbers after each of the selection cuts, normalized to 500 fb^{-1} and $P(e^+, e^-) = (30\%, -80\%)$.

Processes	No cut	all cuts	Purity	Efficiency
$\tilde{\chi}_1^+\tilde{\chi}_1^-$ → hadrons	28529	16552	58%	58%
$\tilde{\chi}_2^0\tilde{\chi}_2^0$ → hadrons	5488	3607	13%	65%
Other SUSY point5	74650	77	0.27%	1.0×10^{-3}
qqqq (WW, ZZ)	4.29e+06	5885	21%	1.4×10^{-3}
qq$\ell\nu$ (WW)	5.19e+06	561	2.0%	1.1×10^{-4}
qqqq$\ell\nu$ (tt)	216996	489	1.7%	2.3×10^{-3}
$\gamma\gamma$ →qqqq	26356	397	1.4%	1.5%
qqqq$\nu\nu$ (WWZ)	9262	268	0.94%	2.9%
qq$\nu\nu$ (ZZ)	367779	76	0.27%	2.1×10^{-4}
qq	9.77e+06	76	0.27%	7.8×10^{-6}
Other background	3.68e+09	438	1.5%	1.2×10^{-7}

Table 2: Purity and efficiency of signal and major background sources after the selection cuts and with an invariant dijet mass larger than 65 GeV. The processes in pathentheses indicate the dominant intermediate states.

Observables	Obtained value	Error	Error at the true mass
$m(\tilde{\chi}_1^\pm)$	220.90 GeV	2.90 GeV	3.34 GeV
$m(\tilde{\chi}_2^0)$	220.56 GeV	1.72 GeV	1.39 GeV
$m(\tilde{\chi}_1^0)$	118.97 GeV	1.02 GeV	0.95 GeV

Table 3: Performance on gaugino masses and associated errors. The last column shows errors on masses when the true edge positions are used in the error propagation. MC truth masses are 216.7, 216.5 and 115.7 GeV for $\tilde{\chi}_1^\pm$, $\tilde{\chi}_2^0$ and $\tilde{\chi}_1^0$, respectively.

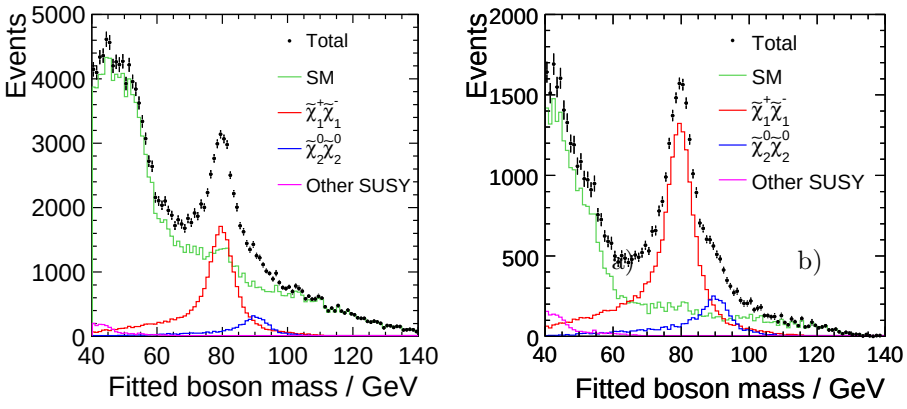

Figure 1: a) Reconstructed mass of the vector boson candidates after all selection cuts and kinematic fit for the jet pairing with the highest fit probability. b) Same distribution after some additional cuts to enhance the purity.

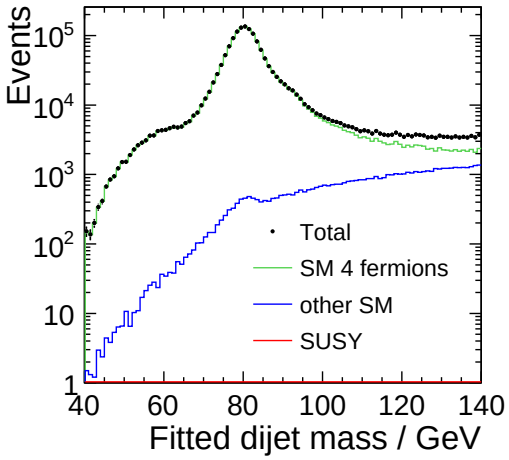

Figure 2: Dijet mass spectrum for Standard Model selection. The event sample is dominated by 4-fermion events, with a small contribution from 6-fermion events, but doesn't contain any SUSY events.

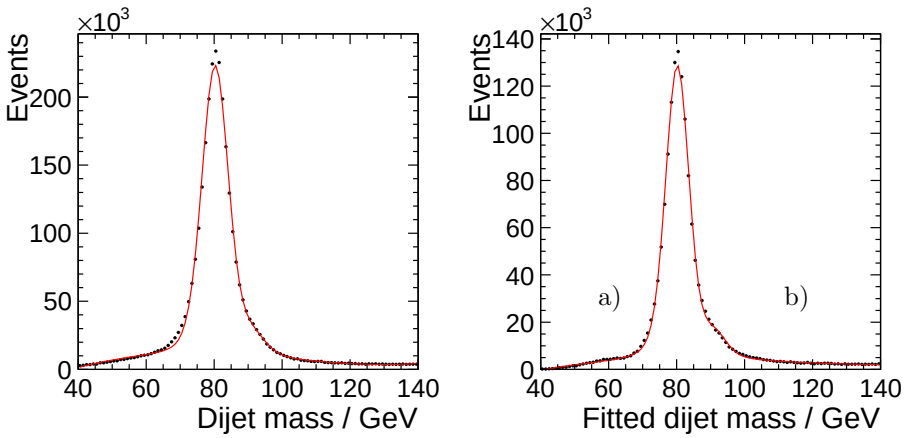

Figure 3: Dijet mass distributions a) without and b) with kinematic fit. Fitting the distributions with the sum of two Breit-Wigner functions folded with Gaussian plus a forth order polynomial for the non-resonant background yields dijet mass resolutions of 3.5 GeV (case a) and 3.0 GeV (case b).

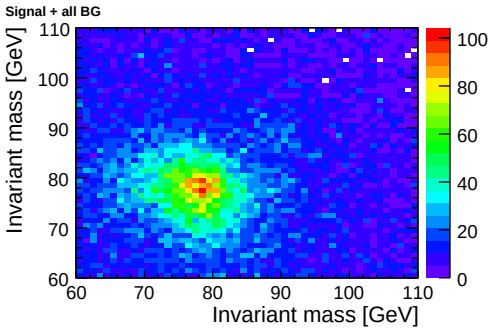

(a) All events (Sig + BG).

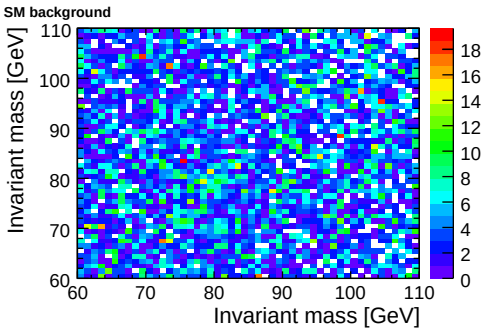

(b) SM background.

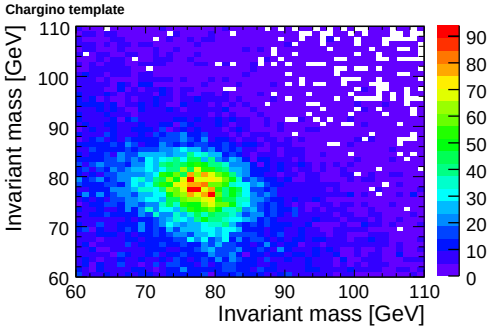

(c) Chargino-pair template (including all W decay mode).

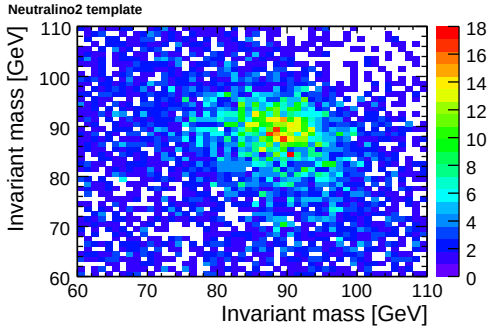

(d) Neutralino2-pair template (including all Z decay mode).

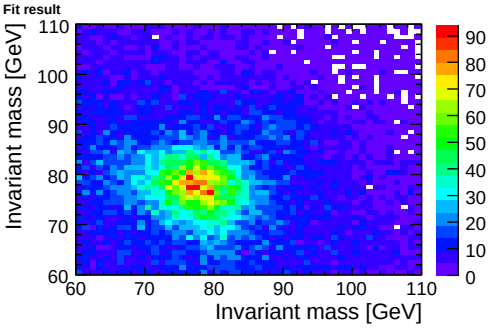

(e) Fit result to (a) - (b) with SM subtraction fluctuation.

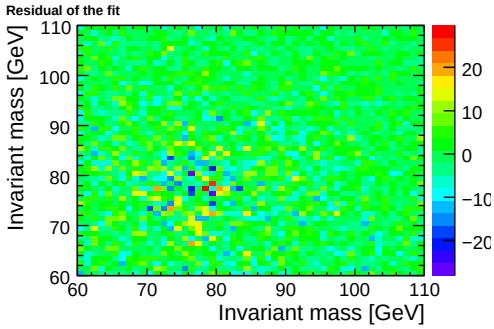

(f) Residual of the fit: (a) - (b) - (e).

Figure 4: Dijet mass distribution for cross-section fit. For (a) and (b) the same events are used, while (c) and (d) are statistically independent of (a).

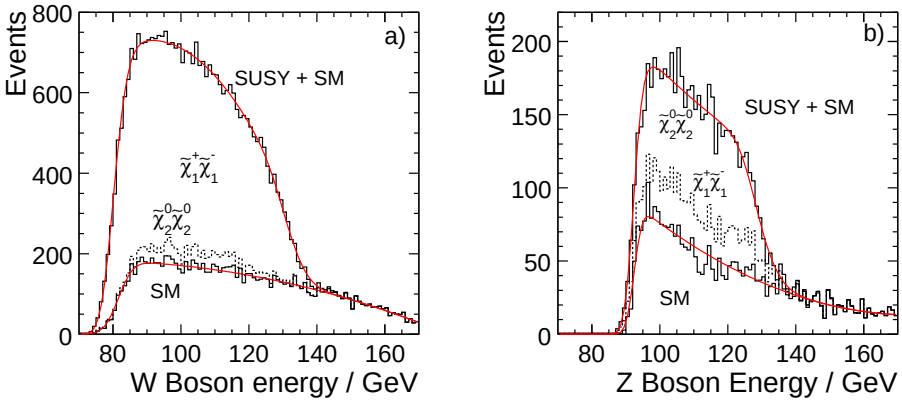

Figure 5: Mass determination: a) Energy spectrum of the $W^{\pm}$ candidates reconstructed from events selected as $\tilde{\chi}_1^{\pm}$ pairs and b) Energy spectrum of the Z^0 candidates reconstructed from events selected as $\tilde{\chi}_2^0$ pairs. In both cases, the Standard Model contribution has been fitted seperately before fitting the total spectrum.

Hidden particle production at the ILC

Hideo Itoh[(a)], **Katsumasa Ikematsu**[(a)], **Keisuke Fujii**[(a)], **Hitoshi Hano**[(a)], **Nobuchika Okada**[(a)], and **Tamaki Yoshioka**[(b)]

[(a)] *High Energy Accelerator Research Organization (KEK), Tsukuba, Japan*
[(b)] *The University of Tokyo, International Center for Elementary Particle Physics (ICEPP), Tokyo, Japan*

In a class of new physics models, new physics sector is completely or partly hidden, namely, singlet under the Standard Model (SM) gauge group. Hidden fields included in such new physics models communicate with the Standard Model sector through higher dimensional operators. If a cutoff lies in the TeV range, such hidden fields can be produced at future colliders. We consider a scalar filed as an example of the hidden fields. Collider phenomenology on this hidden scalar is similar to that of the SM Higgs boson, but there are several features quite different from those of the Higgs boson. We investigate productions of the hidden scalar at the International Linear Collider (ILC) and study the feasibility of its measurements, in particular, how well the ILC distinguishes the scalar from the Higgs boson, through realistic Monte Carlo simulations.

1 Introduction

In a class of new physics models, a new physics sector is completely or partly singlet under the Standard Model (SM) gauge group, $\mathrm{SU}(3)_C \times \mathrm{SU}(2)_L \times \mathrm{U}(1)_Y$. Such a new physics sector, which we call "hidden sector" throughout this paper, includes some singlet fields. These hidden sector fields, in general, couple with the SM fields through higher dimensional operators. If the cutoff scale of the higher dimensional operators lies around the TeV scale, effects of the hidden fields are accessible at future colliders such as the Large Hadron Collider (LHC) and the International Linear Collider (ILC).

There have been several new physics models proposed that include hidden fields. The most familiar example would be the Kaluza-Klein (KK) modes of graviton in extra dimension scenarios [1] [2]. A singlet chiral superfield in the next to Minimal Supersymmetric Standard Model (MSSM) [3] is also a well-known example, which has interesting implications, in particular, on Higgs phenomenology in collider physics [4]. Another example is the supersymmetry breaking sector of the model proposed in Ref. [5], where a singlet scalar field couples with the SM fields through higher dimensional operators with a cutoff around $\Lambda = 1 - 10$ TeV and its collider phenomenology at the LHC and ILC has been discussed. A very recently proposed scenario [6], "unparticle physics", belongs to this class of models, whose phenomenological aspects have been intensively studied by many authors.

In this paper, we introduce a hidden scalar field and investigate the hidden scalar production at the ILC. We assume that the hidden scalar couples with only the SM gauge fields through higher dimensional operators suppressed by a TeV-scale cutoff. In this case, at the ILC, this hidden scalar can be produced through the similar process to the SM Higgs boson

production and with the production cross sections comparable to the Higgs boson one. Thus, the hidden scalar production has interesting implications on the Higgs phenomenology. The crucial difference of the hidden scalar from the Higgs boson lies in that the hidden scalar has nothing to do with the electroweak symmetry breaking. This feature reflects the fact that the hidden scalar couples with mostly the transverse mode of the weak gauge bosons while the Higgs boson couples with mostly their longitudinal modes. Also, the branching ratio of the scalar is quite different from the Higgs boson one. Supposing the hidden scalar is found at the ILC, it is an interesting issue how to distinguish it from the Higgs boson and in this paper, we tackle this issue. Based on realistic Monte Carlo simulations, we study the feasibility of measurements for the hidden scalar productions and its couplings to the SM particles, and show how well the hidden scalar can be distinguished from the Higgs boson at the ILC.

This paper is organized as follows. In the next section, we introduce our theoretical framework and present formulas relevant to our studies. In Sec. 3, we show the results from our Monte Carlo simulations and demonstrate how accurately the ILC can measure the typical features of the scalar and distinguish it from the Higgs boson. The last section is devoted to summary and discussions.

2 Theoretical framework

In this paper, we introduce a real scalar field χ as a hidden field, which communicates with the SM sector through interactions of the form,

$$\mathcal{L}_{\rm int} = \frac{c_i}{\Lambda^{d_{\rm SM}-3}} \chi \, \mathcal{O}^i_{\rm SM}, \tag{2.57}$$

where c_i is a dimensionless coefficient, Λ is a cutoff scale, and $\mathcal{O}^i_{\rm SM}$ is an operator of the SM fields with mass dimension $d_{\rm SM}$. We consider the case that the cutoff, which is naturally characterized by a new physics scale, is around the TeV scale. As an example, it would be easy to imagine a model like the large extra-dimension models [1] whose fundamental scale is in the TeV range or a model with warped extra dimensions [2] where the effective cutoff scale is warped down to the TeV range from the 4-dimensional Planck scale. For a more concrete example, see Ref. [5]. In these models, the above effective interaction can be introduced at tree level.

The theoretical requirements for the SM operator $\mathcal{O}^i_{\rm SM}$ are that it should be a Lorentz scalar operator and be singlet under the SM gauge group. Although there are many possibilities for such operators, we assume that the hidden scalar couples with only the SM gauge bosons through the operators descried as follows*:

$$\mathcal{L}_{\rm int} = -\frac{1}{2} \sum_A \, c_A \, \frac{\chi}{\Lambda} \, {\rm tr} \left[\mathcal{F}^{\mu\nu}_A \mathcal{F}_{A\mu\nu} \right], \tag{2.58}$$

where c_A is a dimensionless parameter, and $\mathcal{F}_A$'s ($A = 1, 2, 3$) are the field strengths of the corresponding SM gauge groups, U(1)$_Y$, SU(2)$_L$, and SU(3)$_C$. After the electroweak symmetry breaking, Eq. (2.58) is rewritten as interactions between χ and gluons, photons,

*In fact, it is easy to construct a simple model which can realize this situation. We give comments on this respect in the last section.

Z- and W-bosons.

$$\begin{aligned}\mathcal{L}_{\rm int} = & - \frac{c_{gg}}{4}\frac{\chi}{\Lambda}G^{a\mu\nu}G^a_{\mu\nu} - \frac{c_{WW}}{2}\frac{\chi}{\Lambda}W^{+\mu\nu}W^-_{\mu\nu} - \frac{c_{ZZ}}{4}\frac{\chi}{\Lambda}Z^{\mu\nu}Z_{\mu\nu} \\ & - \frac{c_{\gamma\gamma}}{2}\frac{\chi}{\Lambda}F^{\mu\nu}F_{\mu\nu} - \frac{c_{Z\gamma}}{4}\frac{\chi}{\Lambda}Z^{\mu\nu}F_{\mu\nu},\end{aligned} \tag{2.59}$$

where $G^{a\mu\nu}$, $W^{+\mu\nu}$, $Z^{\mu\nu}$ and $F^{\mu\nu}$ are the field strengths of gluon, W-boson, Z-boson and photon, respectively. The couplings c_{gg} etc. can be described in terms of the original three couplings, c_1, c_2 and c_3, and the weak mixing angle θ_w as follows:

$$\begin{aligned} c_{gg} &= c_3, \\ c_{WW} &= c_2, \\ c_{ZZ} &= c_1 \sin^2\theta_w + c_2 \cos^2\theta_w, \\ c_{\gamma\gamma} &= c_1 \cos^2\theta_w + c_2 \sin^2\theta_w, \\ c_{Z\gamma} &= (-c_1 + c_2)\sin\theta_w \cos\theta_w. \end{aligned} \tag{2.60}$$

The hidden scalar can be produced at the ILC through these interactions. The dominant χ production process is the associated production, $e^+e^- \to \gamma^*, Z^* \to Z\chi$ and $e^+e^- \to \gamma^*, Z^* \to \gamma\chi$. First, let us consider the process $e^+e^- \to Z\chi$. The cross section is calculated as

$$\begin{aligned}\frac{d\sigma}{d\cos\theta}(e^+e^- \to Z\chi) &= \frac{1}{68\pi s}\sqrt{\frac{E_Z^2 - m_Z^2}{s}} \\ \times & \left[\left(c_{ZZ}^2(g_L^2+g_R^2)\left(\frac{s}{s-m_Z^2}\right)^2 - c_{ZZ}c_{Z\gamma}(g_L+g_R)e\left(\frac{s}{s-m_Z^2}\right) + c_{Z\gamma}^2 e^2\right)\frac{E_Z^2}{\Lambda^2}(1+\cos^2\theta)\right. \\ + & \left.\left(c_{ZZ}^2(g_L^2+g_R^2)\left(\frac{s}{s-m_Z^2}\right)^2 - \sqrt{2}c_{ZZ}c_{Z\gamma}(g_L+g_R)e\left(\frac{s}{s-m_Z^2}\right) + \frac{c_{Z\gamma}^2 e^2}{2}\right)\frac{m_Z^2}{\Lambda^2}\sin^2\theta\right]\end{aligned} \tag{2.61}$$

where $\cos\theta$ is the scattering angle of the final state Z-boson, $g_L = 2(m_Z/v)(-1/2+\sin^2\theta_w)$, $g_R = 2(m_Z/v)\sin^2\theta_w$, and $E_Z = \frac{\sqrt{s}}{2}\left(1 + \frac{m_Z^2 - m_\chi^2}{s}\right)$. It is interesting to compare this χ production process to the similar process of the associated Higgs production (Higgsstrahlung), $e^+e^- \to Zh$, through the Standard Model interaction $\mathcal{L}_{\rm int} = \frac{m_Z^2}{v}hZ^\mu Z_\mu$. In Figure 1, we show the ratio of the total cross sections between χ and Higgs boson productions as a function of Λ at the ILC with the collider energy $\sqrt{s} = 500$ GeV. Here we have taken $c_1 = c_2$ and $m_\chi = m_h = 120$ GeV. The ratio, $\sigma(e^+e^- \to Z\chi)/\sigma(e^+e^- \to Zh)$, becomes one for $\Lambda_{\rm IR} \simeq 872$ GeV, and it decreases proportionally to $1/\Lambda^2$. Note that in the high energy limit, the χ production cross section becomes energy-independent.

The coupling manner among χ and the Z-boson pair is different from that of the Higgs boson. As can be understood from Eq. (2.59), χ couples with the transverse modes of the Z-bosons, while the Higgs boson mainly couples with the longitudinal modes. This fact reflects into the difference of the angular distribution of the final state Z-boson. In the high energy limit, we find $\frac{d\sigma}{d\cos\theta}(e^+e^- \to Z\chi) \propto 1+\cos^2\theta$, while $\frac{d\sigma}{d\cos\theta}(e^+e^- \to Zh) \propto 1-\cos^2\theta$. Figure 2 shows the angular distributions of the associated χ and Higgs boson productions, respectively. Even if $m_\chi = m_h$ and the cross sections of χ and Higgs boson productions are

comparable, the angular dependence of the cross section can distinguish the χ production from the Higgs boson one.

The formula for the process $e^+e^- \to \gamma^*, Z^* \to \gamma\chi$ can be easily obtained from Eq. (2.61) for Z-boson by the replacements: $c_{ZZ} \to c_{Z\gamma}$, $c_{Z\gamma} \to c_{\gamma\gamma}$ and $m_Z \to 0$. As a result, the cross section of the process $e^+e^- \to \gamma\chi$ is found to be

$$\frac{d\sigma}{d\cos\theta}(e^+e^- \to \gamma\chi) = \frac{1}{128\pi s}\sqrt{\frac{E_\gamma^2 - m_Z^2}{s}} \times \left(c_{Z\gamma}^2(g_L^2+g_R^2)\left(\frac{s}{s-m_Z^2}\right)^2 - c_{Z\gamma}c_{\gamma\gamma}(g_L+g_R)e\left(\frac{s}{s-m_Z^2}\right) + c_{\gamma\gamma}^2 e^2 \right) \frac{E_\gamma^2}{\Lambda_{\rm IR}^2}(1+\cos^2\theta), \tag{2.62}$$

where $E_\gamma = \frac{\sqrt{s}}{2}\left(1 - \frac{m_\chi^2}{s}\right)$. For example, $\sigma(e^+e^- \to \gamma\chi) = 105$ fb at $\sqrt{s} = 500$ GeV with the parameter set: $m_\chi = 120$ GeV, $c_1 = c_2 = 1$ and $\Lambda = 1$ TeV. For the Higgs production, the process $e^+e^- \to \gamma^* \to \gamma h$ is negligible.

Next, we consider χ decay processes into a pair of gauge bosons. Partial decay widths are given by

$$\begin{aligned}
\Gamma(\chi \to gg) &= \frac{c_{gg}^2}{8\pi}\frac{m_\chi^3}{\Lambda^2}, \\
\Gamma(\chi \to \gamma\gamma) &= \frac{c_{\gamma\gamma}^2}{64\pi}\frac{m_\chi^3}{\Lambda^2}, \\
\Gamma(\chi \to ZZ) &= \frac{c_{ZZ}^2}{512\pi}\frac{m_\chi^3}{\Lambda^2}\,\beta_Z\left(3+2\beta_Z^2+3\beta_Z^4\right), \\
\Gamma(\chi \to WW) &= \frac{c_{WW}^2}{256\pi}\frac{m_\chi^3}{\Lambda^2}\,\beta_W\left(3+2\beta_W^2+3\beta_W^4\right), \\
\Gamma(\chi \to \gamma Z) &= \frac{c_{Z\gamma}^2}{128\pi}\tan^2(2\theta_w)\frac{m_\chi^3}{\Lambda^2}\left(1-\frac{m_Z^2}{m_\chi^2}\right)^3,
\end{aligned} \tag{2.63}$$

where $\beta_Z = \sqrt{1-4(m_Z/m_\chi)^2}$, and $\beta_W = \sqrt{1-4(m_W/m_\chi)^2}$. In Figure 3. the branching ratio of the χ decay is depicted. We see that the branching ratio of the χ decay is quite different from that of the Higgs boson. In particular, the branching ratio of $\chi \to \gamma\gamma$ can be large, $\mathrm{Br}(\chi \to \gamma\gamma) \simeq 0.1$ for the parameter set in Figure 3. On the other hand, the branching ratio of the Higgs boson into two photons in the SM is at most 10^{-3}, since the coupling between the Higgs boson and two photons are induced through one-loop radiative corrections.

There are several models where the branching ratio of the Higgs boson into two photons is enhanced due to new physics effects. For example, in the MSSM with a large $\tan\beta$ [7], the lightest Higgs boson almost coincides with the up-type Higgs boson of the weak eigenstate. As a result, the Yukawa coupling to bottom quark is suppressed and two-photon branching ratio is relatively enhanced. Another example is the Next to MSSM (NMSSM), where a pseudo scalar (A^0) couples to the lightest (SM-like) Higgs boson. In this model, the Higgs boson can decay into two pseudo scalars ($h \to A^0A^0$) with a sizable branching ratio. If the pseudo scalar is extremely light (lighter than twice the pion mass), it dominantly decays into two photons ($A^0 \to \gamma\gamma$), so that Higgs boson decays into four photons. Since the pseudo-scalar is very light, two photons produced in its decay are almost collinear and will

be detected as a single photon [4]. As a result, the Higgs decay into two pseudo-scalars, followed by $A^0 \to \gamma\gamma$, effectively enhances the Higgs branching ratio into two photons [4]. Therefore, the anomalous branching ratio alone is not enough to distinguish such a Higgs boson from χ (in the associated production with a Z-boson) and the measurements of angular distribution and polarization of the final state Z-boson are crucial.

Here, let us consider current experimental constraints on the parameters in our framework. Since the hidden scalar χ has the properties similar to the Higgs boson, we can use the current experimental limits of the Higgs boson search to constrain model parameters. The most severe constraint is provided by the Higgs boson search in the two-photon decay mode at Tevatron with the integrated luminosity 1 fb^{-1}, which is found to be $\sigma_h \mathrm{Br}(h \to \gamma\gamma) \lesssim 0.1$ pb for a light Higgs boson with a mass around 120 GeV [8]. Here, σ_h is the Higgs boson production cross section at Tevatron, which is dominated by the gluon fusion process. The Standard Model predicts $\sigma_h \mathrm{Br}(h \to \gamma\gamma) \sim 10^{-3}$ pb, far below the bound. However, when this bound is applied to the χ production with $\Lambda \simeq 1$ TeV, we obtain a severe constraint on the model parameters. Comparing the couplings between gluons and χ to the one between gluons and the Higgs boson in the SM, we find the ratio of the production cross sections at Tevatron as $\sigma_\chi/\sigma_h \sim 100 c_{gg}^2$. For $m_\chi = 120$ GeV, for example, the main decay mode of the χ will be into two gluons and photons, and the branching ratio into two photons is estimated as $\mathrm{Br}(\chi \to \gamma\gamma) \simeq (c_{\gamma\gamma}/c_{gg})^2/9$. When we assume the universal coupling $c_1 = c_2 = c_3$ (equivalent to $c_{gg} = c_{\gamma\gamma} = c_{WW} = c_{ZZ}$ and $c_{Z\gamma} = 0$), the Tevatron bound leads us to $c_1 = c_2 = c_3 \lesssim 0.1$. However, in this case, the χ production cross section becomes two orders of magnitude smaller than the Higgs boson production cross section at the ILC.

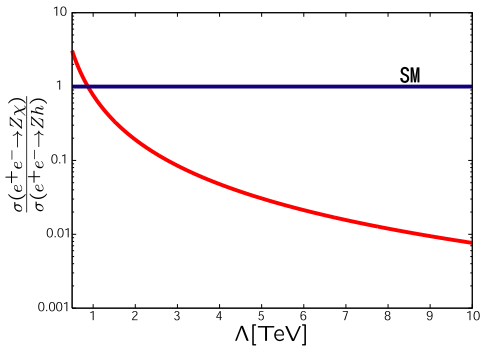

Figure 1: The ratio of total cross sections between the associated χ and Higgs productions as a function of Λ, at the ILC with the collider energy $\sqrt{s} = 500$ GeV. Here, we have fixed the parameters such as $m_\chi = m_h = 120$ GeV and $c_1 = c_2 = 1$. The ratio becomes one for $\Lambda \simeq 872$ GeV.

There are many possible choices of the parameter set (c_1, c_2 and c_3) so as to satisfy the Tevatron bound, while keeping the χ production cross section to be comparable to the Higgs boson one. To simplify our discussion, in this paper, we choose a special parameter set: $c_1 = c_2 = 1$ and $c_3 = 0$, namely the gluophobic but universal for c_1 and c_2. Therefore, the χ production channel through the gluon fusion is closed. For $m_\chi < 2m_W$, the hidden scalar has a 100% branching ratio into two photons.

3 Monte Carlo Simulation

As estimated in the previous section, if the cutoff is around 1 TeV, the production cross section of the hidden scalar can be comparable to the Higgs boson production cross section at the ILC. There are two main production processes associated with a Z-boson or a photon. In the following, we investigate each process. In our analysis, we take the same mass for the

hidden scalar and the Higgs boson: $m_\chi = m_h = 120$ GeV, as a reference.

3.a Observables to be measured

The associated hidden scalar production with a Z-boson is very similar to the Higgs production process and their production cross sections are comparable for $\Lambda \simeq 1$ TeV. One crucial difference is that the hidden scalar couples to Z-bosons through Eq. (2.59) so that the Z-boson in the final state is mostly transversely polarized. On the other hand, in the Higgs boson production the interaction between the Higgs boson and the longitudinal mode of the Z-boson dominates. In order to distinguish the hidden scalar from the Higgs boson, we will measure
(1) the angular distribution of the Z-boson in the final state,
(2) the polarization of the Z-boson in the final sate.

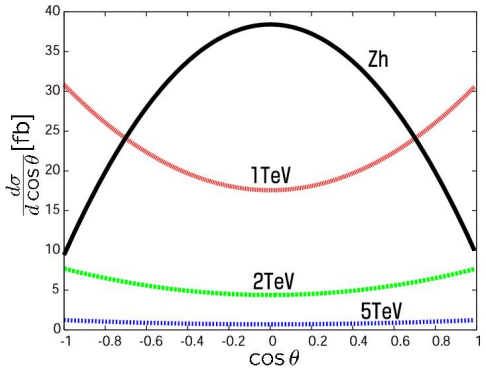

Figure 2: The angular dependence of the cross sections for $m_\chi = m_h = 120$ GeV and $c_1 = c_2 = 1$, at the ILC with the collider energy $\sqrt{s} = 500$ GeV and $\Lambda = 1$, 2 and 5 TeV.

As shown in the previous section, the branching ratio of the hidden scalar decay is quite different from the Higgs boson one. In our reference parameter set, the hidden scalar decays 100% into two photons. The Higgs boson with $m_h = 120$ GeV dominantly decays into a bottom and anti-bottom quark pair. In order to distinguish the hidden scalar from the Higgs boson, we will measure
(3) the branching ratios into two photons and into the bottom and anti-bottom quark pair through b-tagging.

The associated hidden scalar production with a photon is unique and such a process for the Higgs boson is negligible. We will investigate similar things as in the Z-boson case.

3.b Analysis Framework

For Monte Carlo simulation studies of the hidden scalar productions and decays, we have developed event generators of the processes: $e^+e^- \to \gamma\chi$ and $e^+e^- \to Z\chi$ followed by the $\chi \to \gamma\gamma$ decay, which are now included in `physsim-2007a` [9]. In the helicity amplitude calculations, we retain the Z-boson wave function if any and replace it with the wave function composed with the daughter fermion-antifermion pair according to the HELAS algorithm [10]. This allows us to properly take into account the gauge boson polarization effects. The phase space integration and generation of parton 4-momenta are performed with `BASES/SPRING` [11]. Parton showering and hadronization are carried out using `PYTHIA6.3` [12] with final-state tau leptons treated by `TAUOLA` [13] in order to handle their polarizations properly. The background $e^+e^- \to Zh$ events are generated using the $e^+e^- \to Z\chi$ generator with the $e^+e^- \to Z\chi$ helicity amplitudes replaced by corresponding $e^+e^- \to Zh$ amplitudes and the Higgs decay handled by `PYTHIA6.3`.

In the Monte Carlo simulations, we set the nominal center-of-mass energy at 500 GeV and assume no beam polarization. Effects of natural beam-energy spread and beamstrahlung

are taken into account according to the beam parameters given in [14]. We have assumed no crossing angle between the electron and the positron beams and ignored the transverse component of the initial state radiation. Consequently, the $Z\chi$ or $\gamma\chi$ system in our Monte-Carlo sample has no transverse momentum.

The generated Monte-Carlo events were passed to a detector simulator (`JSF Quick Simulator` [15]) which incorporates the ACFA-LC study parameters (see Table. 1). The quick simulator created vertex-detector hits, smeared charged-track parameters in the central tracker with parameter correlation properly taken into account, and simulated calorimeter signals as from individual segments, thereby allowing realistic simulation of cluster overlapping. It should also be noted that track-cluster matching was performed to achieve the best energy-flow measurements.

Detector	**Performance**	**Coverage**
Vertex detector	$\sigma_{\rm b} = 7.0 \oplus (20.0/p) \,/\, \sin^{3/2}\theta \ \mu$m	$\lvert\cos\theta\rvert \leq 0.90$
Central drift chamber	$\sigma_{p_T}/p_T = 1.1 \times 10^{-4} p_T \ \oplus \ 0.1\ \%$	$\lvert\cos\theta\rvert \leq 0.95$
EM calorimeter	$\sigma_E/E = 15\ \%\,/\sqrt{E} \ \oplus 1\ \%$	$\lvert\cos\theta\rvert \leq 0.90$
Hadron calorimeter	$\sigma_E/E = 40\ \%\,/\sqrt{E} \ \oplus 2\ \%$	$\lvert\cos\theta\rvert \leq 0.90$

Table 1: ACFA study parameters for an LC detector, where p, p_T, and E are measured in units of GeV.

3.c Event Selection and Results

3.c.1 $e^+e^- \to Z\chi; \chi \to \gamma\gamma$ *process*

Data equivalent to 50 fb^{-1} have been generated for both $e^+e^- \to Z\chi$ followed by $\chi \to \gamma\gamma$ and $e^+e^- \to Zh$ followed by $h \to \gamma\gamma$. A typical event is displayed in Figure 4. For the $Z\chi \to q\bar{q}\gamma\gamma$ process, there are two jets and two photons in the final state. In the event selection, it is firstly required that the number of reconstructed particles ($N_{particles}$) is greater than 4. In the next, the number of photons reconstructed in the calorimeters (N_{gammas}) is greater than 2, and the two photons whose invariant mass is the closest to m_χ are selected. Finally, the number of jets (N_{jets}) is required to be equal to 2. These selection criteria are summarized in Table 2 together with efficiency of each cut. The distribution of the invariant mass of the two photons which are considered to come from a χ decay is shown in Figure 5 after imposing all the above selection criteria. In the figure, the grey histogram is for the $e^+e^- \to Zh$ process where the number of remaining events is much less than that of the

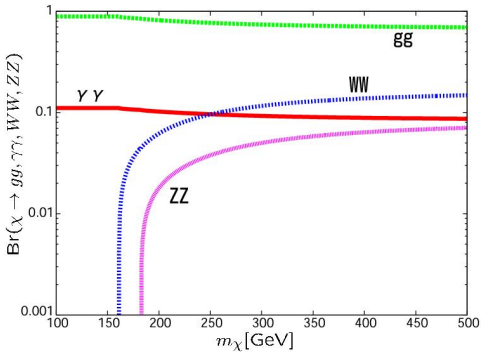

Figure 3: The branching ratio of the hidden scalar (χ) as a function of its mass m_χ for $c_1 = c_2 = c_3 = 1$. Different lines correspond to the modes, $\chi \to gg$, WW, $\gamma\gamma$ and ZZ.

$e^+e^- \to Z\chi$ process. Figures 6 and 7 show the χ and Higgs production angles (left) and the angular distribution of the reconstructed jets from associated Z-boson decays (right) for the both processes, respectively. As can be seen from these plots, χ couples with the transverse modes of the Z-bosons, while the Higgs boson couples with the longitudinal modes. The $e^+e^- \to Zh$ followed by $h \to A^0A^0$ process is also analyzed with the same cut conditions and its cut statistics is summarized in Table 2. Here, we have assumed $\mathrm{Br}(h \to A^0A^0) = 0.1$ and $\mathrm{Br}(A^0 \to \gamma\gamma) = 1$. The distribution of the invariant mass of the two photons will be similar to Figure 5 in this model, but again we can discriminate the χ from the Higgs by looking at the angular distributions. Figure 8 shows the Higgs production angle and the angular distribution of the reconstructed jets from associated Z-boson decays (right) for the $h \to A^0A^0$ process.

Cut	$Z\chi; \chi \to \gamma\gamma$	$Zh; h \to \gamma\gamma$	$Zh; h \to A^0A^0$
No Cut	2187 (1.0000)	142 (1.000)	7087 (1.0000)
$N_{particles} \geq 4$	1738 (0.7947)	106 (0.747)	5692 (0.8032)
$N_{gammas} \geq 2$	1521 (0.8751)	96 (0.906)	4865 (0.8547)
Cut on $M_{\gamma\gamma}$	1499 (0.9855)	95 (0.990)	4828 (0.9924)
$N_{jets} = 2$ for Ycut = 0.004	1498 (0.9993)	95 (1.000)	4825 (0.9994)
Total Efficiency	0.6850 ± 0.0099	0.669 ± 0.040	0.6808 ± 0.0055

Table 2: Cut statistics and breakdown of selection efficiency. The numbers inside and outside of parenthesis are the efficiency and the remaining number of events after each cut, respectively.

3.c.2 $e^+e^- \to \gamma\chi; \chi \to \gamma\gamma$ *process*

Data equivalent to 5.7 fb^{-1} have been generated for both signal ($e^+e^- \to \gamma\chi$ followed by $\chi \to \gamma\gamma$) and background ($e^+e^- \to \gamma\gamma$ with an ISR photon) processes. A typical signal event is displayed in Figure 9. For the $\gamma\chi \to \gamma\gamma\gamma$ process, there are three photons in the final state. The number of photons reconstructed in the calorimeters (N_{gammas}) is required to be equal to 3. It is also required that the energy and the cosine of the polar angle of each photon are greater than 1 GeV and less than 0.999, respectively. Among the photons, two photons whose invariant mass is within $m_\chi \pm 25$ GeV are considered to be from a χ decay. Finally, the cosines of the production angles of both χ and the remaining photon are required to be less than 0.99. These selection criteria are summarized in Table 3 together with their efficiencies. The distribution of the invariant mass of two photons which are considered to come from a χ decay (left) and the angular distribution of the χ (right) are shown in Figure 10 after imposing all the above selection criteria. A peak at m_χ can be clearly seen over the grey background histogram with the angular distribution consistent with $1 + \cos^2\theta$.

4 Summary and discussions

If a hidden scalar field appears in a certain class of new physics models around the TeV scale, there are interesting implications for collider phenomenology. In particular, since the

Cut	$\gamma\chi; \chi \to \gamma\gamma$	$\gamma\gamma$ with an ISR
No Cut	600 (1.0000)	100000 (1.0000)
$N_{gammas} = 3$	575 (0.9583)	3746 (0.0375)
$E_{gamma} > 1$ GeV	575 (1.0000)	3730 (0.9959)
$\lvert\cos(\theta_j)\rvert \leq 0.999$	575 (1.0000)	3728 (0.9992)
$\lvert M_{\gamma\gamma} - m_\chi\rvert \leq 25$ GeV	573 (0.9965)	1332 (0.3573)
$\lvert\cos(\theta_\chi)\rvert$ and $\lvert\cos(\theta_a)\rvert \leq 0.99$	572 (0.9983)	1269 (0.9529)
Total Efficiency	0.9533 ± 0.0086	0.0127 ± 0.0001

Table 3: Similar to Table 2 for $e^+e^- \to \gamma\chi$ and $e^+e^- \to \gamma\gamma$ with an ISR photon.

scalar behaves like the Higgs boson in its production process, it is an interesting issue how to distinguish the scalar from the Higgs boson in future collider experiments. We investigated the hidden scalar production at the ILC and addressed this issue based on realistic Monte Carlo simulations.

With the χ production cross section comparable to the Higgs boson one, the invariant mass distribution reconstructed from two-photon final states due to the decay mode $\chi \to \gamma\gamma$ shows a clear peak at m_χ. In the χ production associated with a Z-boson, the χ production angle and the angular distribution of the reconstructed jets from the associated Z-boson decay reveal that the hidden scalar couples to transversally polarized Z-bosons. On the other hand, the Higgs boson production associated with a Z-boson shows clearly different results in angular distributions and distinguishable from the hidden scalar production.

Some comments are in order here. In this paper, we have assumed that the hidden scalar couples with only the SM gauge bosons. In general, one can introduce couplings between the hidden scalar and the SM fermions and the Higgs doublets. Once these couplings are introduced, the phenomenology of χ productions can be drastically altered from those in this paper. In particular, the coupling of the hidden scalar to the Higgs doublets induces the mixing between χ and the Higgs boson. This mixing spoils the crucial difference between the hidden scalar and the Higgs boson that the former has nothing to do with the electroweak symmetry breaking while the latter is crucial for it. It is not natural but in practice, we can assume the above unwanted couplings to be small.

In fact, it is easy to introduce a setup where the couplings are naturally suppressed. As a simple example, let us consider a model in the context of the brane world scenario, where there are two different branes with the three spatial dimensions separated in extra-dimensional directions. Suppose that the SM gauge bosons live in the bulk and the hidden scalar resides on one brane while the SM fermions and the Higgs doublets on the other brane. In this setup, the couplings between the hidden scalar and the SM fermions and Higgs doublets are geometrically suppressed, while the hidden scalar couples with the bulk SM gauge bosons.

In our analysis, we have taken a special parameter set for simplicity, namely, the gluophobic ($c_3 = 0$) and universal ($c_2 = c_1$) couplings considering the Tevatron bound. In general, it is not necessary to take $c_3 = 0$ in order to avoid the Tevatron bound. For example, a parameter set, $c_{gg} = c_{\gamma\gamma} = 0.1$ and $c_{ZZ} = 1$, can be consistent with the Tevatron bound while keeping the χ production cross section comparable to that of Higgs boson. In this case, $c_{Z\gamma} \simeq 0.7$ and the hidden scalar decays into $Z\gamma$ with a sizable branching ratio. It is

interesting to study the χ production through its decay into $Z\gamma$. Also, in this parameter set, the decay mode into two gluons is sizable. It is hence an interesting issue how to distinguish χ from the Higgs boson through their hadronic decay modes. As can be seen from Eq. (2.61), the coupling between the hidden scalar and the longitudinal mode of the Z-boson is proportional to m_Z/E_Z and is sizable at low energy. To measure this coupling through the energy-dependence of the production angle distribution may provide an additional handle to pin down the χ production. For this purpose, the ILC with low energy could be useful.

In this paper, we have concentrated on the hidden scalar production associated with a Z-boson or a photon. It is also interesting to investigate the weak boson fusion process. For example, in the Z-boson fusion process, measuring the correlations between the cross section and the azimuthal angle between the final state electron and positron can be used to distinguish the couplings between a scalar and the Z-boson with different polarizations.

5 Acknowledgments

The authors would like to thank all the members of the ILC physics subgroup [16] for useful discussions. This study is supported in part by the Creative Scientific Research Grant No. 18GS0202 of the Japan Society for Promotion of Science.

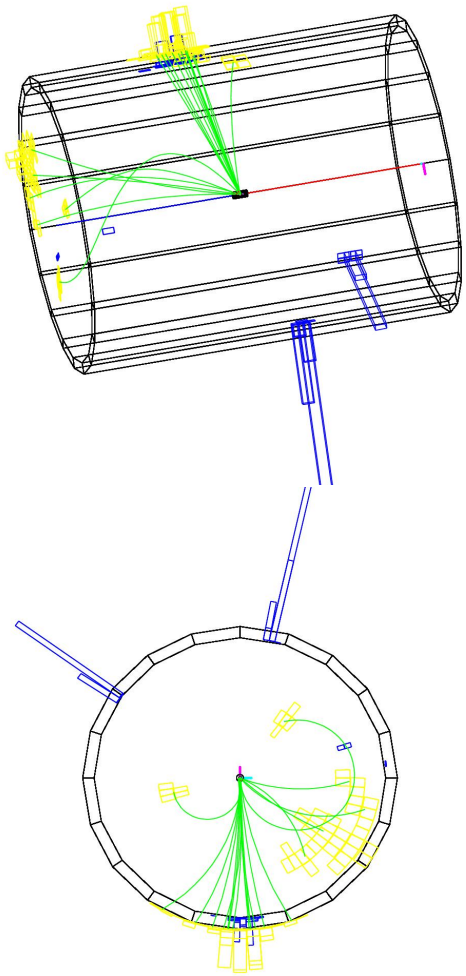

Figure 4: Event displays of $e^+e^- \to Z\chi$ followed by $\chi \to \gamma\gamma$. Two jets from the Z-boson decay and two photons from the χ decay can be clearly seen.

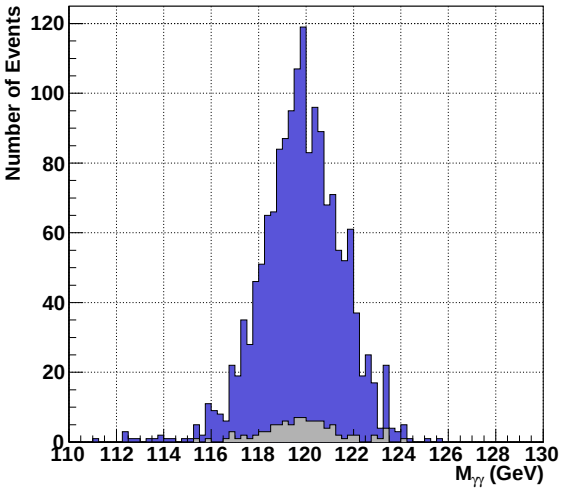

Figure 5: The distribution of the invariant mass of two photons which are considered to come from a χ decay.

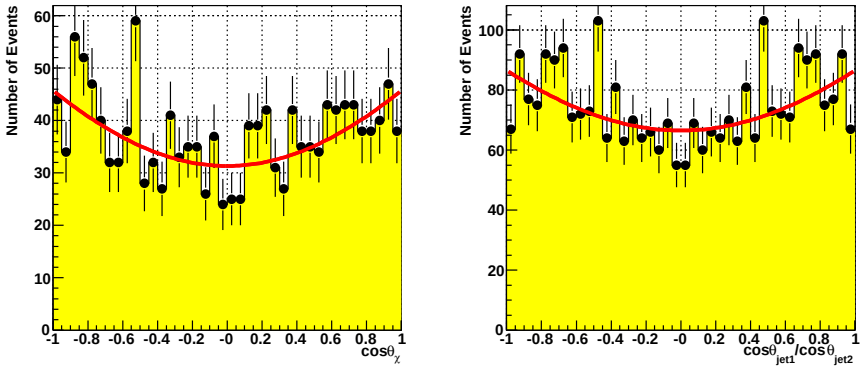

Figure 6: The χ production angle (left) and the angular distribution of the reconstructed jets from associated Z-boson decays (right).

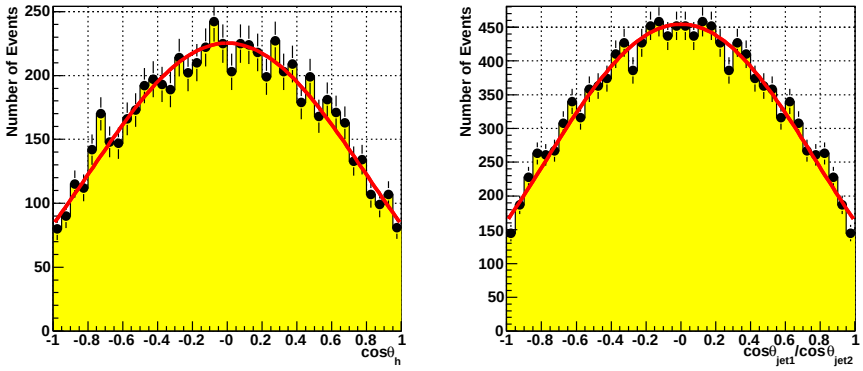

Figure 7: The Higgs production angle (left) and the angular distribution of the reconstructed jets from associated Z-boson decays (right) for $e^+e^- \to Zh$ followed by $H \to \gamma\gamma$.

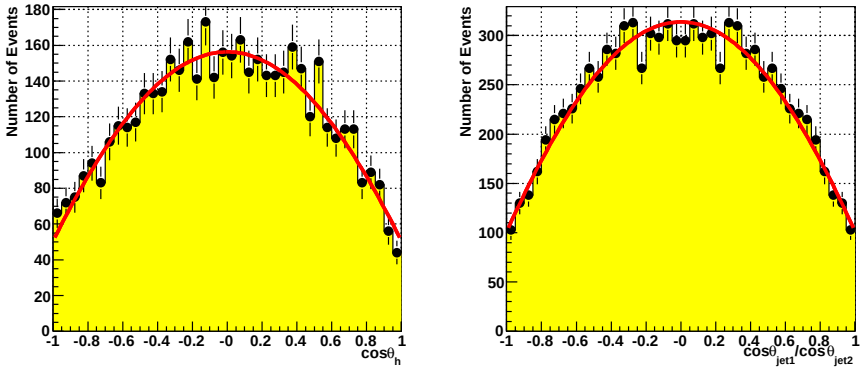

Figure 8: The Higgs production angle (left) and the angular distribution of the reconstructed jets from associated Z-boson decays (right) for $e^+e^- \to Zh$ followed by $h \to A^0A^0$.

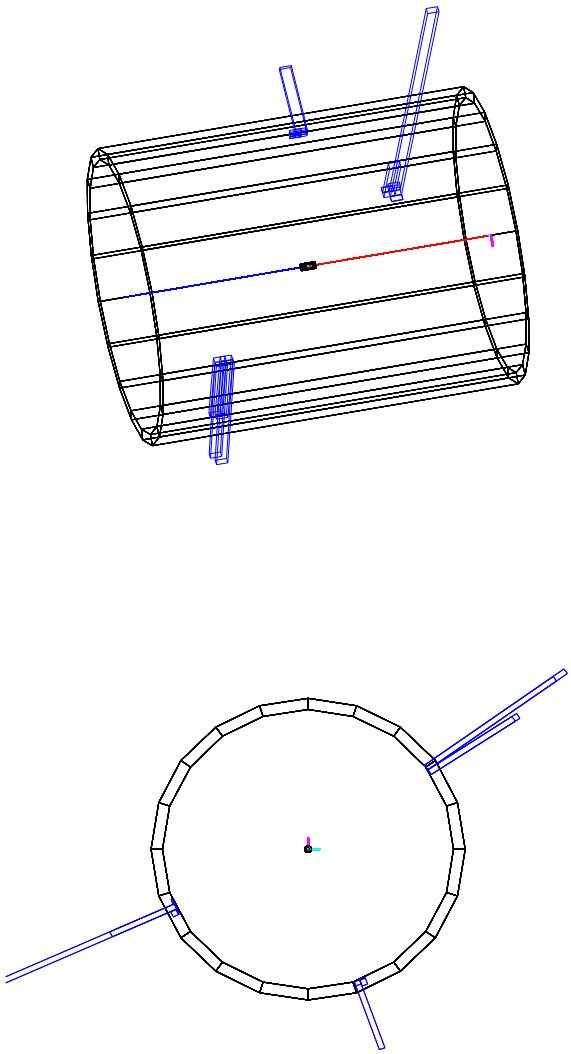

Figure 9: Event displays of $e^+e^- \to \gamma\chi$ followed by $\chi \to \gamma\gamma$.

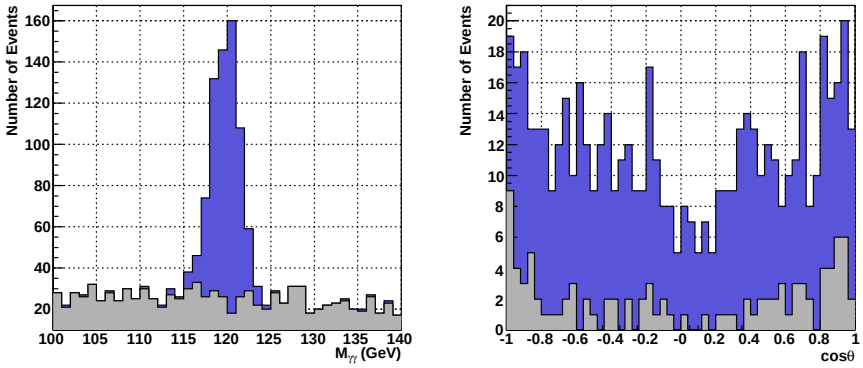

Figure 10: The distribution of the invariant mass of two photons which are considered to come from a χ decay (left) and the angular distribution of the χ (right) for the $e^+e^- \to \gamma\chi$ process with background.

References

[1] N. Arkani-Hamed, S. Dimopoulos and G. Dvali, Phys. Lett. **B429**, 263 (1998); I. Antoniadis, N. Arkani-Hamed, S. Dimopoulos and G. Dvali, Phys. Lett. **B436**, 257 (1998); N. Arkani-Hamed, S. Dimopoulos and G. Dvali, Phys. Rev. **D59**, 086004 (1999).

[2] L. Randall and R. Sundrum, Phys. Rev. Lett. **83**, 3370 (1999).

[3] See, for example, J. F. Gunion, H. E. Haber, G. L. Kane and S. Dawson, *The Higgs Hunter's Guide*, Addison-Weseley: Redwood City, California, 1989.

[4] B. A. Dobrescu, G. L. Landsberg and K. T. Matchev, Phys. Rev. D **63**, 075003 (2001).

[5] H. Itoh, N. Okada and T. Yamashita, Phys. Rev. D **74**, 055005 (2006).

[6] H. Georgi, Phys. Rev. Lett. **98**, 221601 (2007).

[7] H. Baer and J. D. Wells, Phys. Rev. D **57**, 4446 (1998) [arXiv:hep-ph/9710368]; W. Loinaz and J. D. Wells, Phys. Lett. B **445**, 178 (1998) [arXiv:hep-ph/9808287]; M. S. Carena, S. Mrenna and C. E. M. Wagner, Phys. Rev. D **60**, 075010 (1999) [arXiv:hep-ph/9808312]; Phys. Rev. D **62**, 055008 (2000) [arXiv:hep-ph/9907422].

[8] S. Mrenna and J. D. Wells, Phys. Rev. D **63**, 015006 (2000) [arXiv:hep-ph/0001226].

[9] physsim-2007a, `http://www-jlc.kek.jp/subg/offl/physsim/` .

[10] H. Murayama, I. Watanabe and K. Hagiwara, *KEK Report*, 91-11 (1992).

[11] S. Kawabata, *Comp. Phys. Commun.* **41**, 127 (1986).

[12] T. Sjöstrand, L. Lönnblad, S. Mrenna, P. Skands, hep-ph/0308153 (2003).

[13] S. Jadach, Z. Was, R. Decker and J. H. Kühn, *Comp. Phys. Commun.* **76**, 361 (1993).

[14] GLD Detector Outline Document.

[15] JSF Quick Simulator, `http://www-jlc.kek.jp/subg/offl/jsf/` .

ILC phenomenology in a TeV scale radiative seesaw model for neutrino mass, dark matter and baryon asymmetry

Mayumi Aoki[(a)], **Shinya Kanemura**[(b)], **Osamu Seto**[(c)]

[(a)] *Institute for Theoretical Physics, Kanazawa University, Kanazawa 920-1192, Japan*
[(b)] *Department of Physics, University of Toyama, Toyama 930-8555, Japan*
[(c)] *Department of Architecture and Building Engineering, Hokkai-Gakuen University, Sapporo 062-8605, Japan*

We discuss phenomenology in a new TeV scale model which would explain neutrino oscillation, dark matter, and baryon asymmetry of the Universe simultaneously by the dynamics of the extended Higgs sector and TeV-scale right-handed neutrinos. Tiny neutrino masses are generated at the three-loop level due to the exact Z_2 symmetry, by which the stability of the dark matter candidate is guaranteed. The model provides various discriminative predictions in Higgs phenomenology, which can be tested at the Large Hadron Collider and the International Linear Collider.

1 Introduction

In spite of the success of the Standard Model (SM) for elementary particles, it is widely understood that a new model beyond the SM must be considered to explain the phenomena such as tiny neutrino masses and their mixing [1], the nature of dark matter (DM) [2] and baryon asymmetry of the Universe [3].

We here discuss the model in which these problems would be simultaneously explained by the TeV-scale physics [4]. Tiny neutrino masses are generated at the three-loop level due to an exact discrete symmetry, by which tree-level Yukawa couplings of neutrinos are prohibited. The lightest neutral odd state under the discrete symmetry is a candidate of DM. Baryon asymmetry can also be generated at the electroweak phase transition (EWPT) by additional CP violating phases in the Higgs sector [5]. In this framework, a successful model can be made without contradiction of the current data.

The original idea of generating tiny neutrino masses via the radiative effect has been proposed by Zee [6]. The extension with a TeV-scale right-handed (RH) neutrino has been discussed in Ref. [7], where neutrino masses are generated at the three-loop level due to the exact Z_2 parity, and the Z_2-odd RH neutrino is a candidate of DM. This has been extended with two RH neutrinos to describe the neutrino data [8]. Several models with adding baryogenesis have been considered in Ref. [9]. The following advantages would be in the present model [4]: (a) all mass scales are at most at the TeV scale without large hierarchy, (b) physics for generating neutrino masses is connected with that for DM and baryogenesis, (c) the model parameters are strongly constrained by the current data, so that the model provides discriminative predictions which can be tested at future experiments.

In the following, we first explain the basic properties of the model, and discuss its phenomenology, in particular that at the International Linear Collider (ILC).

2 Model

Two scalar isospin doublets with hypercharge 1/2 (Φ_1 and Φ_2), charged singlet fields ($S^\pm$), a real scalar singlet (η) and two generation isospin-singlet RH neutrinos (N_R^α with $\alpha = 1, 2$) are introduced in our model [4]. We impose an exact Z_2 symmetry to generate tiny neutrino masses at the three-loop level, which we refer as Z_2. We assign Z_2-odd charge to $S^\pm$, η and N_R^α, while ordinary gauge fields, quarks and leptons and Higgs doublets are Z_2 even. In order to avoid the flavor changing neutral current in a natural way, we impose another (softly-broken) discrete symmetry ($\tilde{Z}_2$) [10]. We employ so called Type-X Yukawa interaction [11], where $\tilde{Z}_2$ charges are assigned such that only Φ_1 couples to leptons whereas Φ_2 does to quarks [12, 13, 14];

$$\mathcal{L}_Y = -y_{e_i}\overline{L}^i\Phi_1 e_R^i - y_{u_i}\overline{Q}^i\tilde{\Phi}_2 u_R^i - y_{d_i}\overline{Q}^i\Phi_2 d_R^i + \text{h.c.}, \tag{2.64}$$

where Q^i (L^i) is the ordinary i-th generation left-handed (LH) quark (lepton) doublet, and u_R^i and d_R^i (e_R^i) are RH-singlet up- and down-type quarks (charged leptons), respectively. We summarize the particle properties under Z_2 and $\tilde{Z}_2$ in Table 1.

The Yukawa coupling in Eq. (2.64) is different from that in the minimal supersymmetric SM (MSSM) [15]. In addition to the usual potential of the two Higgs doublet model (THDM) with the $\tilde{Z}_2$ parity and that of the Z_2-odd scalars, we have the interaction terms between Z_2-even and -odd scalars:

$$\mathcal{L}_{int} = -\sum_{a=1}^{2}\left(\rho_a|\Phi_a|^2|S|^2 + \sigma_a|\Phi_a|^2\frac{\eta^2}{2}\right) - \sum_{a,b=1}^{2}\left\{\kappa\,\epsilon_{ab}(\Phi_a^c)^\dagger\Phi_b S^-\eta + \text{h.c.}\right\}, \tag{2.65}$$

where ϵ_{ab} is the anti-symmetric tensor with $\epsilon_{12} = 1$. The mass term and the interaction for N_R^α are given by

$$\mathcal{L}_{Y_N} = \sum_{\alpha=1}^{2}\left\{\frac{1}{2}m_{N_R^\alpha}\overline{N_R^{\alpha\,c}}N_R^\alpha - h_i^\alpha\overline{(e_R^i)^c}N_R^\alpha S^- + \text{h.c.}\right\}. \tag{2.66}$$

Although the CP violating phase in the Lagrangian is crucial for successful baryogenesis at the EWPT [5], it does not much affect the following discussions. Thus, we neglect it for simplicity. We later give a comment on the case with the non-zero CP-violating phase.

As Z_2 is exact, the even and odd fields cannot mix. Mass matrices for the Z_2-even scalars are diagonalized as in the usual THDM by the mixing angles α and β, where α diagonalizes the CP-even states, and $\tan\beta = \langle\Phi_2^0\rangle/\langle\Phi_1^0\rangle$ [15]. The Z_2 even physical states are two CP-even (h and H), a CP-odd (A) and charged ($H^\pm$) states. We here define h and H such that h is always the SM-like Higgs boson when $\sin(\beta-\alpha) = 1$.

	Q^i	u_R^i	d_R^i	L^i	e_R^i	Φ_1	Φ_2	$S^\pm$	η	N_R^α
Z_2 (exact)	+	+	+	+	+	+	+	−	−	−
$\tilde{Z}_2$ (softly broken)	+	−	−	+	+	+	−	+	−	+

Table 1: Particle properties under the discrete symmetries.

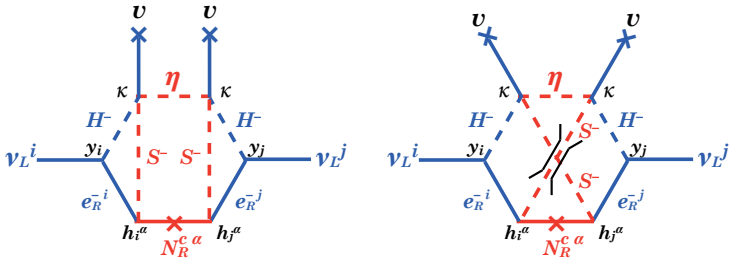

Figure 1: The diagrams for generating tiny neutrino masses.

Set	h_e^1	h_e^2	h_μ^1	h_μ^2	h_τ^1	h_τ^2	$B(\mu \to e\gamma)$
A	2.0	2.0	0.041	-0.020	0.0012	-0.0025	1.5×10^{-12}
B	2.2	2.1	0.0087	0.037	-0.0010	0.0021	7.8×10^{-12}

Table 2: Values of h_i^α for $m_{H^\pm}(m_{S^\pm}) = 100$ (400) GeV, $m_\eta = 50$ GeV, $m_{N_R^1} = m_{N_R^2}$ =3.0 TeV for the normal hierarchy. For Set A (B), $\kappa \tan\beta = 29$ (34) and $U_{e3} = 0$ (0.14). Predictions on the branching ratio of $\mu \to e\gamma$ are also shown.

3 Neutrino Mass, Dark Matter, and Strongly 1st-Order Phase Transition

The LH neutrino mass matrix M_{ij} is generated by the three-loop diagrams in Fig. 1. The absence of lower order loop contributions is guaranteed by Z_2. $H^\pm$ and e_R^i play a crucial role to connect LH neutrinos with the one-loop sub-diagram by the Z_2-odd states. We obtain

$$M_{ij} = \sum_{\alpha=1}^{2} C_{ij}^\alpha F(m_{H^\pm}, m_{S^\pm}, m_{N_R^\alpha}, m_\eta), \tag{3.67}$$

where $C_{ij}^\alpha = 4\kappa^2 \tan^2\beta (y_{e_i}^{\rm SM} h_i^\alpha)(y_{e_j}^{\rm SM} h_j^\alpha)$ with $y_{e_i}^{\rm SM} = \sqrt{2} m_{e_i}/v$ and $v \simeq 246$ GeV. The factor of the three-loop integral function $F(m_{H^\pm}, m_{S^\pm}, m_{N_R}, m_\eta)$ includes the suppression factor of $1/(16\pi^2)^3$, whose typical size is $\mathcal{O}(10^4)$eV. Magnitudes of $\kappa \tan\beta$ as well as F determine the universal scale of M_{ij}, whereas variation of h_i^α $(i = e,\ \mu,\ \tau)$ reproduces the mixing pattern indicated by the neutrino data [1].

Under the *natural* requirement $h_e^\alpha \sim \mathcal{O}(1)$, and taking the $\mu \to e\gamma$ search results into account [16], we find that $m_{N_R^\alpha} \sim \mathcal{O}(1)$ TeV, $m_{H^\pm} \lesssim \mathcal{O}(100)$ GeV, $\kappa \tan\beta \gtrsim \mathcal{O}(10)$, and $m_{S^\pm}$ being several times 100 GeV. On the other hand, the LEP direct search results indicate $m_{H^\pm}$ (and $m_{S^\pm}$) $\gtrsim 100$ GeV [1]. In addition, with the LEP precision measurement for the ρ parameter, possible values uniquely turn out to be $m_{H^\pm} \simeq m_H$ (or m_A) $\simeq 100$ GeV for $\sin(\beta - \alpha) \simeq 1$. Thanks to the Yukawa coupling in Eq. (2.64), such a light $H^\pm$ is not excluded by the $b \to s\gamma$ data [17]. Since we cannot avoid to include the hierarchy among $y_i^{\rm SM}$, we only require $h_i^\alpha y_i \sim \mathcal{O}(y_e) \sim 10^{-5}$ for values of h_i^α. Our model turns out to prefer the normal hierarchy scenario. Several sets for h_i^α are shown in Table 2 with the predictions

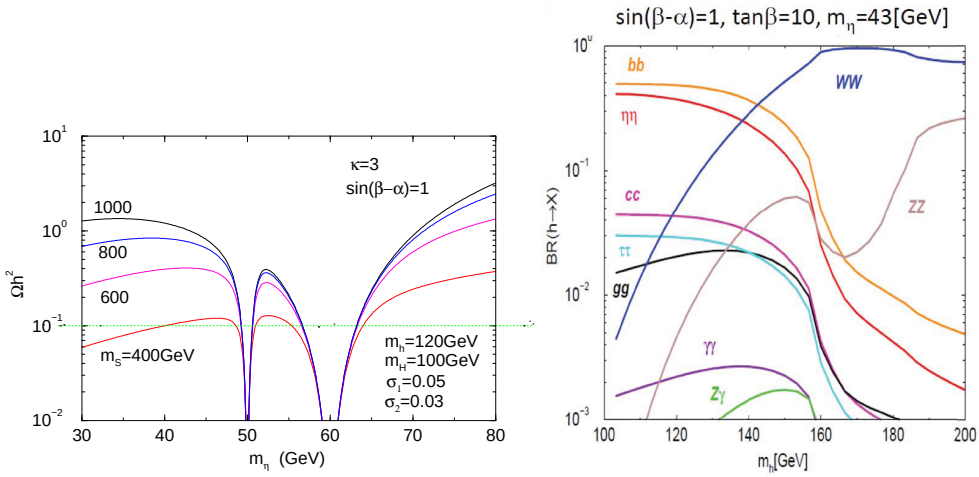

Figure 2: [Left figure] The relic abundance of η. [Right figure] The region of strong first order EWPT. Deviations from the SM value in the hhh coupling are also shown.

on the branching ratio of $\mu \to e\gamma$ assuming the normal hierarchy * .

The lightest Z_2-odd particle is stable and can be a candidate of DM if it is neutral. In our model, N_R^α must be heavy, so that the DM candidate is identified as η. When η is lighter than the W boson, η dominantly annihilates into $b\bar{b}$ and $\tau^+\tau^-$ via tree-level s-channel Higgs (h and H) exchange diagrams, and into $\gamma\gamma$ via one-loop diagrams. From their summed thermal averaged annihilation rate $\langle\sigma v\rangle$, the relic mass density $\Omega_\eta h^2$ is evaluated. Fig. 2(Left) shows $\Omega_\eta h^2$ as a function of m_η. Strong annihilation can be seen near 50 GeV $\simeq m_H/2$ (60 GeV $\simeq m_h/2$) due to the resonance of H (h) mediation. The data ($\Omega_{\rm DM}h^2 \simeq 0.11$ [2]) indicate that m_η is around 40-65 GeV.

The model satisfies the necessary conditions for baryogenesis [3]. Especially, departure from thermal equilibrium can be realized by the strong first order EWPT. The free energy is given at a high temperature T by

$$V_{eff}[\varphi, T] = D(T^2 - T_0^2)\varphi^2 - ET\varphi^3 + \frac{\lambda_T}{4}\varphi^4 + ..., \tag{3.68}$$

where φ is the order parameter. A large value of the coefficient E is crucial for the strong first order EWPT with keeping $m_h \lesssim 120$ GeV. For sufficient sphaleron decoupling in the broken phase, it is required that [18]

$$\frac{\varphi_c}{T_c}\left(\simeq \frac{2E}{\lambda_{T_c}}\right) \gtrsim 1, \tag{3.69}$$

where φ_c ($\neq 0$) and T_c are the critical values of φ and T at the EWPT. In Fig. 2(Right), the allowed region under the condition of Eq. (3.69) is shown. The condition is satisfied when $m_{S^\pm} \gtrsim 350$ GeV for $m_A \gtrsim 100$ GeV, $m_h \simeq 120$ GeV, $m_H \simeq m_{H^\pm}(\simeq M) \simeq 100$ GeV and $\sin(\beta-\alpha) \simeq 1$, where M represents the soft-breaking mass of extra Higgs bosons for $\tilde{Z}_2$ [4].

*The predictions for $\mu \to e\gamma$ shown here are corrected ones from those in Ref. [4].

4 Phenomenology

A successful scenario which can simultaneously solve the above three issues under the data [1, 16, 17] would be

$$\begin{array}{llll} \sin(\beta-\alpha)\simeq 1, & \kappa\tan\beta\simeq 30, & m_h=120\ \text{GeV}, & m_H\simeq m_{H^\pm}\simeq\mathcal{O}(100)\ \text{GeV}, \\ m_A\gtrsim\mathcal{O}(100)\ \text{GeV}, & m_{S^\pm}\sim 400\ \text{GeV}, & m_\eta\lesssim m_W, & m_{N_R^1}\simeq m_{N_R^2}\simeq 3\ \text{TeV}. \end{array} \quad (4.70)$$

This is realized without assuming unnatural hierarchy among the couplings. All the masses are between $\mathcal{O}(100)$ GeV and $\mathcal{O}(1)$ TeV. The discriminative properties of this scenario are in order:

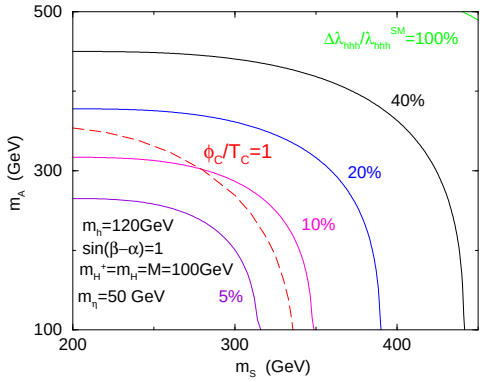

Figure 3: The decay branching ratios of the SM-like Higgs boson h.

(I) h is the SM-like Higgs boson, but decays into $\eta\eta$ when $m_\eta < m_h/2$. The branching ratio is about 30% for $m_\eta \simeq 43$ GeV and $\tan\beta = 10$: see Fig. 3. This is related to the DM abundance, so that our DM scenario is testable at the CERN Large Hadron Collider (LHC) and the ILC by searching the missing decay of h. Furthermore, η is potentially detectable by direct DM searches [19], because η can scatter with nuclei via the scalar exchange [20].

(II) For successful baryogenesis, the hhh coupling has to deviate from the SM value by more than 10-20 % [21] (see Fig. 2), which can be tested at the ILC [22].

(III) H (or A) can predominantly decay into $\tau^+\tau^-$ instead of $b\bar{b}$ for $\tan\beta \gtrsim 2$ because of the Type-X Yukawa interaction. For example, we have $B(H(A)\to\tau^+\tau^-)\simeq 100$ % and $B(H(A)\to\mu^+\mu^-)\simeq 0.3$ % for $m_A = m_H = 130$ GeV, $\sin(\beta-\alpha)=1$ and $\tan\beta = 10$. The scenario with light $H^\pm$ and H (or A) can be directly tested at the LHC via $pp\to W^*\to HH^\pm$ and $AH^\pm$ [23], and also $pp\to HA$. Their signals are four lepton states $\ell^-\ell^+\tau^\pm\nu$ and $\ell^-\ell^+\tau^+\tau^-$, where ℓ represents μ and τ [11]. At the ILC, the process $e^+e^-\to HA$ would be useful to discriminate the model from the other new physics candidates. In Fig. 4, the production rate of the $e^+e^-\to HA$ is shown for $m_A = m_H$. For $\sqrt{s} = 500$ GeV, about 17,000 (110) of the $\tau^+\tau^-\tau^+\tau^-$ ($\mu^+\mu^-\tau^+\tau^-$) events are then produced from the signal for $m_A = m_H = 130$ GeV [11], while about 60 (0) events are in the MSSM for the similar parameter set. The main back ground comes from ZZ production

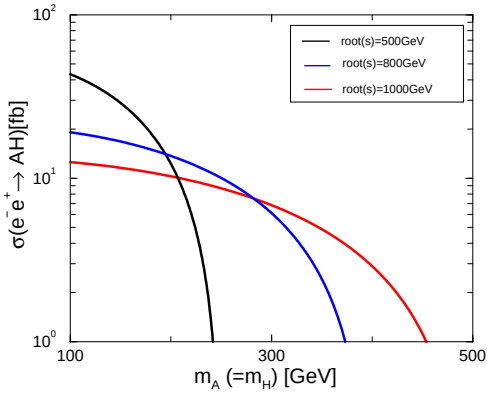

Figure 4: The production cross section of $e^+e^-\to HA$.

(about 400 fb), which is expected to be easily reduced by appropriate kinematic cuts.

(IV) The physics of Z_2-odd charged singlet $S^\pm$ is important to distinguish this model from the other models. At the LHC, they are produced in pair via the Drell-Yuan process [24]. The cross section amounts to 0.5 fb for $m_{S^\pm} = 400$ GeV at $\sqrt{s} = 14$ TeV, so that more than a hundred of the S^+S^- events are produced for the integrated luminosity 300 fb^{-1}. The produced $S^\pm$ bosons decay as $S^\pm \to H^\pm \eta$, and $H^\pm$ mainly decay into $\tau^\pm \nu$. The signal would be a high-energy hadron pair [25] with a large missing transverse momentum.

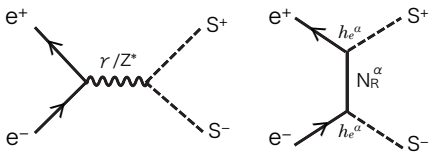

Figure 5: Feynman diagrams for the processes of $e^+e^- \to S^+S^-$.

The charged singlet scalar bosons $S^\pm$ in our model can also be better studied at the ILC via $e^+e^- \to S^+S^-$ shown in Fig. 6. The total cross sections are shown as a function of $m_{S^\pm}$ for $\sqrt{s}$ in Fig. 6. The other relevant parameters are taken as $m_{N_R^1} = m_{N_R^2} = 3$ TeV and $h_e^1 = h_e^2 = 2.0$. Both the contributions from the s-channel gauge boson (γ and Z) mediation and the t-channel RH neutrino mediation are included in the calculation. The total cross section can amount to about 200 fb for $m_{S^\pm} = 400$ GeV at $\sqrt{s} = 1$ TeV due to the contributions of the t-channel RH neutrino-mediation diagrams with $\mathcal{O}(1)$ coupling constants h_e^α. The signal would be a number of energetic tau lepton pairs with large missing energies. Although several processes such as $e^+e^- \to W^+W^-$ and $e^+e^- \to H^+H^-$ can give backgrounds for this final state, we expect that the signal events can be separated by kinematic cuts.

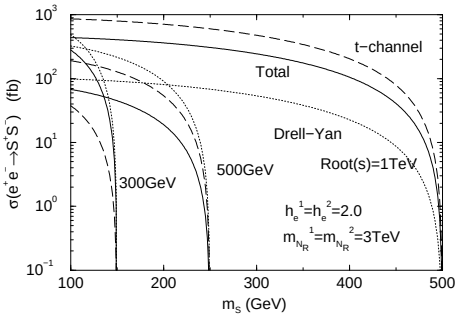

Figure 6: Production cross sections for $e^+e^- \to S^+S^-$ via the s-channel gauge boson (γ and Z) mediation (dotted curve), the t-channel RH-neutrino (N_R^α) mediation (solid curve), and both contributions (dashed curve) for $\sqrt{s} = 300$, 500 and 1000 GeV.

Finally, there is a further advantage in testing our model at the e^-e^- collision option of the ILC, where the dimension five operators $\ell^-\ell^- S^+S^+$, which appear in the sub-diagram of the three-loop induced masses of neutrinos in our model, can be directly measured. The production cross section for $e^-e^- \to S^-S^-$ [t-channel N_R^α mediation: see Fig. 7] is given by

$$\sigma(e^-e^- \to S^-S^-) = \int_{t_{\rm min}}^{t_{\rm max}} dt \frac{1}{128\pi s} \left| \sum_{\alpha=1}^{2} (|h_e^\alpha|^2 m_{N_R^\alpha}) \left(\frac{1}{t - m_{N_R^\alpha}^2} + \frac{1}{u - m_{N_R^\alpha}^2} \right) \right|^2 . \quad (4.71)$$

Due to the structure of our model that the tiny neutrino masses are generated at the three-loop level, the magnitudes of h_e^α ($\alpha = 1, 2$) are of $\mathcal{O}(1)$, by which the cross section becomes very large. Furthermore, thanks to the Majorana nature of the t-cahnnel diagram we obtain much larger cross section in the e^-e^- collision than at the e^+e^- collision when $m_{N_R^\alpha}^2 \gg s$. Fig. 8 shows the production cross sections for $e^-e^- \to S^-S^-$ via the t-channel RH-neutrino.

The cross section can be as large as 30 pb for $m_{S^\pm} = 400$ GeV for $\sqrt{s}_{e^-e^-} = 1$ TeV, $m_{N_R^1} = m_{N_R^2} = 3$ TeV and $h_e^1 = h_e^2 = 2.0$. The backgrounds are expected to be much less than the e^+e^- collision.

We emphasize that a combined study for these processes would be an important test for our model, in which neutrino masses are generated at the three-loop level by the Z_2 symmetry and the TeV-scale RH neutrinos [†].

In the other radiative seesaw models in which the neutrino masses are induced at the one-loop level with RH neutrinos, the corresponding coupling constants to our h_e^α couplings are necessarily one or two orders of magnitude smaller to satisfy the neutrino data, so that the cross section of the t-channel RH neutrino mediation processes are small due to the suppression factor $(h_e^\alpha)^4$.

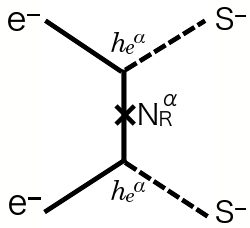

Figure 7: Feynman diagram for the processes of $e^-e^- \to S^-S^-$.

(V) The couplings h_i^α cause lepton flavor violation such as $\mu \to e\gamma$ which would provide information on $m_{N_R^\alpha}$ at future experiments.

Finally, we comment on the case with the CP violating phases. Our model includes the THDM, so that the same discussion can be applied in evaluation of baryon number at the EWPT [5]. The mass spectrum would be changed to some extent, but most of the features discussed above should be conserved with a little modification.

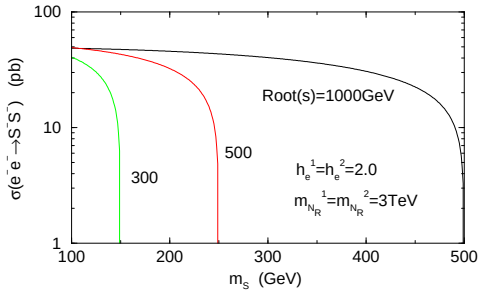

Figure 8: Production cross sections for $e^-e^- \to S^-S^-$ via the t-channel RH-neutrino (N_R^α) mediation for $\sqrt{s} = 300$, 500 and 1000 GeV.

5 Summary

We have discussed the model with the extended Higgs sector and TeV-scale RH neutrinos, which would explain neutrino mass and mixing, DM and baryon asymmetry by the TeV scale physics. It gives specific predictions on the collider phenomenology. In particular, the predictions on the Higgs physics are completely different from those in the MSSM, so that the model can be distinguished at the LHC and also at the ILC.

References

[1] W. M. Yao, et al., [Particle Data Group] J. Phys. G **33** (2006) 1.

[2] E. Komatsu *et al.* [WMAP Collaboration], Astrophys. J. Suppl. **180** (2009) 330.

[3] A. D. Sakharov, Pisma Zh. Eksp. Teor. Fiz. **5**, 32 (1967).

[†]Unlike our model, in the model in Ref. [7], the coupling constants corresponding to our h_e^α are small and instead those to h_μ^α are $\mathcal{O}(1)$, so that its Majorana structure is not easy to test at e^-e^- collisions.

[4] M. Aoki, S. Kanemura and O. Seto, Phys. Rev. Lett. **102**, 051805 (2009); Phys. Rev. D **80**, 033007 (2009).

[5] J. M. Cline, K. Kainulainen and A. P. Vischer, Phys. Rev. D **54**, 2451 (1996); L. Fromme, S. J. Huber and M. Seniuch, JHEP **0611**, 038 (2006).

[6] A. Zee, Phys. Lett. B **93**, 389 (1980) [Erratum-ibid. B **95**, 461 (1980)]; A. Zee, Phys. Lett. B **161**, 141 (1985).

[7] L. M. Krauss, S. Nasri and M. Trodden, Phys. Rev. D **67**, 085002 (2003).

[8] K. Cheung and O. Seto, Phys. Rev. D **69**, 113009 (2004).

[9] E. Ma, Phys. Rev. D **73**, 077301 (2006); J. Kubo, E. Ma and D. Suematsu, Phys. Lett. B **642**, 18 (2006); T. Hambye, K. Kannike, E. Ma and M. Raidal, Phys. Rev. D **75**, 095003 (2007).

[10] S. L. Glashow and S. Weinberg, Phys. Rev. D **15**, 1958 (1977).

[11] M. Aoki, S. Kanemura, K. Tsumura and K. Yagyu, Phys. Rev. D **80** (2009) 015017.

[12] V. D. Barger, J. L. Hewett and R. J. N. Phillips, Phys. Rev. D **41**, 3421 (1990).

[13] Y. Grossman, Nucl. Phys. B **426**, 355 (1994).

[14] S. Su and B. Thomas, Phys. Rev. D **79** (2009) 095014; H. E. Logan and D. MacLennan, Phys. Rev. D **79** (2009) 115022.

[15] J. F. Gunion, et al., "*The Higgs Hunters's Guide*" (Addison Wesley, 1990).

[16] A. Baldini, Nucl. Phys. Proc. Suppl. **168**, 334 (2007).

[17] E. Barberio *et al.* [Heavy Flavor Averaging Group], arXiv:0808.1297 [hep-ex].

[18] G. D. Moore, Phys. Lett. B **439**, 357 (1998); Phys. Rev. D **59**, 014503 (1998).

[19] Y. D. Kim, Phys. Atom. Nucl. **69**, 1970 (2006); D. S. Akerib, et al., Phys. Rev. Lett. **96**, 011302 (2006).

[20] J. McDonald, Phys. Rev. D **50**, 3637 (1994); for a recent study, see *e.g.*, H. Sung Cheon, S. K. Kang and C. S. Kim, J. Cosmol. Astropart. Phys. 05 (2008) 004.

[21] S. Kanemura, Y. Okada and E. Senaha, Phys. Lett. B **606**, 361 (2005).

[22] M. Battaglia, E. Boos and W. M. Yao, arXiv:hep-ph/0111276; Y. Yasui, et al., arXiv:hep-ph/0211047.

[23] S. Kanemura and C. P. Yuan, Phys. Lett. B **530**, 188 (2002); Q. H. Cao, S. Kanemura and C. P. Yuan, Phys. Rev. D **69**, 075008 (2004).

[24] S. Kanemura, T. Kasai, G. L. Lin, Y. Okada, J. J. Tseng and C. P. Yuan, Phys. Rev. D **64**, 053007 (2001).

[25] B. K. Bullock, K. Hagiwara and A. D. Martin, Phys. Rev. Lett. **67**, 3055 (1991).

Precision Measurements of the model parameters in the Littlest Higgs model with T-parity

Masaki Asano[(a)], **Eri Asakawa**[(b)], **Keisuke Fujii**[(c)], **Tomonori Kusano**[(d)], **Shigeki Matsumoto**[(e)], **Rei Sasaki**[(d)], **Yosuke Takubo**[(d)], and **Hitoshi Yamamoto**[(d)]

[(a)] *Institute for Cosmic Ray Research (ICRR), University of Tokyo, Kashiwa, Japan*
[(b)] *Institute of Physics, Meiji Gakuin University, Yokohama, Japan*
[(c)] *High Energy Accelerator Research Organization (KEK), Tsukuba, Japan*
[(d)] *Department of Physics, Tohoku University, Sendai, Japan*
[(e)] *Department of Physics, University of Toyama, Toyama, Japan*

We investigate a possibility of precision measurements for parameters of the Littlest Higgs model with T-parity at the International Linear Collider (ILC). The model predicts new gauge bosons which masses strongly depend on the vacuum expectation value that breaks a global symmetry of the model. Through Monte Carlo simulations of production processes of new gauge bosons, we show that these masses can be determined very accurately at the ILC for a representative parameter point of the model. From the simulation result, we also discuss the determination of other model parameters at the ILC.

1 Introduction

The Little Higgs model [1, 2] has been proposed for solving the little hierarchy problem. In this scenario, the Higgs boson is regarded as a pseudo Nambu-Goldstone (NG) boson associated with a global symmetry at some higher scale. Though the symmetry is not exact, its breaking is specially arranged to cancel quadratically divergent corrections to the Higgs mass term at 1-loop level. This is called the Little Higgs mechanism. As a result, the scale of new physics can be as high as 10 TeV without a fine-tuning on the Higgs mass term. Due to the symmetry, the scenario necessitates the introduction of new particles. In addition, the implementation of the Z_2 symmetry called T-parity to the model has been proposed in order to avoid electroweak precision measurements [3]. In this study, we focus on the Littlest Higgs model with T-parity as a simple and typical example of models implementing both the Little Higgs mechanism and T-parity.

In order to test the Little Higgs model, precise determinations of properties of Little Higgs partners are mandatory, because these particles are directly related to the cancellation of quadratically divergent corrections to the Higgs mass term. In particular, measurements of heavy gauge boson masses are quite important. Since heavy gauge bosons acquire mass terms through the breaking of the global symmetry, precise measurements of their masses allow us to determine the most important parameter of the model, namely the vacuum expectation value (VEV) of the breaking. Furthermore, because the heavy photon is a candidate for dark matter [8, 9], the determination of its property gives a great impact not only on particle physics but also on astrophysics and cosmology. However, it is difficult to

determine the properties of heavy gauge bosons at the Large Hadron Collider, because they have no color charge [6].

On the other hand, the ILC will provide an ideal environment to measure the properties of heavy gauge bosons. We study the sensitivity of the measurements to the Little Higgs parameters at the ILC based on a realistic Monte Carlo simulation [7]. We have used MadGraph [10] and Physsim [11] to generate signal and Standard Model (SM) events, respectively. In this study, we have also used PYTHIA6.4 [13], TAUOLA [14] and JSFQuickSimulator which implements the GLD geometry and other detector-performance related parameters [15].

2 Model

The Littlest Higgs model with T-parity is based on a non-linear sigma model describing an SU(5)/SO(5) symmetry breaking with a VEV, $f \sim \mathcal{O}(1)$ TeV. An $[\mathrm{SU}(2)\times\mathrm{U}(1)]^2$ subgroup in the SU(5) is gauged, which is broken down to the SM gauge group $\mathrm{SU}(2)_L\times\mathrm{U}(1)_Y$. Due to the presence of the gauge and Yukawa interactions, the SU(5) global symmetry is not exact. The SM doublet and triplet Higgs bosons (H and Φ) arise as pseudo NG bosons in the model. The triplet Higgs boson is T-odd, while the SM Higgs is T-even.

This model contains gauge fields of the gauged $[\mathrm{SU}(2)\times\mathrm{U}(1)]^2$ symmetry; The linear combinations $W^a = (W_1^a + W_2^a)/\sqrt{2}$ and $B = (B_1 + B_2)/\sqrt{2}$ correspond to the SM gauge bosons for the $\mathrm{SU}(2)_L$ and $\mathrm{U}(1)_Y$ symmetries. The other linear combinations $W_{\mathrm{H}}^a = (W_1^a - W_2^a)/\sqrt{2}$ and $B_{\mathrm{H}} = (B_1 - B_2)/\sqrt{2}$ are additional gauge bosons called heavy gauge bosons, which acquire masses of $\mathcal{O}(f)$ through the SU(5)/SO(5) symmetry breaking. After the electroweak symmetry breaking, the neutral components of W_{H}^a and B_{H} are mixed with each other and form mass eigenstates A_{H} and Z_{H}. The heavy gauge bosons (A_{H}, Z_{H}, and W_{H}) behave as T-odd particles, while SM gauge bosons are T-even.

To implement T-parity, two SU(2) doublets $l^{(1)}$ and $l^{(2)}$ are introduced for each SM lepton. The quantum numbers of $l^{(1)}$ and $l^{(2)}$ under the gauged $[\mathrm{SU}(2)\times\mathrm{U}(1)]^2$ symmetry are $(\mathbf{2}, -3/10; \mathbf{1}, -1/5)$ and $(\mathbf{1}, -1/5; \mathbf{2}, -3/10)$, respectively. The linear combination $l_{SM} = (l^{(1)} - l^{(2)})/\sqrt{2}$ gives the left-handed SM lepton. On the other hand, another linear combination $l_{\mathrm{H}} = (l^{(1)} + l^{(2)})/\sqrt{2}$ is vector-like T-odd partner which acquires the mass of $\mathcal{O}(f)$. The masses depend on the κ_l: $m_{e_{\mathrm{H}}} = \sqrt{2}\kappa_l f, m_{\nu_{\mathrm{H}}} = (1/2)(\sqrt{2} + \sqrt{1 + c_f})\kappa_l f \simeq \sqrt{2}\kappa_l f$. In addition, new particles are also introduced in quark sector. (For details, see Ref. [13].)

3 Simulation study

The representative point used in our simulation study is $(f, m_h, \lambda_2, \kappa_l)$ = (580 GeV, 134 GeV, 1.5, 0.5) where ($m_{A_{\mathrm{H}}}$, $m_{W_{\mathrm{H}}}$, $m_{Z_{\mathrm{H}}}$, m_{Φ}) = (81.9 GeV, 368 GeV, 369 GeV, 440 GeV) and λ_2 is an additional Yukawa coupling in the top sector. The model parameter satisfies not only the current electroweak precision data but also the WMAP observation [7]. Furthermore, no fine-tuning is needed at the sample point to keep the Higgs mass on the electroweak scale [15, 16].

In the model, there are four processes whose final states consist of two heavy gauge bosons: $e^+e^- \to A_{\mathrm{H}}A_{\mathrm{H}}$, $A_{\mathrm{H}}Z_{\mathrm{H}}$, $Z_{\mathrm{H}}Z_{\mathrm{H}}$, and $W_{\mathrm{H}}^+W_{\mathrm{H}}^-$. The first process is undetectable. At the representative point, the largest cross section is expected for the fourth process, which is open at $\sqrt{s} > 1$ TeV. On the other hand, because $m_{A_{\mathrm{H}}} + m_{Z_{\mathrm{H}}}$ is less than 500 GeV, the second process is important already at the $\sqrt{s} = 500$ GeV. We, hence, concentrate on

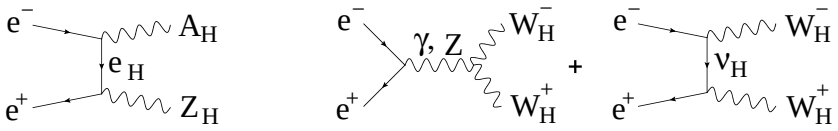

Figure 1: Diagrams for signal processes; $e^+e^- \to A_{\rm H}Z_{\rm H}$ and $e^+e^- \to W_{\rm H}^+W_{\rm H}^-$.

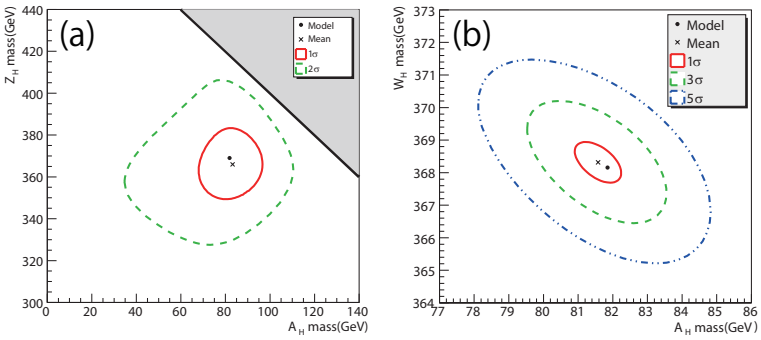

Figure 2: Probability contours corresponding to (a) 1- and 2-σ deviations from the best fit point in the $A_{\rm H}$ and $Z_{\rm H}$ mass plane, and (b) 1-, 3-, and 5-σ deviations in the $A_{\rm H}$ and $W_{\rm H}$ mass plane. The shaded area in (a) shows the unphysical region of $m_{A_{\rm H}} + m_{Z_{\rm H}} > 500$ GeV.

$e^+e^- \to A_{\rm H}Z_{\rm H}$ at $\sqrt{s} = 500$ GeV and $e^+e^- \to W_{\rm H}^+W_{\rm H}^-$ at $\sqrt{s} = 1$ TeV. Feynman diagrams for the signal processes are shown in Fig. 1.

For the $A_{\rm H}Z_{\rm H}$ production at $\sqrt{s} = 500$ GeV with an integrated luminosity of 500 fb^{-1}, we define $A_{\rm H}Z_{\rm H} \to A_{\rm H}A_{\rm H}h \to A_{\rm H}A_{\rm H}bb$ as our signal event. The $A_{\rm H}$ and $Z_{\rm H}$ boson masses can be estimated from the edges of the distribution of the reconstructed Higgs boson energies. The endpoints have been estimated by fitting the distribution with a line shape determined by a high statistics signal sample. The fit resulted in $m_{A_{\rm H}}$ and $m_{Z_{\rm H}}$ being 83.2 ± 13.3 GeV and 366.0 ± 16.0 GeV, respectively.

For the $W_{\rm H}W_{\rm H}$ production at $\sqrt{s} = 1$ TeV with an integrated luminosity of 500 fb^{-1}, we have used 4-jet final states, $W_{\rm H}^+W_{\rm H}^- \to A_{\rm H}A_{\rm H}W^+W^- \to A_{\rm H}A_{\rm H}qqqq$. The masses of $A_{\rm H}$ and $W_{\rm H}$ bosons can be determined from the edges of the W energy distribution. The fitted masses of $A_{\rm H}$ and $W_{\rm H}$ bosons are 81.58 ± 0.67 GeV and 368.3 ± 0.63 GeV, respectively. Using the process, it is also possible to confirm that the spin of $W_{\rm H}^\pm$ is consistent with one and the polarization of $W^\pm$ from the $W_{\rm H}^\pm$ decay is dominantly longitudinal. Furthermore, the gauge charges of the $W_{\rm H}$ boson could be also measured using a polarized electron beam.

Figure 2 shows the probability contours for the masses of $A_{\rm H}$ and $W_{\rm H}$ at 1 TeV together with that of $A_{\rm H}$ and $Z_{\rm H}$ at 500 GeV. The mass resolution improves dramatically at $\sqrt{s} = 1$ TeV, compared to that at $\sqrt{s} = 500$ GeV.

4 Conclusion

The Littlest Higgs Model with T-parity is one of the attractive candidates for physics beyond the SM. We have shown that the masses of the heavy gauge bosons can be determined very accurately at the ILC. It is important to notice that these masses are obtained in a model-independent way, so that it is possible to test the Little Higgs model by comparing them with the theoretical predictions. Furthermore, since the masses of the heavy gauge bosons are determined by the VEV f, it is possible to accurately determine f. From the results obtained in our simulation study, it turns out that the VEV f can be determined to accuracies of 4.3% at $\sqrt{s} = 500$ GeV and 0.1% at $\sqrt{s} = 1$ TeV. Another Little Higgs parameter κ_l could also be estimated from production cross sections for the heavy gauge bosons, because the cross sections depend on the masses of heavy leptons. At the ILC with $\sqrt{s} = 500$ GeV and 1 TeV, κ_l could be obtained within 9.5% and 0.8% accuracies, respectively.

Finally, We have also found that the thermal abundance of dark matter relics can be determined to 10% and 1% levels at $\sqrt{s} = 500$ GeV and $\sqrt{s} = 1$ TeV, respectively. These accuracies are comparable to those of current and future cosmological observations such as the PLANCK satellite [17], implying that the ILC experiment will play an essential role to understand the thermal history of our universe.

5 Acknowledgments

The authors would like to thank all the members of the ILC physics subgroup [16] for useful discussions. This study is supported in part by the Creative Scientific Research Grant No. 18GS0202 of the Japan Society for Promotion of Science.

References

[1] N. Arkani-Hamed, A. G. Cohen and H. Georgi, Phys. Lett. B **513** (2001) 232; N. Arkani-Hamed, A. G. Cohen, E. Katz, A. E. Nelson, T. Gregoire and J. G. Wacker, JHEP **0208** (2002) 021.

[2] N. Arkani-Hamed, A. G. Cohen, E. Katz and A. E. Nelson, JHEP **0207** (2002) 034.

[3] H. C. Cheng and I. Low, JHEP **0309** (2003) 051; H. C. Cheng and I. Low, JHEP **0408** (2004) 061; I. Low, JHEP **0410** (2004) 067.

[4] J. Hubisz and P. Meade, Phys. Rev. D **71** (2005) 035016, (For the correct paramter region consistent with the WMAP observation, see the figure in the revised vergion, hep-ph/0411264v3).

[5] M. Asano, S. Matsumoto, N. Okada and Y. Okada, Phys. Rev. D **75** (2007) 063506; A. Birkedal, A. Noble, M. Perelstein and A. Spray, Phys. Rev. D **74** (2006) 035002; M. Perelstein and A. Spray, Phys. Rev. D **75** (2007) 083519.

[6] Q. H. Cao and C. R. Chen, Phys. Rev. D **76** (2007) 075007.

[7] E. Asakawa *et al.*, arXiv:0901.1081 [hep-ph].

[8] http://madgraph.hep.uiuc.edu/.

[9] http://acfahep.kek.jp/subg/sim/softs.html.

[10] T. Sjòstrand, *Comp, Phys. Comm.* **82** (1994) 74.

[11] http://wasm.home.cern.ch/wasm/goodies.html.

[12] GLD Detector Outline Document, arXiv:physics/0607154.

[13] M. Schmaltz and D. Tucker-Smith, Ann. Rev. Nucl. Part. Sci. **55** (2005) 229; M. Perelstein, Prog. Part. Nucl. Phys. **58** (2007) 247.

[14] E. Komatsu *et al.* [WMAP Collaboration], arXiv:0803.0547 [astro-ph].

[15] J. Hubisz, P. Meade, A. Noble and M. Perelstein, JHEP **0601** (2006) 135.

[16] S. Matsumoto, T. Moroi and K. Tobe, Phys. Rev. D **78** (2008) 055018.

[17] [Planck Collaboration], arXiv:astro-ph/0604069.

[18] http://www-jlc.kek.jp/subg/physics/ilcphys/.

Measurement of Heavy Gauge Bosons in the Little Higgs Model with T-parity at ILC

Yosuke Takubo[(a)], **Eri Asakawa**[(b)], **Masaki Asano**[(a)], **Keisuke Fujii**[(c)], **Tomonori Kusano**[(a)], **Shigeki Matsumoto**[(d)], **Rei Sasaki**[(a)], and **Hitoshi Yamamoto**[(a)]

[(a)] *Department of Physics, Tohoku University, Sendai, Japan*
[(b)] *Institute of Physics, Meiji Gakuin University, Yokohama, Japan*
[(c)] *High Energy Accelerator Research Organization (KEK), Tsukuba, Japan*
[(d)] *Department of Physics, University of Toyama, Toyama, Japan*

The Littlest Higgs Model with T-parity is one of the attractive candidates of physics beyond the Standard Model. One of the important predictions of the model is the existence of new heavy gauge bosons, where they acquire mass terms through the breaking of global symmetry necessarily imposed on the model. The determination of the masses are, hence, quite important to test the model. In this paper, the measurement accuracy of the heavy gauge bosons at ILC is reported.

1 Introduction

There are a number of scenarios for new physics beyond the Standard Model. The most famous one is the supersymmetric scenario. Recently, alternative one called the Little Higgs scenario has been proposed [1, 2]. In this scenario, the Higgs boson is regarded as a pseudo Nambu-Goldstone boson associated with a global symmetry at some higher scale. A Z_2 symmetry called T-parity is imposed on the models to satisfy constraints from electroweak precision measurements [3, 4, 5]. Under the parity, new particles are assigned to be T-odd (i.e. with a T-parity of -1), while the SM particles are T-even. The lightest T-odd particle is stable and provides a good candidate for dark matter. In this article, we focus on the Littlest Higgs model with T-parity as a simple and typical example of models implementing both the Little Higgs mechanism and T-parity.

In order to test the Little Higgs model, precise determinations of properties of Little Higgs partners are mandatory, because these particles are directly related to the cancellation of quadratically divergent corrections to the Higgs mass term. In particular, measurements of heavy gauge boson masses, Little Higgs partners for gauge bosons, are quite important. Since heavy gauge bosons acquire mass terms through the breaking of the global symmetry, precise measurements of their masses allow us to determine the most important parameter of the model, namely the vacuum expectation value of the breaking.

We studied the measurement accuracy of masses of the heavy gauge bosons at the international linear collider (ILC). In addition, the sensitivity to the vacuum expectation value (f) was estimated. In this paper, the status of the study is shown, and the detail of this study is described in [6].

$\sqrt{s}$	$e^+e^- \to A_{\rm H}Z_{\rm H}$	$e^+e^- \to Z_{\rm H}Z_{\rm H}$	$e^+e^- \to W_{\rm H}^+W_{\rm H}^-$
500 GeV	1.91 (fb)	—	—
1 TeV	7.42 (fb)	110 (fb)	277 (fb)

Table 1: Cross sections for the production of heavy gauge bosons.

2 Representative point and target mode

In order to perform a numerical simulation at ILC, we need to choose a representative point in the parameter space of the Littlest Higgs model with T-parity. Firstly, the model parameters should satisfy the current electroweak precision data. In addition, the cosmological observation of dark matter relics also gives important information. Thus, we consider not only the electroweak precision measurements but also the WMAP observation [7] to choose a point in the parameter space. We have selected a representative point where Higgs mass and f are 134 GeV and 580 GeV, respectively. At the representative point, we have obtained $\Omega_{\rm DM}h^2$ of 1.05. The masses of the heavy gauge bosons are ($M_{A_{\rm H}}$, $M_{W_{\rm H}}$, $M_{Z_{\rm H}}$) = (81.9 GeV, 368 GeV, 369 GeV), where $A_{\rm H}$, $Z_{\rm H}$, and $W_{\rm H}$ are the Little Higgs partners of a photon, Z boson, and W boson, respectively. Here, $A_{\rm H}$ plays the role of dark matter in this model [8, 9]. Since all the heavy gauge bosons are lighter than 500 GeV, it is possible to generate them at ILC.

There are four processes whose final states consist of two heavy gauge bosons: $e^+e^- \to A_{\rm H}A_{\rm H}$, $A_{\rm H}Z_{\rm H}$, $Z_{\rm H}Z_{\rm H}$, and $W_{\rm H}^+W_{\rm H}^-$. The first process is undetectable, thus not considered in this article. The cross sections of the other processes are shown in Table 1. Since $m_{A_{\rm H}} + m_{Z_{\rm H}}$ is less than 500 GeV, $A_{\rm H}Z_{\rm H}$ can be produced at the $\sqrt{s} = 500$ GeV. At $\sqrt{s} = 1$ TeV, we can observe $W_{\rm H}^+W_{\rm H}^-$ with large cross section. We, hence, concentrate on $e^+e^- \to A_{\rm H}Z_{\rm H}$ at $\sqrt{s} = 500$ GeV and $e^+e^- \to W_{\rm H}^+W_{\rm H}^-$ at $\sqrt{s} = 1$ TeV. Feynman diagrams for the signal processes are shown in Fig. 1. Note that $Z_{\rm H}$ decays into $A_{\rm H}h$, and $W_{\rm H}^\pm$ decays into $A_{\rm H}W^\pm$ with almost 100% branching fractions.

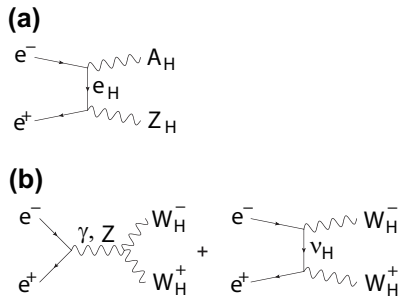

Figure 1: Diagrams for signal processes; (a) $e^+e^- \to A_{\rm H}Z_{\rm H}$ and (b) $e^+e^- \to W_{\rm H}^+W_{\rm H}^-$.

3 Simulation tools

We have used MadGraph [10] to generate $e^+e^- \to A_{\rm H}Z_{\rm H}$ at $\sqrt{s} = 500$ GeV, while $e^+e^- \to W_{\rm H}^+W_{\rm H}^-$ at $\sqrt{s} = 1$ TeV and all the standard model events have been generated by Physsim [11]. We ignored the initial- and final-state radiation, beamstrahlung, and the beam energy spread for study of $e^+e^- \to A_{\rm H}Z_{\rm H}$ at $\sqrt{s} = 500$ GeV, whereas their effects were considered for study of $e^+e^- \to W_{\rm H}^+W_{\rm H}^-$ at $\sqrt{s} = 1$ TeV where the beam energy spread is set to 0.14% for the electron beam and 0.07% for the positron beam. The finite crossing angle between the electron and positron beams was assumed to to be zero. In both event generators, the helicity amplitudes were calculated using the HELAS library [12], which allows us to deal with the effect of gauge boson polarizations properly.

Process	Cross sec. [fb]	# of events	# of events after all cuts
$A_{\rm H}Z_{\rm H} \to A_{\rm H}A_{\rm H}bb$	1.05	525	272
$\nu\nu h \to \nu\nu bb$	34.0	17,000	3,359
$Zh \to \nu\nu bb$	5.57	2,785	1,406
$tt \to WWbb$	496	248,000	264
$ZZ \to \nu\nu bb$	25.5	12,750	178
$\nu\nu Z \to \nu\nu bb$	44.3	22,150	167
$\gamma Z \to \gamma bb$	1,200	600,000	45

Table 2: Signal and backgrounds processes considered in the $A_{\rm H}Z_{\rm H}$ analysis.

Parton showering and hadronization have been carried out by using PYTHIA6.4 [13], where final-state tau leptons are decayed by TAUOLA [14] in order to handle their polarizations correctly. The generated Monte Carlo events have been passed to a detector simulator called JSFQuickSimulator, which implements the GLD geometry and other detector-performance related parameters [15].

4 Analysis

In this section, we present simulation and analysis results for heavy gauge boson productions. The simulation has been performed at $\sqrt{s} = 500$ GeV for the $A_{\rm H}Z_{\rm H}$ production and at $\sqrt{s} =$ 1 TeV for the $W_{\rm H}^+W_{\rm H}^-$ production with an integrated luminosity of 500 fb^{-1}.

4.a $e^+e^- \to A_{\rm H}Z_{\rm H}$ at 500 GeV

$A_{\rm H}$ and $Z_{\rm H}$ are produced with the cross section of 1.9 fb at the center of mass energy of 500 GeV. Since $Z_{\rm H}$ decays into $A_{\rm H}$ and the Higgs boson, the signature is a single Higgs boson in the final state, mainly 2 jets from $h \to b\bar{b}$ (with a 55% branching ratio). We, therefore, define $A_{\rm H}Z_{\rm H} \to A_{\rm H}A_{\rm H}bb$ as our signal event. For background events, contribution from light quarks was not taken into account because such events can be rejected to negligible level after requiring the existence of two b-jets, assuming a b-tagging efficiency of 80% for b-jets with 15% probability to misidentify a c-jet as a b-jet. This b-tagging performance was estimated by the full simulation, assuming a typical ILC detector. Signal and background processes considered in this analysis are summarized in Table 2. Figure 2 shows a typical $A_{\rm H}Z_{\rm H}$ event seen in the detector simulator.

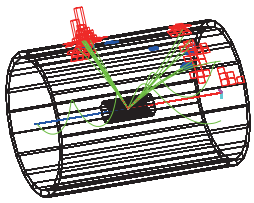

Figure 2: A typical event of $A_{\rm H}Z_{\rm H}$ in the simulator.

The clusters in the calorimeters are combined to form a jet if the two clusters satisfy $y_{ij} < y_{\rm cut}$. y_{ij} is defined as

$$y_{ij} = \frac{2E_iE_j(1-\cos\theta_{ij})}{E_{\rm vis}^2}, \tag{4.72}$$

where θ_{ij} is the angle between momenta of two clusters, $E_{i(j)}$ are their energies, and $E_{\rm vis}$ is

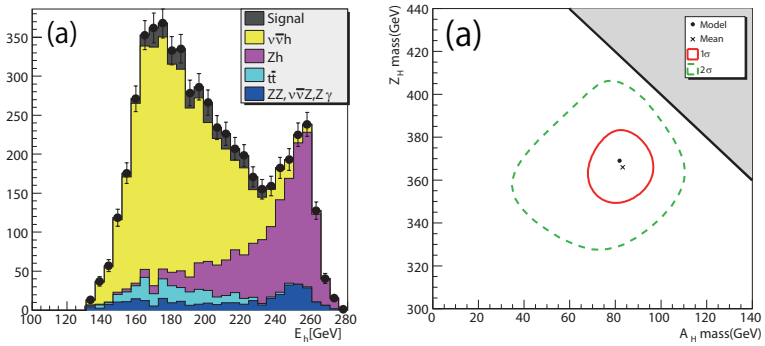

Figure 3: (a)Energy distribution of the reconstructed Higgs bosons with remaining backgrounds after the mass cut. (b) Probability contours corresponding to 1- and 2-σ deviations from the best fit point in the $A_{\rm H}$ and $Z_{\rm H}$ mass-plane. The shaded area shows the unphysical region of $m_{A_{\rm H}} + m_{Z_{\rm H}} > 500$ GeV.

the total visible energy. All events are forced to have two jets by adjusting $y_{\rm cut}$. We have selected events with the reconstructed Higgs mass in a window of $100 - 140$ GeV. Since Higgs bosons coming from the WW fusion process have the transverse momentum ($p_{\rm T}$) mostly below W mass, $p_{\rm T}$ is required to be above 80 GeV in order to suppress the $\nu\nu h \to \nu\nu bb$ background. Finally, multiplying the efficiency of double b-tagging ($0.8 \times 0.8 = 0.64$), we are left with 272 signal and 5,419 background events as shown in Table 2, which corresponds to a signal significance of 3.7 ($= 272/\sqrt{5419}$) standard deviations. The indication of the new physics signal can hence be obtained at $\sqrt{s} = 500$ GeV.

The masses of $A_{\rm H}$ and $Z_{\rm H}$ bosons can be estimated from the edges of the distribution of the reconstructed Higgs boson energies. This is because the maximum and minimum Higgs boson energies ($E_{\rm max}$ and $E_{\rm min}$) are written in terms of these masses,

$$\begin{aligned} E_{\rm max} &= \gamma_{Z_{\rm H}} E_h^* + \beta_{Z_{\rm H}} \gamma_{Z_{\rm H}} p_h^*, \\ E_{\rm min} &= \gamma_{Z_{\rm H}} E_h^* - \beta_{Z_{\rm H}} \gamma_{Z_{\rm H}} p_h^*, \end{aligned} \tag{4.73}$$

where $\beta_{Z_{\rm H}}(\gamma_{Z_{\rm H}})$ is the $\beta(\gamma)$ factor of the $Z_{\rm H}$ boson in the laboratory frame, while $E_h^*(p_h^*)$ is the energy (momentum) of the Higgs boson in the rest frame of the $Z_{\rm H}$ boson. Note that E_h^* is given as $(M_{Z_{\rm H}}^2 + M_h^2 - M_{A_{\rm H}}^2)/(2M_{Z_{\rm H}})$.

Figure 3(a) shows the energy distribution of the reconstructed Higgs bosons with remaining backgrounds. The background events are subtracted from Fig. 3(a), assuming that the background distribution can be understand completely. Then, the endpoints, $E_{\rm max}$ and $E_{\rm min}$, have been estimated by fitting the distribution with a line shape determined by a high statistics signal sample. The fit resulted in $m_{A_{\rm H}}$ and $m_{Z_{\rm H}}$ to be 83.2 ± 13.3 GeV and 366.0 ± 16.0 GeV, respectively, which should be compared to their true values: 81.85 GeV and 368.2 GeV. Figure 3(b) shows the probability contours for the masses of $A_{\rm H}$ and $Z_{\rm H}$.

Since the masses of the heavy gauge bosons are from the vacuum expectation value (f), f can be determined by fitting the energy distribution of the reconstructed Higgs bosons. Then, f was determined to be $f = 576.0 \pm 25.0$ GeV.

Process	cross sec. [fb]	# of events	# of events after all cuts
$W_{\rm H}^+W_{\rm H}^- \to A_{\rm H}A_{\rm H}qqqq$	106.5	53,258	37,560
$W^+W^- \to qqqq$	1773.5	886,770	306
$e^+e^-W^+W^- \to e^+e^-qqqq$	464.9	232,442	23
$e\nu_e WZ \to e\nu_e qqqq$	25.5	12,770	3,696
$Z_{\rm H}Z_{\rm H} \to A_{\rm H}A_{\rm H}hh$	99.5	49,757	3,351
$\nu\bar{\nu}W^+W^- \to \nu\bar{\nu}qqqq$	6.5	3,227	1,486

Table 3: Signal and background processes considered in the $W_{\rm H}^+W_{\rm H}^-$ analysis.

4.b $e^+e^- \to W_{\rm H}^+W_{\rm H}^-$ at 1 TeV

$W_{\rm H}^+W_{\rm H}^-$ production has large cross section (277 fb) at ILC with $\sqrt{s} = 1$ TeV. Since $W_{\rm H}^\pm$ decays into $A_{\rm H}$ and $W^\pm$ with the 100% branching ratio, analysis procedure depends on the W decay modes. In this analysis, we have used 4-jet final states from hadronic decays of two W bosons, $W_{\rm H}^+W_{\rm H}^- \to A_{\rm H}A_{\rm H}qqqq$. Signal and background processes considered in the analysis are summarized in Table 3.

All events have been reconstructed as 4-jet events by adjusting the cut on y-values. In order to identify the two W bosons from $W_{\rm H}^\pm$ decays, two jet-pairs have been selected so as to minimize a χ^2 function,

$$\chi^2 = ({}^{\rm rec}{\rm M}_{W1} - {}^{\rm tr}{\rm M}_W)^2/\sigma^2_{{\rm M}_W} + ({}^{\rm rec}{\rm M}_{W2} - {}^{\rm tr}{\rm M}_W)^2/\sigma^2_{{\rm M}_W}, \tag{4.74}$$

where ${}^{\rm rec}{\rm M}_{W1(2)}$ is the invariant mass of the first (second) 2-jet system paired as a W candidate, ${}^{\rm tr}{\rm M}_W$ is the true W mass (80.4 GeV), and $\sigma_{{\rm M}_W}$ is the resolution for the W mass (4 GeV). We required $\chi^2 < 26$ to obtain well-reconstructed events. Since $A_{\rm H}$ bosons escape from detection resulting in a missing momentum, the missing transverse momentum (${}^{\rm miss}p_{\rm T}$) of the signal peaks at around 175 GeV. We have thus selected events with ${}^{\rm miss}p_{\rm T}$ above 84 GeV. Then, the reconstructed W energy is required to be between 0 GeV to 500 GeV. The numbers of events after the selection cuts are shown in Table 3. The number of remaining background events is much smaller than that of the signal.

As in the case of the $A_{\rm H}Z_{\rm H}$ production, the masses of $A_{\rm H}$ and $W_{\rm H}$ bosons can be determined from the edges of the W energy distribution. Figure 4(a) shows the energy distribution of the reconstructed W bosons. After subtracting the backgrounds from Fig.4(a), the distribution has been fitted with a line shape function. The fitted masses of $A_{\rm H}$ and $W_{\rm H}$ bosons are 82.29 ± 1.10 GeV and 367.8 ± 0.8 GeV, respectively, which are to be compared to their input values: 81.85 GeV and 368.2 GeV. Figure 4(b) shows the probability contours for the masses of $A_{\rm H}$ and $W_{\rm H}$ at 1 TeV. The mass resolution improves dramatically at $\sqrt{s} = 1$ TeV, compared to that at $\sqrt{s} = 500$ GeV. Then, $f = 579.7 \pm 1.1$ GeV was obtained by fitting the energy distribution of the reconstructed W bosons.

5 Summary

The Littlest Higgs Model with T-parity is one of the attractive candidates of physics beyond the Standard Model since it solves both the little hierarchy and dark matter problems simultaneously. One of the important predictions of the model is the existence of new heavy gauge bosons, where they acquire mass terms through the breaking of global symmetry necessarily

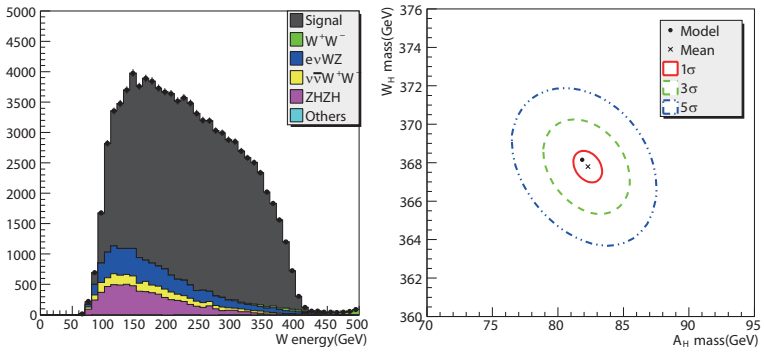

Figure 4: (a) The energy distribution of the reconstructed W bosons with remaining backgrounds after the selection cuts. (b) Probability contours corresponding to 1-, 3-, and 5-σ deviations in the $A_{\rm H}$ and $W_{\rm H}$ mass-plane.

imposed on the model. The determination of the masses are, hence, quite important to test the model.

We have performed Monte Carlo simulations in order to estimate measurement accuracy of the masses of the heavy gauge bosons at ILC. At ILC with $\sqrt{s} = 500$ GeV, it is possible to produce $A_{\rm H}$ and $Z_{\rm H}$ bosons. Here, we can observe the excess by $A_{\rm H}Z_{\rm H}$ events in the Higgs energy distribution with the statistical significance of 3.7-sigma. Furthermore, the masses of these bosons can be determined with accuracies of 16.2% for $A_{\rm H}$ and 4.3% for $Z_{\rm H}$. Once ILC energy reaches $\sqrt{s} = 1$ TeV, the process $e^+e^- \to W_{\rm H}^+W_{\rm H}^-$ opens. Since the cross section of the process is large, the masses of $W_{\rm H}$ and $A_{\rm H}$ can be determined as accurately as 1.3% and 0.2%, respectively. Then, the vacuum expectation value, f, can be determined with accuracy of 4.3% at $\sqrt{s} = 500$ GeV and 0.2% at 1 TeV.

6 Acknowledgments

The authors would like to thank all the members of the ILC physics subgroup [16] for useful discussions. This study is supported in part by the Creative Scientific Research Grant No. 18GS0202 of the Japan Society for Promotion of Science, and Dean's Grant for Exploratory Research in Graduate School of Science of Tohoku University.

References

[1] N. Arkani-Hamed, A. G. Cohen and H. Georgi, Phys. Lett. B **513** (2001) 232;

[2] N. Arkani-Hamed, A. G. Cohen, E. Katz and A. E. Nelson, JHEP **0207** (2002) 034.

[3] H. C. Cheng and I. Low, JHEP **0309** (2003) 051.

[4] H. C. Cheng and I. Low, JHEP **0408** (2004) 061.

[5] I. Low, JHEP **0410** (2004) 067.

[6] E. Asakawa, Phys. Rev. D79, 075013, (2009).

[7] E. Komatsu *et al.* [WMAP Collaboration], arXiv:0803.0547 [astro-ph].

[8] J. Hubisz and P. Meade, Phys. Rev. D **71** (2005) 035016, (For the correct paramter region consistent with the WMAP observation, see the figure in the revised vergion, hep-ph/0411264v3).

[9] M. Asano, S. Matsumoto, N. Okada and Y. Okada, Phys. Rev. D **75** (2007) 063506;
[10] http://madgraph.hep.uiuc.edu/.
[11] http://acfahep.kek.jp/subg/sim/softs.html.
[12] H. Murayama, I. Watanabe, K. Hagiwara, KEK-91-11, (1992) 184.
[13] T. Sjöstrand, *Comp, Phys. Comm.* **82** (1994) 74.
[14] http://wasm.home.cern.ch/wasm/goodies.html.
[15] GLD Detector Outline Document, arXiv:physics/0607154.
[16] http://www-jlc.kek.jp/subg/physics/ilcphys/.